Correction of Residual Artifacts in Prospectively Motion-corrected MR-data

Dissertation

zur Erlangung des akademischen Grades

Doctor rerum naturalium

(Dr. rer. nat)

genehmigt durch die Fakultät für Naturwissenschaften

der Otto-von-Guericke-Universität Magdeburg

von	Master of Science, Uten Yarach
geb. am	12. April 1979 in Nan (Thailand)

Gutachter:	Prof. Dr. rer. nat. Oliver Speck
	Prof. Dr. Nikolaus Weiskopt

eingereicht am:	01 Juni 2016
verteidigt am:	16 Dezember 2016

To my parents and my wife (Chanakarn)

ABSTRACT

Head motion during magnetic resonance imaging (MRI) acquisition can degrade image quality below levels acceptable for clinical diagnosis. Over the years, numerous motion correction techniques have been presented and can be categorized into methods for retrospective and prospective correction. Prospective motion correction (PMC) approaches have been receiving increased attention due to the fact that they can prevent k-space inconsistencies and spin history effects. Furthermore, no extra imaging time is required when an external tracking system is used. However, even with highly accurate and precise tracking and low-latency PMC, large-scale motion can lead to residual artifacts that cannot be compensated for with rigid body adjustment alone. The relative motion of the coil sensitivities, the distortion associated with gradient nonlinearity (*GNL*) and magnetic field inhomogeneities (ΔB_0) due to tissue-specific susceptibilities are widely discussed in the literature.

The main objective of this study was to develop retrospective corrections to minimize the aforementioned residual artifacts in the intra-scan motion MRI after applying PMC. The corrections were integrated into the augmented sensitivity encoding (augmented SENSE) reconstruction, which was recently introduced for retrospectively correcting the rigid body motion and simultaneously alleviating the relative motion of coil sensitivity in multiple-coil MRI data. The distortions caused by *GNL* and ΔB_0 were considered in image domain using the pixel shift method. The type-1 of NUFFT that can map data from uniform k-space to non-uniform image space, and is capable of preserving high spatial frequency components was exploited. Our experiments suggest that including the corrections of the relative motion of coil sensitivity, as well as the geometric distortions due to magnetic field variations (*GNL* and ΔB_0), can further improve the quality of large-scale motion MR images acquired using the prospective motion correction.

ZUSAMMENFASSUNG

Kopfbewegungen während der Bildakquise durch Magnetresonanzbildgebung (MRI) kann die Bildqualität unter das für die klinische Akzeptanz notwendige Niveau verringern. In den letzten Jahren wurde eine Viezahl an Methoden zur Bewegungskorrektur präsentiert, welche in retro- und prospektive Korrektur kategorisiert werden können. Ansätze der prospektiven Bewegungskorrektur (*prospective motion correction*, PMC) erlangten verstärkt Aufmerksamkeit, da sie k-Raum-Inkonsistenzen und Spin-Verlaufs-Effekte verhindern können. Weiter ist von Vorteil, dass keine zusätzliche Zeit zur Bildgebung benötigt wird, wenn ein externes Tracking-System benutzt wird. Jedoch können, trotz hochgenauem und präzisem Tracking und PMC geringer Latenz, starke Bewegungen zu übrigbleibenden Artefakten führen, die nicht allein durch Transformationen starrer Körper kompensiert werden können. Relativbewegungen der Spulensensitivitäten, Verzerrungen aufgrund von Gradienten-Nichtlinearität (*GNL*) und Magnetfeldinhomogenitäten (ΔB_0) aufgrund gewebespezifischer Suszeptibilitäten wurden gemeinhin als relevante Quellen dieser Artefakte diskutiert.

Das Hauptziel dieser Studie ist die Entwicklung retrospektiver Korrekturen, um die oben genannten residuellen Artefakte durch Bewegungen unter Anwendung von PMC zu minimieren. Die Korrekturen wurden in die *augmented sensitivity encoding*-Rekonstruktion (*augmented SENSE*) integriert, welche zuletzt zur retrospektiven Korrektur der Bewegung starrer Körper unter gleichzeitiger Berücksichtigung der Verschiebung der Spulensensitivitäten vorgestellt wurde. Die Verzerrungen durch GNL und ΔB_0 wurden im Bildraum durch pixelweise Verschiebung berücksichtigt. Die nicht-uniforme schnelle Fouriertransformation vom Typ 1 (*type-1 NUFFT*), die Komponenten hoher Raumfrequenzen erhalten kann, wurde hierfür ausgenutzt. Die Experimente legen nahe, dass die Korrektur sowohl der Relativbewegung der Spulensensitivitäten als auch der Verzerrungen durch Magnetfeldveränderungen (*GNL* und ΔB_0) die Bildqualität von PMC-gestützter Bildgebung unter starker Bewegung weiter verbessert.

ACKNOWLEDGEMENT

I knew from the beginning that pursuing doctoral study is a difficult and challenging task. Throughout this long journey, I have gained a lot by learning persevere despite hardship. I am grateful for all of the support and contribution along this journey. I would never have successfully completed this thesis without the assistance of numerous people who I am indebted to.

First of all, I would like to express my sincerest appreciation to my advisor Professor Dr. Oliver Speck, whose thoughtful consideration and guidance has been invaluable. He has supported me throughout my thesis with his patience and vast knowledge whilst allowing me to work in my own way. Without his guidance, support, encouragement and inspiration during the most critical period of my PhD journey, I would not have been able to accomplish this study. To him, I wish to say "You are wonderful supervisor, professor and researcher".

I would like to thank Office of the Civil Service Commission (OCSC) of Thailand for the financial support throughout my study. Thanks to BMBF (Forschungscampus STIMULATE, grant number: 03FO16101A) and NIH (grant number: DA021146) for research funding.

My sincere thanks also go to Assistant Professor Dr. Chaiya Luengviriya from Kasetsart University, Thailand for his earlier guidance on this thesis. He also supplied me with the necessary Matlab materials as well as references I needed. I would also like to thank Dr. Suwit Saekho from Chiang Mai University, Thailand, who was my first advisor and who introduced me into the field of medical imaging.

Many thanks also to our BMMR team members especially Mo-Co members who have been developing the motion tracking system which is a main tool for this research work. With their supports, my experiments have been simply done. I also greatly appreciate the many useful advices from Dr. Myung-Ho In and Dr. Oleg Poznansky.

I would like to thank my Thai friends in University Magdeburg for all great times that we have shared. Talking, cooking, and eating with them makes my stay more enjoyable.

My endless thanks especially go to my parents, who passed away before I started my doctoral study. Even though, their unconditional love, personal spirit and strong are the best motivation of my work and will be forever the power of my life. Without my parents, nothing has been possible. This last word of acknowledgement I have saved for my dear wife Chanakarn Yarach, who has been standing beside me throughout my doctoral study. Her love and support provided me the energy to attain my study.

TABLE OF CONTENTS

CHAPTER:

LIST OF FIGURES

ABBREVIATION

BW	Bandwidth
CG	Conjugate Gradient
CNR	Contrast to Noise Ratio
DCF	Density Compensation Function
DFT	Discrete Fourier Transform
EPI	Echo-Planar Imaging
FE	Frequency Encoding
FFT	Fast Fourier Transform
FLASH	Fast Low Angle Short
FOV	Field Of View
FSE	Fast Spin Echo
GRAPPA	Generalized Auto-calibrating Partially Parallel Acquisitions
Hz	Hertz
IRB	Institutional Review Board
MPRAGE	Magnetization-Prepared Rapid Gradient-echo
MRI	Magnetic Resonance Imaging
NMR	Nuclear Magnetic Resonance
NUFFT	Non Uniform Fast Fourier Transform

PE	Phase Encoding
PMC	Prospective Motion Correction
RMSE	Root Mean Square Error
RSS	Root Sum of Squares
SENSE	Sensitivity encoding
TPS	Thin Plate Spline
TR/TE/TI	Repetition Time/Echo Time/Inversion Time

CHAPTER 1

1. INTRODUCTION

1.1. Motivation

Magnetic Resonance Imaging (MRI) is a non-invasive imaging modality. Unlike Computed Tomography (CT), MRI does not use ionizing radiation. In addition, MRI provides a large number of flexible contrast parameters. These provide excellent soft tissue contrast. MRI can also be sensitized to many specific parameters. These include imaging brain oxygen saturation changes due to neuronal activity; measuring blood flow velocities; measuring temperature; and measuring the concentration of metabolites. MRI is also the only way to directly image diffusion of water molecules in vivo. However, patient motion during MRI acquisition remains a severe problem and may degrade image quality below levels acceptable for clinical diagnosis**.** Numerous motion correction techniques have been presented over the past few decades. They can be categorized into methods for retrospective and prospective corrections based on motion information that originates from MR-data, i.e. navigator echoes (Ehman et al., 1989) and self-navigated (Pipe, 1999), or from external motion detection devices (Derbyshire et al., 1998). When motion occurred only infrequently during an examination, the image quality can be improved after either the corrupted signals were rejected or replaced by resampled signals (Bydder et al., 2002b; Pipe, 1999). Retrospective correction (Atkinson et al., 1999; Batchelor et al., 2005) was applied in the image reconstruction process by reversing the motion effects on the corrupted signals. As a way of preventing inconsistent k-space data, real-time prospective motion correction (PMC) (Thesen et al., 2000; Ward et al., 2000; Zaitsev et al., 2006) has been proposed with continuous or repeated position determination, followed by gradient and RF adjustment immediately before each excitation to result in data as if no movement had occurred. Furthermore, no extra imaging time is required when an external tracking system, which commonly computes pose in six degrees of freedom, is used (Zaitsev et al., 2006).

Even with highly accurate and precise tracking and low-latency PMC, large-scale motion may lead to residual artifacts (Maclaren et al., 2013) that cannot be compensated for with rigid body adjustment alone. Apart from the inherent tracking problem (Maclaren et al., 2011), the commonly discussed artifact sources are the relative motion of the coil sensitivity (Aksoy Bammer, 2008; Atkinson et al., 2004; Bammer et al., 2007; Benerjee et al., 2013; Luengviriya, 2010) as well as the geometric distortions caused by *GNL* (Hu et al., 2005; Polzin et al., 2004) and the subject-related field inhomogeneity (ΔB_0) (Ooi et al., 2013).

The coil sensitivity misalignment due to physiological movement within the static RF receive coils will cause variation of signal intensity and phase and lead to images with shading artifacts after combination of single coil images (Atkinson et al., 2004; Banerjee et al., 2013). This artifact appears more visible in parallel imaging with high acceleration factors (Aksoy et al., 2008), and also becomes more challenging with a large number of small array coils (Luengviriya, 2010). A previous study (Bammer et al., 2007) introduced an effective technique for reconstructing the motion dataset, and also considering the relative motion of coil sensitivity artifact, and is termed 'augmented sensitivity encoding (augmented SENSE) reconstruction' – namely, the k-space data were divided into several pipelines based on the motion poses, and compensated for coil sensitivity mismatch individually in an iterative fashion. The sensitivity maps accounted in (Bammer et al., 2007) were measured for all motion poses. However, Benerjee et al., (2013) reported that the coil sensitivities relative to the motion poses can be prepared by adjusting the initial calibration data. This strategy worked well at the low field strength (i.e., 1.5T) which coil loading effect caused by the body being imaged is small, in comparison to higher field strengths. *Therefore, this thesis observes the impact of the relative motion of coil sensitivity artifacts and determines the necessity of its correction at 7T MRI.*

Motion within a non-linear gradient manifests as spatial distortion and blurring since object geometry at multiple object poses within the non-linear gradient fields, and thus the k-space data become inconsistent between phase encoding steps as demonstrated by Polzin et al. (2004) and other authors (Hu et al., 2005). This effect is more pronounced in

peripheral regions where gradient deviations are strongest. In general, not only *GNL* can result in spatial distortion due to motion, but B_0 inhomogeneity caused by magnetic properties of the subject (e.g., air-tissue interfaces) is a relevant source of geometric distortions (Jezzard et al., 1995; Jezzard et al., 1999; Ooi et al., 2013). Particularly, its effect is increased at a high field strength such as 7T (Speck et al., 2008). Recently, the locations and sizes of B_0 field shifts within the brain at 7T for different head movements were reported (Sulikoswa et al., 2014). These observations showed that the local field changes strongly depend on the subject orientation. Consequently, PMC at high field may be impacted by this variation even in conventional Cartesian MRI acquisitions with low readout-bandwidth (BW) that are often chosen to optimize signal-to-noise (SNR) or contrast-to-noise (CNR) ratios in structural imaging. In static and conventional MRI, the distortion correction is widely considered in post-processing steps (Baldwin et al., 2007; Jezzard et al., 1995) rather by taking part in during image reconstruction. This traditional pipeline becomes impractical for intra-scan motion MRI, since the set of k-space is interfered by the different magnetic field displacements, resulting not only distortion but also blurring in image space. *Therefore, this thesis is to develop the retrospective corrections to minimize the geometric distortions within intra-scan motion MRI after applying PMC at 7T MRI.*

1.2. Thesis Outline

Chapter 2 is a brief introduction to MRI. It covers some basic MR physics; signal generation; signal reception; spatial encoding; and image generation. The rigid body motion artifact, its existing correction methods, and the residual artifacts after the motion correction are presented. The advance image reconstruction algorithms such as the gridding, the NUFFT, and the augmented SENSE are described.

Chapter 3 demonstrates the influence of coil sensitivities within intra-scan motion data with PMC enabled, and the necessity of its correction. The mathematical model, the coil sensitivity estimations, and the reconstruction algorithm are described. Both fully-sampled and under-sampled of intra-scan motion MR data are observed.

Chapter 4 proposes the MR signal model corrupted by the gradient nonlinearity. The gradient displacement field which is key information for this model is obviously explained. The iterative correction scheme using type-1 of NUFFT is highlighted. The use of proposed reconstruction to improve the quality of images is demonstrated.

Chapter 5 proposes the correction of subject-specific susceptibility induced geometric distortion in PMC data. The distorted space obtained from the B_0 field map is derived. B_0 field variations at different head orientations are investigated. The method of implementation in phantom and in vivo brain are presented.

Chapter 6 includes a detailed discussion of the proposed correction techniques.

Finally, Chapter 7 includes the unresolved challenges that require further investigations, and the conclusion.

CHAPTER 2

2. BACKGROUND

MRI has been widely used as a non-invasive clinical and research modality for the study of human anatomy. It exploits the phenomenon of nuclear magnetic resonance (NMR) in an external magnetic field, whereby nuclei absorb and re-emit certain radio frequency (RF) waves during changes in the nuclear spin state. Image formation using NMR signals was developed by Lauterbur and Mansfield (Lauterbur, 1989; Mansfield et al., 1977) based on spatial encoding principles, which won them the 2003 Nobel Prize in Physiology and Medicine. Since then, MRI has undergone dramatic improvements in all the features that define image quality, such as resolution, SNR, contrast enhancement and speed. Specific structures, such as arteries, lesions, white matter fiber tracts, can also be visualized by manipulating RF fields and local magnetic field.

2.1. Principle of MRI

2.1.1. Basic NMR physics

MRI is based on the interaction of a nuclear spin with external magnetic fields. All atomic nuclei consist of nucleons (protons and neutrons) that possess a quantum mechanical property called *spin*. If the nucleus consists of an odd number of nucleons, the nuclear spin is greater than zero, the nucleus is NMR-active, and a *magnetic dipole moment*, or simply a magnetic moment, can be associated with the nucleus. The dominant nucleus in biological tissues is the proton in hydrogen. The interaction of the NMR-active nuclei, e.g., the proton, with the external magnetic field results in the precession of the spin about the external field direction, which is called the *Larmor precession*.

The Larmor precession occurs at a specific frequency, called the *Larmor frequency*, which depends on the strength of the external magnetic field and the characteristics of the nucleus:

$$\omega_0 = \gamma B_0 \qquad (2.1)$$

where ω_0 is the Larmor frequency, B_0 is the external magnetic field, and γ is a constant called the *gyro-magnetic ratio*, which depends on the nucleus involved.

In a classical model, the precession of the spins around the magnetic field occurs out of phase with each other in the presence of a static external magnetic field. This out-of-phase precession results in a net macroscopic magnetization in the direction of the external magnetic field, i.e., the longitudinal direction, since the transverse magnetization components cancel out due to the out-of-phase precession[1]. This is usually referred to as the *equilibrium magnetization*, denoted by M_0. Note that, by definition, magnetization is a vector field equal to the volume density of permanent or induced magnetic dipole moments in a magnetic material.

To detect this magnetization, it can be rotated away from its alignment along the B_0 axis by applying a radio frequency (RF) magnetic field for a short time, i.e., an RF pulse, with

---

[1] The B_0 direction is referred to as the longitudinal direction and is often assumed to be in the direction of the z-axis. Perpendicular to B_0 the direction is the transverse plane, i.e., the xy-plane.

its frequency tuned to the Larmor frequency (see Figure 2.1). The RF pulse is produced by an RF transmit coil, which is often used as the receiving coil as well. The RF magnetic field is also referred to as the B_1 field. The duration and power of the RF pulse determines the *flip angle* (α) by which the magnetization is rotated.

$$\alpha = \gamma \int_0^{\tau} |B_1(t)|\, dt \qquad (2.2)$$

The application of the RF pulse tilts the net macroscopic magnetization away from the B_0 direction, resulting in a net (macroscopic) transverse magnetization component precessing at the Larmor frequency. The produced magnetic field precesses along with the magnetization, yielding a changing flux in the receive coil and therefore a current based on Faraday's law.

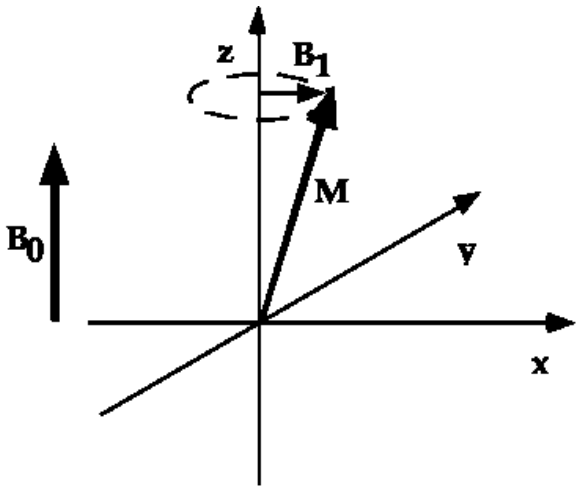

Figure 2.1. The magnetization vector is tilted away from the longitudinal equilibrium in the B_0 direction towards the transverse plane by the application of an RF pulse, B_1, at the Larmor (resonance) frequency.

2.1.2. Spatial Localization for Imaging

The precession frequency given in Eq. 2.1 can be modified by applying additional magnetic field gradients, thereby forcing the Larmor frequency to be spatially dependent.

An additionally applied magnetic field gradient $\vec{G} = \nabla B \approx \nabla B_z$[2] yields the following spatially dependent precession frequency ω:

$$\omega(\vec{r}, t) = \gamma(B_0 + \vec{G}(t) \cdot \vec{r}) \qquad (2.3)$$

Thus, by exploiting magnetic field gradients in all three spatial dimensions, one is able to fully spatially encode the object under investigation. MRI is described in more detail below.

2.1.2.1. Selective Excitation

At the beginning of every conventional 2D MRI experiment the slice to be imaged must be selected, normally in the *z*-direction. To this end, a selective RF excitation pulse is required, which excites only spins in a well-defined frequency range. Such RF pulses have a well-defined shape such as Gaussian or Sinc with a finite frequency bandwidth $\Delta\omega_{rf}$ around the center frequency ω_{rf}. For small flip angles, the actual excitation profile of such pulses can roughly be approximated by a simple Fourier transformation of the temporal modulation function of the RF pulse (small tip angle approximation (Pauly et al., 2011)). In this case, a sinc-type excitation pulse corresponds to a box-car-shaped excitation profile, a Gaussian RF pulse to a Gaussian excitation profile. By applying a frequency-selective RF pulse with frequency bandwidth $\Delta\omega_{rf}$ in combination with a constant magnetic field gradient $B_z = \partial B_z / \partial z$ only spins within a distinct slice with thickness Δz are excited.

$$\Delta z = \frac{\Delta\omega_{rf}}{\gamma \cdot G_z} \qquad (2.4)$$

[2] B_x and B_y can be neglected because $\left|\vec{B}_0\right| \gg \left|\vec{B}(\vec{r})\right|$

The slice position z_0 is adjusted by the carrier frequency ω_{rf} of the pulse, which can be chosen slightly off-resonant from the Larmor frequency given in Eq. 2.1. Exploiting again Eq. 2.3, the frequency offset corresponds to an offset in the slice position.

$$z_0 = \frac{\omega_{rf} - \omega_0}{\gamma \cdot G_z} \qquad (2.5)$$

To compensate for spin dephasing caused by the slice gradient, an inverted gradient must be applied after slice-selection.

2.1.2.2. K-Space Formalism

According to Eq. 2.3 magnetic field gradients $\vec{G}(t)$ result in a spatially dependent Larmor frequency. In the presence of such a gradient, the signal $m(t)$ picked up by the receiver is composed of the sum of all spins in the object under investigation with spin density $\rho(\vec{r})$ (neglecting relaxation effect and magnetic field inhomogeneities) at position $\vec{r}$:

$$m(t) \propto \int \rho(\vec{r}) \cdot e^{-i\int_0^t \omega(\vec{r},t')dt'} d^3\vec{r}$$

$$\propto e^{i\omega_0 t} \int \rho(\vec{r}) \cdot e^{-i\gamma\int_0^t \vec{G}(t')dt'\vec{r}} d^3\vec{r} \qquad (2.6)$$

By substituting $\vec{k} = \gamma \int_0^t \vec{G}(t')dt'$, where t denotes the time the magnetic field gradient is applied, and omitting the exponential term with spatially independent modulation frequency ω_0, the relation in Eq. 2.6 yields:

$$m(\vec{k}) \propto \int \rho(\vec{r}) \cdot e^{-i\vec{k}\vec{r}} d^3\vec{r} \qquad (2.7)$$

In this form, the received signal m can be recognized as the Fourier transformation of the spin density $\rho(\vec{r})$ at position $\vec{r}$. Therefore, the spin density (or the image) can be determined by simply applying the inverse Fourier transformation to the received signal.

$$\rho(\vec{r}) \propto \int m(\vec{k}) \cdot e^{i\vec{k}\vec{r}} d^3\vec{k} \qquad (2.8)$$

By introducing the reciprocal space vector $\vec{k}$, the so-called k-space can be defined, which is spanned by three orthogonal k-vectors allowing a simple description of the spatial encoding used in MRI (Twieg, 1983). This concept, and how it is carried out in practice is described in the following sections and discussed in more detail, for example, in (Haacke, 1999).

2.1.2.3. Frequency Encoding

After slice selection, one spatial dimension is encoded by a spatial frequency modulation, which the so-called frequency encoding. Here, frequency encoding is carried out in the x-direction by applying a constant magnetic field gradient $G_x = \frac{\partial B_z}{\partial x}$, during data acquisition. The longer and stronger the gradient G_x is applied, the higher is the spatial frequency content in the received one-dimensional signal:

$$m(k_x) = \int \rho(\vec{x}) \cdot e^{-ik_x x} dx \quad \text{with} \quad k_x = \gamma G_x \cdot t_x \qquad (2.9)$$

In practice, the signal is sampled at N_x discrete points in intervals of Δt_x while a constant gradient G_x is on. Thus, the discrete steps traversed in the k_x direction in k-space are $\Delta k_x = \gamma G_x \cdot \Delta t_x$. In most cases, frequency encoding is performed by starting at a maximum negative spatial frequency $-k_x^{max}$ and ending at a maximum positive spatial frequency $+k_x^{max}$. To obtain the echo maximum at k_x = 0, before the actual frequency encoding is carried out, the spins are dephased by applying a negative gradient in the x-direction (see Figure 2.2).

2.1.2.4. Phase Encoding

The phase of the NMR signal can be used to encode a second spatial dimension, here the y-direction, within the excited slice. The so-called phase encoding is carried out between the slice excitation and the signal acquisition. To this end, a magnetic field

gradient, the phase encoding gradient $G_y = \frac{\partial B_z}{\partial y}$, is applied in the y-direction (perpendicular to the x-direction) for a duration t_y, thereby generating sinusoidal modulations of the spin phases in the sample. Thereafter, all spins precess with the same frequency, but now with a spatially dependent phase:

$$\Phi(y) = \gamma G_y t_y y \qquad (2.10)$$

This modulation persists throughout the following read-out procedure. In contrast to frequency encoding, the phase encoding process has to be repeated several times by changing either the gradient strength G_y or the phase encoding time t_y in order to cover the entire two dimensional k-space. With $k_y = \gamma G_y t_y$, the two-dimensional signal originating from the excited slice can be written as

$$m(k_x, k_y) = \iint \rho(x, y) \cdot e^{-i(k_x x + k_y y)} dx dy \qquad (2.11)$$

In Figure 2.2 (left), the sequence of RF and gradient pulses are shown for a simple gradient echo experiment using a conventional spin-warp trajectory for phase encoding (Edelstein et al., 1980). After slice selection (1) the starting point for the read-out procedure is set by applying a negative gradient in the x-direction and (normally at the same time) a phase encoding gradient in the y-direction (2), followed by the actual read-out procedure (3). This corresponds to moving at a certain k_y position in k-space in the k_x-direction from left ($-k_x^{max}$) to right ($+k_x^{max}$).

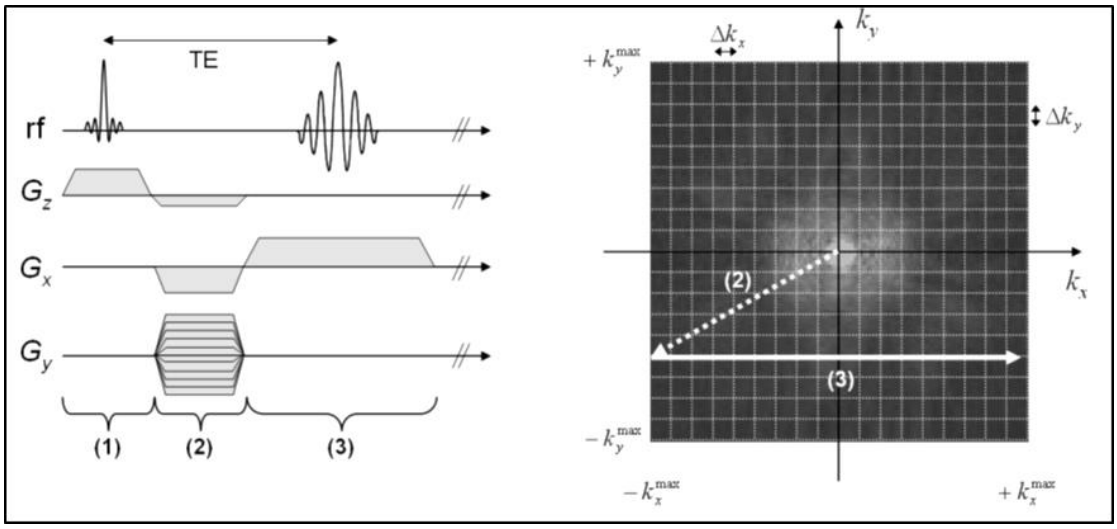

Figure 2.2. Schematic description of spatial encoding in MRI. On the left, a typical spin-warp gradient echo pulse sequence is displayed, and on the right, the corresponding k-space trajectory. In step (1), the slice selection is carried out by an RF excitation applied during a normally constant gradient in z-direction. In step (2), the rephase lobe of the slice select gradient is applied. Normally at the same time, a negative gradient lobe in x is switched, moving the trajectory in k-space to $-k_x^{max}$. Simultaneously, a phase encoding gradient applied in the y-direction moves the trajectory to a specific k_y-value. The actual read-out procedure (3) follows, which corresponds to travelling in the k_y-direction in k-space from left to right. (from Breuer, 2006).

This procedure must be repeated with multiple phase encoding gradients running from $-G_y^{max}$ to $+G_y^{max}$ in N_y equidistant steps to cover the entire k space in the k_y-direction.

$$\Delta k_x = \gamma \frac{G_x t_x}{N_x} = \gamma G_x \Delta t_x \qquad \Delta k_y = \gamma \frac{2G_y^{max} t_y}{N_y} = \gamma \Delta G_y t_y \tag{2.12}$$

The concept of phase encoding can be extended to the remaining third dimension instead of using slice selection. By applying an additional phase encoding gradient G_z in the z-direction, the signal originating from the excited slab can be spatially encoded in the slice direction. A relatively thick slab is excited and encoded in multiple thin partitions.

$$m(k_x, k_y, k_z) = \iiint \rho(x, y, z) \cdot e^{-i(k_x x + k_y y + k_z z)} dx dy dz \qquad (2.13)$$

Using the Fourier transform definition, it is clear from the form of Eq. 2.13 that the total signal $m(k_x, k_y, k_z)$ is the Fourier transform pair, $\rho(x, y, z)$, defined in k-space. The gradients can be varied to change the frequency and phases of the isochromat to fill k-space. Once this has been done, the data can be inverse Fourier transformed to display the image.

However, this is an idealized model of the processes involved in an MRI scan. In order that the spins are displayed accurately in the image, they must feel the magnetic field strength that the system expects them to. If they experience a field that is stronger or weaker than that intended for their position, then their Larmor frequency will be altered accordingly. This means that when decoded, the spin will be displayed in the wrong position, distorting the image.

2.2. The Geometric distortion in MRI

NMR modality, just like other modalities, does have some limitations: the limitations are related to the homogeneity of the field generating devices used to form the image. In other words, geometric distortion can arise from magnetic field inhomogeneity and the non-linearity of the gradient field. It can be a serious problem in some MRI applications where high geometric accuracy is required. In some cases, non-uniformity of the magnetic field can be large enough, for example in the presence of metal objects, to cause significant degradation of the image. Magnetic field inhomogeneities refer here to the cause of dephasing of nuclear spins during data acquisition, which in turn leads to a loss of NMR signal. The final resulting effect is a noticeable reduction in image intensity.

The distortion caused by gradient field non-linearity is very small near to the magnet center or iso-center, but increases when moving away from the center. It is strongest at the field of view boundary. It can be as large as 6-8 cm (Baldwin et al., 2007; Doran et al., 2005; Wang et al., 2004b), so the correction of geometric distortion here is necessary.

The current generations of MRI scanners have been designed with short gradient rise times of less than 200 ms, to achieve shorter rise times. The gradient design is restricted to be shorter and with fewer turns. Such restrictions have led to an increase in the gradient field nonlinearity which results in image distortions. The effects of the gradient field nonlinearity which is a consequence of imperfections and limitation of the gradient coil design, depends on the geometry of the gradient coils and its effects, which are constant in time and independent of the imaging sequence which is used.

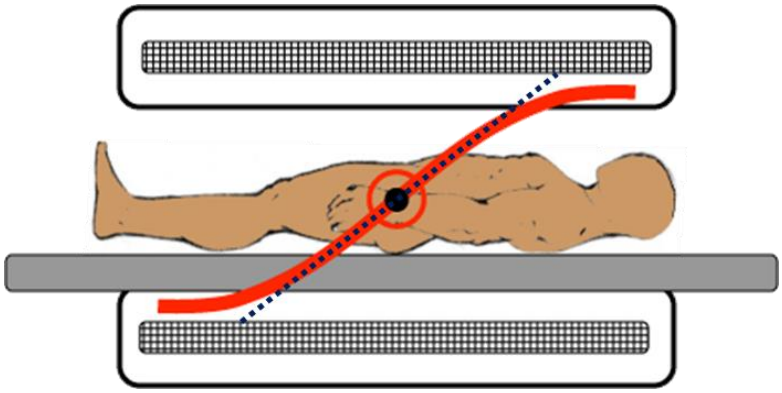

Figure 2.3. Schematic shows the geometric distortion of a typical gradient profile along the z-axis, with decreasing linearity (red line) as the distance from the magnet iso-center increases. The black dotted line shows the desired linear gradient profile (from Zhuo et al., 2006).

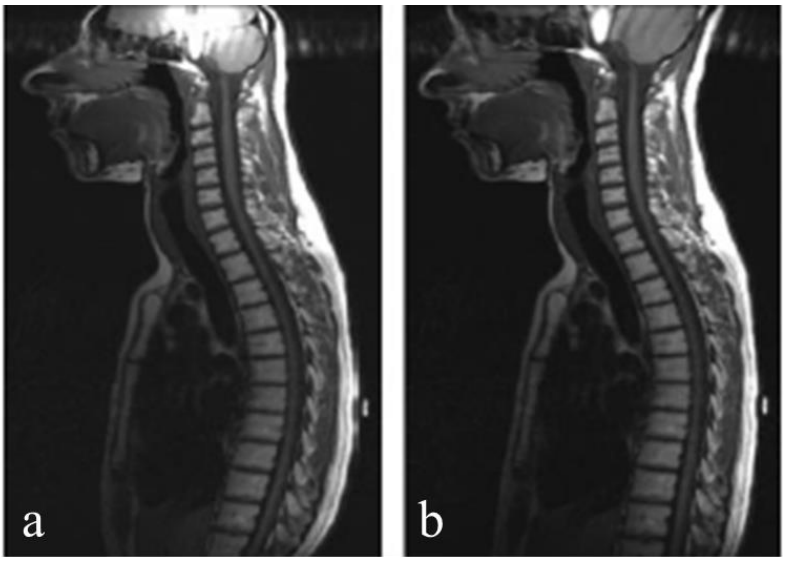

Figure 2.4. Gradient field non-linearity artifact. a) MR image obtained with SE sequence and large field of view, b) Image obtained with a vendor-supplied correction algorithm shows correction of the geometric distortion (from Mahesh, 2004).

The most complex form of geometric distortion with MR scanning is object-specific. This distortion is complex, because it depends on both the present material and the shape of the structure being imaged. The phantom-based quantifications are very useful to assess the general scan quality but they cannot take into account the object dependent parameters, such as magnetic susceptibility differences, chemical shift and flow. Sumanaweera (1994) presented a study of air-tissue and bone-tissue susceptibility effects at 1.5T MRI, and concluded that the distortion at bone-tissue interfaces is negligible compared to the typical 1 mm MR image resolution, but the distortion at air-tissue interfaces has the size up to 2 mm. It is possible to correct those spatial mis-registrations due to susceptibility differences and chemical shift by manipulation of the parameter settings of the used sequence during acquisition, but nevertheless one must still be careful, because the air-tissue effect can be significant. Lüdeke et al have shown the local field deviation can be up to 10 ppm (Ludeke et al., 1985; Michiels et al., 1994). Furthermore, the geometric distortions can differ depending on the sequence. For example, geometric distortions due to the inhomogeneity in the main magnetic field and

the susceptibility difference are less in spin echo sequences than gradient echo sequences. Therefore, the selections of sequence parameters along with optimized scanner calibration are therefore important optimization aspects.

2.3. The Standard Distortion Correction Model

For simplification, relaxation during the acquisition is ignored in the following. The one-dimensional MRI signal (m) in uniform Cartesian imaging can be generated by freely precessing magnetization (ρ) in the presence of a linear magnetic field (B) as

$$m(t) = \int_{FOV_x} \rho(x) \cdot e^{-i\gamma \int_0^t B(x,\tau)d\tau} dx \qquad (2.14)$$

Ideally, the magnetic fields only include the static homogenous B_0 and constant gradient G_x.

$$\int_0^t B(x,\tau)d\tau = (B_0 + G_x x)t \qquad (2.15)$$

In reality, the static and gradient fields are not perfectly linear. The non-linear terms $\Delta B_0(x)$, $\Delta G_x(x)$ are always superimposed. Thus Eq. 2.15 becomes

$$\int_0^t B(x,\tau)d\tau = (B_0 + \Delta B_0(x) + G_x x + \Delta G_x(x))t \qquad (2.16)$$

After signal demodulation, the signal equation in the presence of field inhomogeneities becomes

$$m(t) = \int_{FOV_x} \rho(x) \cdot e^{-i\gamma(G_x x + \Delta G_x(x) + \Delta B_0(x))t} dx$$

$$= \int_{FOV_x} \rho(x) \cdot e^{-i\gamma G_x t\left(x + \frac{\Delta G_x(x) + \Delta B_0(x)}{G_x}\right)} dx \qquad (2.17)$$

Setting $k(t) = \gamma G_x t/2\pi$, the signal equation transforms to:

$$m\big(k(t)\big) = \int_{FOV_x} \rho(x) \cdot e^{-i2\pi k(t)\left(x + \frac{\Delta G_x(x) + \Delta B_0(x)}{G_x}\right)} dx \qquad (2.18)$$

A coordinate transformation operator is defined as:

$$x_d = T[x] = x + \frac{\Delta G_x(x) + \Delta B_0(x)}{G_x}, x = T^{-1}[x_d] \qquad (2.19)$$

where $T[\cdot]$ is the operator that maps true object locations (scanner's coordinate) to distorted image locations.

$$dx_d = \left(1 + \frac{\Delta G_x'(x) + \Delta B_0'(x)}{G_x}\right) dx \qquad (2.20)$$

Substituting variables x_d and dx_d for x and dx leads to:

$$m\big(k(t)\big) = \int_{FOV_x} \frac{\rho(T^{-1}[x_d])}{1 + (\Delta G_x'(T^{-1}[x_d]) + \Delta B_0'(T^{-1}[x_d]))/G_x} \cdot e^{-i2\pi k(t) x_d} dx_d \qquad (2.21)$$

A standard Fourier transform of $m\big(k(t)\big)$ yields the distorted image (I_d) with both a geometry and intensity distortions.

$$\mathfrak{F}^{-1}\{m\big(k(t)\big)\} = I_d = \frac{\rho(T^{-1}[x_d])}{1 + (\Delta G_x'(T^{-1}[x_d]) + \Delta B_0'(T^{-1}[x_d]))/G_x} \qquad (2.22)$$

To correct this problem, the displacement fields (warping function, $T[\cdot]$) and its derivative (Jacobian of the transformation, $1 + (\Delta G_x'(T^{-1}[x_d]) + \Delta B_0'(T^{-1}[x_d]))/G_x$) are required. During warping the distorted image back to undistorted image, the interpolation (Thevenaz et al., 2000) plays a key role for resampling the new pixel values.

2.4. Motion Artifact in MRI

2.4.1. Origin of Motion Artifact

Despite major advances in MR pulse sequence design and image reconstruction, motion still remains a significant problem, with high clinical and public health costs. Both ghosting and blur are common image artifacts from motion during the acquisition that often mask subtle lesions, obscure morphological details characteristic for pathology, or simply just lower diagnostic confidence. This can become particularly problematic for inexperienced referring physicians who cannot read through artifacts, or surgeons who must interpret scans to plan and perform their procedures. Moreover, gains in resolution are typically accomplished via increased scan time and are often offset by motion artifacts. Similarly, for 2D imaging, when motion occurs between the acquisitions of slices that form a 3D volume, the integrity of this volume is compromised. Due to through-plane motion, spins that have been partially saturated by previous slice excitations can enter the imaging slice and lead to altered SNR or contrast. Overall, motion leads to strong image artifacts that often render studies meaningless, particularly if patients are uncooperative, or have certain (neurological) disorders that cause involuntary movements. Sadly, some patients are simply too ill or suffer from too much pain to remain stationary.

For high-resolution MRI with long scan times, the head motion causes motion artifacts primarily in the phase-encoding direction (intra-scan motion). The frequency encoding direction is less affected since the k-space data corresponding to the readout direction are collected over a relatively short period of a few milliseconds or less, and can be regarded as instantaneous on the time scale of most physiologic motion. However, in the phase encoding direction, the positions are encoded by a step-wise changing magnetic field gradient prior to the acquisition of each line of k-space. Therefore, the time interval between two neighboring points in the phase encoding direction is TR, which ranges from tens of milliseconds or several seconds and cannot be regarded as instantaneous. Such motion will cause additional phase shifts to the spins from line to line, which will

corrupt the spatial encoding and give rise to ghosting. Head motion is usually random motion, which makes the artifacts smeared out along the phase encoding direction and can obscure pathology (see Figure 2.5)

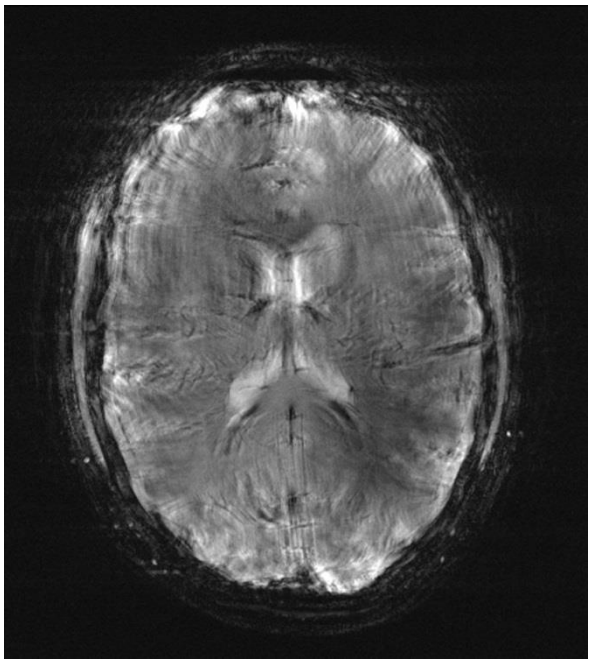

Figure 2.5. GRE T2* weighted image on a volunteer who was asked to slightly moved his head throughout the scan (BMMR Magdeburg).

2.4.2. Effect of Rigid Body Motion on k-Space

Rigid body motion has a well–defined influence on the raw k–space data. The effects described in this section are the basis for all rigid body motion estimation and correction techniques operating in inverse space. An important property of k–space is the fact that the effects of translation and rotation of an object can be separated. Translations only affect the phase and rotations only affect the magnitude of the raw signal. For explanatory purposes, the following descriptions assume a standard 2DFT data acquisition with frequency encode direction the $k_x(x)$ direction and phase encode direction in the $k_y(y)$ direction. Motion can, of course, occur in all three dimensions.

2.4.2.1. Translation in k-Space

The simplest motion by an object is rigid body translation, and many of the motions observed in MR imaging can be considered to be simple translations. According to the Fourier Shift Theorem, which is derived at the section 2.7.1, a translation in the spatial domain is equivalent to a phase change in the spatial frequency domain. Typically in MRI, translational motion occurs slowly as compared to the time of a single excitation and readout of one k-space data line or view. Motion in the short time window between the RF excitation and the data readout is termed intra-view motion and is usually considered to be negligible. More important is the inter-view motion, occurring between successive data readout repetitions. If the translational position of an object varies from TR to TR, phase inconsistencies are present in each phase-encoded line of the sampled k-space and image artifacts will appear in the phase encode direction of the spatial domain image reconstruction. The phase corruption, $\Delta\Phi$, for a certain k-space sample is described by Eq. 2.23 where k_x and k_y are the k-space locations of the sample, and Δx and Δy are the relative displacements of the object from a reference position.

$$\Delta\Phi(k_x, k_y) = 2\pi(k_x \Delta x + k_y \Delta y) \qquad (2.23)$$

If the translation is inter-view, the relative displacement of the object will be constant for an entire line of k-space in the k_x (frequency encode, FE) direction. Therefore, the displacement in the FE direction, Δx, will impose a ramp of additional phase on the acquired samples, and the displacement in the PE direction, Δy, will cause an additional constant phase. Even a single displacement at some point in the data acquisition will cause a phase inconsistency in the k_y (PE) direction of the acquired k-space. Such an inconsistency violates the assumption of the Fourier inversion that the longitudinal magnetization, i.e. the object, was in the same state from TR to TR. Translation in the through-plane (slice select) direction is also detrimental. Small through-plane displacements can cause a modulation of k-space magnitude in the PE direction, which also results in ghosting artifacts. If the acquired MR dataset is 3D with phase encodes in

both the k_z and k_y directions, the z displacement will add a similar phase constant term, and ghosting in the reconstructed image volume will occur in both the z and y directions.

2.4.2.2. Rotation in k-Space

Rotation is a change in orientation, and almost any real anatomical motion has some component of rotation. If an object imaged with MR rotates in an unknown way during data acquisition, the sampled k-space will not be the part of k-space intended for collection. According to the Fourier Rotation Theorem, which is derived at the section 2.7.1, the rotation of an object in the spatial domain is also a rotation in the spatial frequency domain. Therefore, the acquired k-space view of a rotated object will be assigned incorrect (k_x, k_y) coordinates when it is placed in the rectilinear grid of acquired 2DFT data. In the likely scenario that the object rotation is primarily inter-view, the data inconsistencies will primarily be in the PE direction. The strategies for overcoming rotational motion are similar to those to overcome translational motion except for the methods that attempt to correct already acquired k-space data. In the case of translation correction, only a simple phase correction needs to be applied. In the case of rotation, one needs to replace a particular k-space sample with a completely different value, i.e. the value that really belongs to that particular (k_x, k_y) coordinate. If that exact k-space coordinate was not acquired, interpolation will be necessary to estimate its value based on neighboring points (Atkinson et al., 2003). This process is computationally more difficult and becomes increasingly more so with larger or more frequent rotational motions.

2.5. Corrections of Rigid Body Motion Artifact

Optimized pulse sequences (Frahm et al., 1986) and accelerated image acquisition (Lustig et al., 2007) are usually employed to reduce data acquisition periods in time, such that motion becomes negligible. By acquiring k-space data faster than the typical time scale of motion, artifacts can be reduced to a minimum. However, they are still restricted for high SNR and high resolution structural MRI. Therefore, other correction schemes

that can be used with nearly all imaging sequences have been proposed. They are generally referred to as retrospective and prospective motion corrections.

2.5.1. Retrospective Correction

Retrospective motion correction addresses motion artifacts after the acquisition of a complete set of raw image data. Linear motion is accounted for by using a phase ramp in k-space (Korin et al., 1989), image rotation by rotation of profiles in k-space (Atkinson et al., 2003; Maas et al., 1997). Retrospective motion correction is thus a reordering of k-space data from the acquired regular grid to an irregular grid which matches the static image.

Without the prior knowledge of motion information, an autofocus method has been proposed by Atkinson et al. (1999). This can reduce motion artifacts using an optimization procedure that finds the patient motion that minimizes a focus criterion-entropy in the image. A similar technique has also been combined with parallel imaging (Atkinson et al., 2004). A general framework to correct for arbitrary motion can be modeled by setting up a forward equation from the ideal object to corrupted k-space data (Batchelor et al., 2005). Using matrix descriptions, motion is modeled as linear mapping and motion correction is reduced to an inverse problem for a generalized encoding matrix including MR encoding and motion related spatial transformations. The inversion is performed using the LSQR routine in MATLAB. This requires a cost function to assess the image and to allow the algorithm to converge (again, entropy is used).

Aksoy et al. (2006) demonstrates that the motion information between subsequent k-space profiles/interleaves relative to a reference point can be alternatively determined using intrinsic navigator images (e.g. low resolution spiral) by co-registering each navigator image to the reference image, then an augmented parallel imaging reconstruction (Bammer et al., 2007) was performed in order to avoid local under-sampling and variable sampling density as well as to address coil sensitivity alterations induced by motion within the coil sensitivity field. Bammer et al. (2007) also suggested that the effect of altered coil sensitivity needs to be considered regardless of using either

prospective or retrospective motion correction techniques or parallel imaging based scan acceleration is used.

Motion correction can also be achieved using information inherent in the MRI acquisition itself. Pipe et al. (1999) introduced the data acquisition with periodically rotated overlapping parallel lines with enhanced reconstruction (PROPELLER) that allows for intrinsic compensation for translational or rotational head motion during data acquisition. This technique is based on multiple-shot fast spin-echo (FSE), in which several k-space lines are acquired in each TR, forming a blade centered at the origin of k-space. The blade is then rotated around its center between shots, resulting in a k-space sampling pattern that resembles a propeller. The central disc of k-space is sampled by all blades and can be used as a 2D navigator. Comparison of this k-space disc between blades allows correction of the subject's in-plane rotation and translation, as well as identification of blades with corrupted data and exclusion of such blades from the final reconstruction.

The drawbacks of these methods are 1) computationally intensive during the reconstruction process; 2) the increased scan time related to redundant k-space sampling;, and 3) they might work well only for in-plane motion. They are generally inadequate for through-plane and/or large-scale motions, primarily because they cannot correct for the spin history effect (i.e., changes in saturation level of longitudinal magnetization due to motion-induced changes in the image-slice location).

2.5.2. Prospective Correction

The goal of PMC is to keep the acquisition field of view (FOV) constant, relative to the moving object. This implies that the FOV can be adapted to the object pose (position and orientation) by changing the gradient encoding and system RF settings. It is usually restricted to the correction of rigid body motion, for example, of the head. This section follows the idea of Maclaren et al. (2013).

2.5.2.1. Theory

Several theoretical descriptions of prospective motion correction exist (Manke et al., 2003; Nehrke et al., 2005; Shechter et al., 2004) and will not be repeated here. It is useful, however, to summarize the main results of their finding. It is assumed that a point in the imaged object undergoes a transformation with 12 degrees of freedom representing rotation, scaling, shearing, and translation. This transformation, which is generally referred to as an affine transformation, can be described by

$$\vec{x}'(t) = A(t)\vec{x} + \Delta\vec{x}(t) \qquad (2.24)$$

where $A(t)$ is a time-varying linear transformation (representing rotation, scaling, and shearing) and t(t) is a time-varying translation vector. The translation of the object, $\Delta\vec{x}(t)$, can be then compensated for by changing the radiofrequency (RF) transmit frequency and receiving phase. However, to compensate for $A(t)$, the original gradient waveform, $\vec{g}(t)$, must be transformed to $\vec{g}'(t)$ by

$$\vec{g}'(t) = A(t)\vec{g}(t) \qquad (2.25)$$

Eq. 2.25 states that to compensate for an affine transformation of the object, the gradient waveforms must be transformed by $A(t)$, meaning that they must undergo a rotation, scaling, or shearing (all linear operations). This is possible with conventional linear gradients (nonlinear warping, on the other hand, would not be correctable). However, the tracking device is usually limited to measure rigid body motion with 6 degrees of freedom (rotation and translation). In this case, it is assumed that only rigid-body motion occurs. Thus, the scaling and shearing operators are excluded from Eq. 2.25 and can be rewritten as:

$$\vec{g}'(t) = R(t)\vec{g}(t) \quad (2.26)$$

where the rotation matrix $R(t)$ represents the rotation of the image object over time. Thus, to correct for rotations, the read, phase, and slice-encoding gradients (the logical gradients) are represented by different combinations of the x, y, and z gradients (the physical gradients) as the object rotates (see Figure 2.6b).

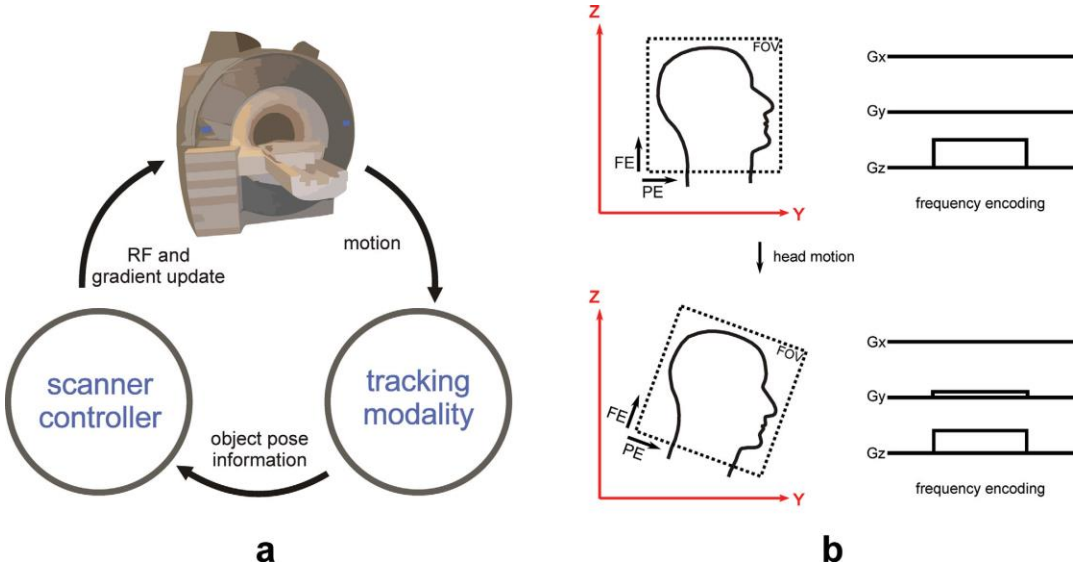

Figure 2.6. (a) Prospective motion correction uses tracking data describing the current pose of the imaged object to update the pulse sequence in real time. (b) After a rotation, gradient directions are modified so that any given voxel in the sample experiences the same field as it would have if the rotation had not occurred. This process necessitates the recalculation of the physical gradient waveforms that are needed to generate the desired logical gradient. In the example shown, the frequency encode gradient initially requires only one physical gradient, G_x; after head rotation, the frequency encode gradient requires both G_z and G_y.

2.5.2.2. Obtaining Tracking Data

In general, PMC applies motion detection techniques and adapts the MRI pulse sequence during its run-time (often referred to as real-time). Obviously, motion tracking techniques for PMC need to deliver pose information frequently and fast enough. The tracking techniques are usually classified as optical methods, field detection methods, and navigator methods.

Optical methods are completely independent from the MR sequence timing. They include laser systems (Eviatar et al., 1997), bend-sensitive optical fibers (Herbst et al., 2011), and camera systems. Camera systems have recently become popular, due to technology

improvements in both cameras and computing. Methods successfully used for motion correction include out-of-bore stereo camera systems (Speck et al., 2006; Zaitsev et al., 2006), out-of-bore single camera systems (Andrews-Shigaki et al., 2011), in-bore single camera systems (Aksoy et al., 2011; Qin et al., 2009), and in-bore systems with multiple cameras (Yancey et al., 2011). All currently used optical systems require a marker. Examples of markers include reflective spheres (Zaitsev et al., 2006), or new technology such as moiré phase tracking (Maclaren et al., 2012), which generates moiré patterns allowing accurate determination of through-plane rotations. The last example allows the use of particularly small targets (diameter 1.2 cm or less) with a single camera and has been shown to be a suitable alternative for conventional three dimensional (3D) motion capture (Weinhandl et al., 2010). Of course, in all of these examples, a marker must be rigidly attached to the head.

Field detection methods are a completely different approach with a long history in MRI. The scanner gradient fields are measured to localize the object. The method requires the use of a short sequences of pulses to obtain position information from a small sample of MR visible material fixed inside a miniature receive coil. This approach was first conceived in 1986, by Ackerman et al. (1986) for catheter tracking. Dumoulin et al. (1993) also pioneered developments in this area. A proof-of-principle study for slice-by-slice prospective motion correction using such a system was published by Derbyshire et al. (1998). More recent implementations, such as that of Ooi et al. (2011; 2009), refer to these as ‘‘active markers.’’ Active markers have been used for prospective motion correction in structural brain scans (Ooi et al., 2009) and in echo-planar imaging (EPI) (Ooi et al., 2011). A similar technique has been recently applied to measure gradient waveforms by Barmet et al. (2008; 2009), who decouple tracking from MR imaging by using RF-shielded probes and separate transmit/receive chains. Recently, they have also demonstrated the possibility of computing the probe position during simultaneous MRI by applying ‘‘tones’’ (Haeberlin et al., 2015) simultaneously with the conventional gradient waveforms. Field detection methods require several probes or active markers to be attached to the subject (a minimum of three markers are required, positioned noncollinearly and connected in a rigid arrangement).

MR navigators used for motion correction include navigators operating in k-space, such as cloverleaf navigators (van der Kouwe et al., 2006), orbital navigators (Fu et al., 1995; Ward et al., 2000), and spherical navigators (Welch et al., 2002) as well as image-based navigators, such as PROMO (White et al., 2010) or EPI navigators (Alhamud et al., 2012). K-space navigators repeatedly sample parts of k-space and quantify rotations and translations of the object by measuring rotations and phase shifts in the k-space data. Depending on the trajectory used, this can allow motion quantification in all 6 degrees of freedom. Image-based navigators use low-resolution images or volumes. These generally require longer time to acquire than k-space navigators but allow the user to define the region of interest for motion quantification, thus avoiding non-rigid regions (e.g., the neck). Alternatively, it is possible to detect, but not quantify, motion by comparing the relative intensity of a free induction decay signal between multiple receive coils (Kober et al., 2011). Navigator methods with sufficient accuracy for prospective motion correction all require unused time in the sequence to obtain accurate motion information [e.g., about 48 ms. for PROMO (White et al., 2010)], which makes them incompatible with some sequences. This spoils one of the main advantages of prospective correction, namely that the technique can be applied to most MR sequences. Nevertheless, if time in the sequence is available, as is often the case in spectroscopy, this method is very practical. Navigator methods have an advantage over optical tracking and field detection methods, in that they require no additional hardware and that there is no need for a marker to be attached to the subject.

2.5.2.3. Data Transfer and Sequence Update

Regardless of the tracking modality used (optical, field detection, or navigators), a key component of prospective correction involves the transfer of the pose estimation data to the imaging sequence. However, changing the tracking modality makes a significant difference to how this is performed. Navigator techniques, for example, often use the feedback facility made available by the scanner manufacturer. As this is vendor specific, it is not discussed here. In the case of external tracking systems, pose data are often computed on an external computer and sent to the scanner computer using a network

connection. For this purpose, data are sent via user datagram protocol (UDP) [e.g., (Andrews-Shigaki et al., 2011; Zaitsev et al., 2006)] or transmission control protocol (TCP) [e.g., (Feinberg et al., 2010; Qin et al., 2009)]. The initial position and orientation (pose) of the imaging volume is known and serves as the reference pose. During the scan only the differences between the current pose and its initial pose are required. The position and orientation of the imaging volume is then modified corresponding to these differences. The new imaging volume parameters are handed over to the scanner, which calculates the gradients and frequencies accordingly. The calculation requires time (typically milliseconds) and the updated gradient waveforms need to be transferred to the executing digital signal processor (DSP) before they can be applied. The procedure is soft- and hardware dependent but usually requires the identification of suitable periods within the sequence to insert the update mechanism.

Adjustments of the MR scanner's gradients and frequencies require the motion data in scanner coordinates. Following the terminology introduced in Zaitsev et al. (2006), referred to the process of determining the transform as cross-calibration. There are a number of ways in which this cross-calibration procedure can be performed. Aksoy et al. (2011; Forman et al., 2010) use a 60 s cross-calibration procedure based on a precisely manufactured marker (Forman et al., 2010) that is visible to both the scanner and the camera. Two other common approaches involve recording motion of a phantom using both the tracking system and the MR scanner (using image registration). Depending on the exact implementation details, these approaches are called iterative or non-iterative. The non-iterative approach involves collecting numerous datasets and solving for the transform that best fits the data. The iterative approach, as described in (Zaitsev et al., 2006), applies prospective correction using the latest version of the transform. If the transform is accurate, the resulting images will be perfectly aligned, due to motion correction. If the transform is inaccurate, then errors in the image alignment will result; these are used to fine-tune the transform. Calibration based on image registration can produce very good results, but there are several confounding effects to be aware of. These include field distortions (caused by rotating the phantom during calibration), gradient nonlinearities, and imperfect fixation of the tracking marker to the phantom.

2.6. Further Considerations after Rigid Body Motion Correction

PMC has been demonstrated to be efficient in the prevention of motion artifacts originating from displacements between acquisition steps as well as sequence specific motion effects such as signal dropouts due to dephasing or misalignment of the encoding direction for diffusion or flow measurements. PMC also accounts for spin-history effects when through-plane motion otherwise causes the magnetization to enter or exit the excited imaging volume. However, inherent tracking precision and accuracy (Maclaren et al., 2011) as well as delay between pose detection and sequence update can lead to residual artifacts that degrade correction data. Aksoy et al. (2012) described a hybrid prospective and retrospective correction method to mitigate the adverse effects of tracking errors. This involves retrospectively finding a transform by minimizing image entropy in a similar way to previous work by Atkinson et al. (1999). As k-space lines are rotated off the Cartesian grid, and a gridding reconstruction is used to resample the data. Their results show that application of the retrospective stage significantly improves image quality by reducing artifacts caused by poor cross-calibration.

However, large-scale motion may lead to other residual artifacts that cannot be compensated for with rigid body adjustment alone. The widely discussed artifact sources are with regard to the relative motion of the coil sensitivity (Aksoy Bammer, 2008; Banerjee et al., 2013; Luengviriya, 2010) as well as the geometric distortions caused by GNL (Hu et al., 2005; Polzin et al., 2004) and the object-induced static magnetic field inhomogeneity (ΔB_0) (Boegle et al., 2010; Ooi et al., 2013).

2.6.1. Relative Motion of Coil Sensitivity

Phased-array head coils have become the standard practice for state-of-the-art high resolution MRI of the brain. Phased-array head coils contain a number of surface coils, which are arranged in an integrated design which surrounds the head (e.g., 8-, 12-, or ever 32-channel head coils). A surface coil is only capable of receiving a signal near its spatial position and even though the sensitivity decreases with depth in the patient, images with very high local SNR can be obtained. The major advantage of a multichannel, phase-

array head coil is that it provides higher SNR and allows the application of parallel acquisition techniques, which can be used to speed up MRI. However, when motion occurs in measurements with stationary multi-coil receive arrays, the coil sensitivities will change relative to the moving object. This effect introduces erroneous signal intensity variations across the EPI time series. Not taking the coil sensitivities into account may therefore lead to misinterpretations of the BOLD signal. Even outside the scope of functional MRI (fMRI) applications, the existing literature on interactions between head motion, coil sensitivity and the quality of MRI results is rather limited at present. In one example, rotating a phantom after acquiring coil sensitivity map data was found to cause slight ghosting artifacts in images reconstructed using Generalized Auto-calibrating Partially Parallel Acquisitions (GRAPPA) (Zhao et al., 2008). Inter-scan head motion was also shown to perturb maps of coil sensitivity and to have a negative impact on the accuracy of quantitative T1 mapping (Papp et al., 2015). Another study that investigated the use of the iterative self-consistent parallel imaging reconstruction (SPIRiT) method (Lustig et al., 2010) showed that residual aliasing remained if a subject moved between acquisitions of the coil sensitivity map and the under-sampled images (Tian et al., 2015). Such artifacts appear more prominently in parallel imaging with high reduction factors and for arrays of small receiver coils with strong sensitivity profile variations in space.

2.6.2. Gradient Nonlinearity Induced Geometrical Distortion

Conventional image reconstruction techniques in clinical magnetic resonance imaging (MRI) typically assume that spatial encoding is performed with gradient fields that vary linearly across the entire imaging FOV. In practice, however, the gradient fields inevitably contain a higher order; nonlinear components due to engineering limitations or manufacturing imperfections; or to reduce peripheral nerve stimulation (Glover et al., 1986; Harvey et al., 1999). The unaccounted *GNL* causes image geometric distortion and negatively affects applications where high geometric accuracy is required, such as large-scale longitudinal studies and pretreatment planning (Chen et al., 2006; Doran et al., 2005; Gunter et al., 2009; Janke et al., 2004b; Schad et al., 1992). In stationary MR

imaging, *GNL* effects are seen as warping (geometric distortions) of the object particularly at the edges of large FOV, which can be corrected since the gradient field distribution is known (Jovicich et al., 2006). Unlike in static imaging, motion during the acquisition with *GNL* leads to blurring in addition to spatial distortion because imaging data acquired at multiple object locations within the non-linear gradient fields have different geometry. Thus, the k-space data of the object become inconsistent between phase encoding steps. This effect is again strongest in peripheral regions (Hu et al., 2005; Polzin et al., 2004), and has not been studied in relation to prospective motion correction for MRI.

2.6.3. Tissue Magnetic Susceptibility Induced Geometrical Distortion

Motion-induced magnetic field changes may occur due to the main magnetic field inhomogeneity and object induced field changes. These local magnetic field changes are frequently considered as the main source of geometric distortions (Jezzard et al., 1995; Jezzard et al., 1999; Ooi et al., 2013). They are most prominent in EPI, which is very sensitive to field inhomogeneity due to the low effective phase-encoding bandwidth. These static geometric distortions can be considered after the image reconstruction using the pixel shift method (Jezzard et al., 1995). Recently, the size and location of B_0 field shifts within the brain at 7T for different types of head movement were studied by Sulikowska et al. (2014). Their results showed that the maximum B_0 field changes at the frontal lobe for pitch and yaw rotations were 4±2 and 8±11 Hz/degree, respectively. Other authors have reported maximum B_0 field differences caused by head movement of 160 Hz at 2.89T (Maclaren et al., 2013) and 50 Hz at 3T (Jezzard et al., 1999). The local field changes strongly depend on the subject orientation. Consequently, PMC at high field may be impacted by this variation even in conventional sequences (i.e., Spin-Echo and Gradient-Echo) with low readout-bandwidth (BW) that are often chosen to optimize SNR or CNR ratios in structural imaging.

2.7. Image Reconstruction for MRI

The inverse fast Fourier transform (FFT) has served the MR community very well as the conventional image reconstruction method for k-space data with Cartesian sampling. Unfortunately, in the presence of motion or non-uniform sampled MRI (Atkinson et al., 2003; Fessler et al., 2003), the inverse FFT is unable to be directly applied to reconstruct the images. Discrete Fourier transformation is a possible method with a much heavier computation burden. Currently, the widely used method is to first regrid the samples onto regular Cartesian grid, and then to apply inverse FFT. These methods include gridding (Jackson et al., 1991; Meyer et al, 1992; O'Sullivan, 1985), non-uniform FFT (NUFFT) (Dutt et al., 1993; 1995; Fessler et al., 2003; Nguyen et al., 1999), etc.

2.7.1. Fourier Theorems

2.7.1.1. Fourier Shift Theorems

Let $m(k_x, k_y)$ be the Fourier transform of a 2-D object $\rho(x, y)$ as stated in Eq. 2.27.

$$m(k_x, k_y) = \Im\{f(x, y)\} = \iint_{xy} \rho(x, y) e^{-2\pi i[xk_x + yk_y]} dxdy \quad (2.27)$$

Let $m'(k_x, k_y)$ be the Fourier transform of $\rho(x + \Delta x, y + \Delta y)$, a translated version of $\rho(x, y)$

$$m'(k_x, k_y) = \Im\{\rho(x + \Delta x, y + \Delta y)\}$$
$$= \iint_{xy} \rho(x + \Delta x, y + \Delta y) e^{-2\pi i[xk_x + yk_y]} dxdy \quad (2.28)$$

If one makes the substitution $x' = x + \Delta x$ and $y' = y + \Delta y$, the result is

$$m'(k_x, k_y) = \iint_{x'y'} \rho(x', y') e^{-2\pi i[(x' - \Delta x)k_x + (y' - \Delta y)k_y]} dx'dy'$$

$$= e^{2\pi i[\Delta x k_x + \Delta y k_y]} \iint_{x'y'} \rho(x', y') e^{-2\pi i[x' k_x + y' k_y]} dx' dy' \quad (2.29)$$

The integral in Eq. 2.29 is the same as in Eq. 2.27. Thus, the Fourier transform of the shifted object is equal to the original Fourier transform with additional phase terms at each location of k-space dependent on the $(\Delta x, \Delta y)$ shifts as shown in Eq. 2.30.

$$m'(k_x, k_y) = e^{2\pi i[\Delta x k_x + \Delta y k_y]} m(k_x, k_y) \quad (2.30)$$

2.7.1.2. Fourier Rotation Theorem

Let $\rho'(x, y)$ be equivalent to $\rho(x', y')$ which is a rotated version of $\rho(x, y)$

$$\rho'(x, y) = \rho(x', y') = R\{\rho(x, y)\} \quad (2.31)$$

where the rotation transformation matrix R is defined by

$$R = \begin{bmatrix} \cos\theta & -\sin\theta \\ \sin\theta & \cos\theta \end{bmatrix} \quad (2.32)$$

making the new coordinates $x'$and y'equal to

$$\begin{bmatrix} x' \\ y' \end{bmatrix} = \begin{bmatrix} \cos\theta & -\sin\theta \\ \sin\theta & \cos\theta \end{bmatrix} \begin{bmatrix} x \\ y \end{bmatrix}$$
$$x' = x\cos\theta - y\sin\theta$$
$$y' = x\sin\theta + y\cos\theta \quad (2.33)$$

where θ is the rotation angle about the origin. The Fourier transform $m'(k_x, k_y)$ of $\rho(x, y)$ is given by

$$m'(k_x, k_y) = \iint_{xy} \rho'(x, y) e^{-2\pi i[x k_x + y k_y]} dx dy \quad (2.34)$$

Using a change of variables to x' and y' we have

$$m'(k_x, k_y) = \iint_{xy} \rho(x', y') e^{-2\pi i[(x'\cos\theta + y'\sin\theta)k_x + (-x'\sin\theta + y'\cos\theta)k_y]} dx' dy' \quad (2.35)$$

where the substitutions for x and y have been made according to

$$\begin{aligned} x &= x' \cos\theta + y' \sin\theta \\ y &= -x' \sin\theta + y' \cos\theta \end{aligned} \tag{2.36}$$

Rearranging the exponents to be in the canonical form produces

$$\begin{aligned} m'(k_x, k_y) &= \iint_{xy} \rho(x', y') e^{-2\pi i [x'(k_x cos\theta + k_y sin\theta) + y'(k_x sin\theta + k_y cos\theta)]} dx' dy' \\ &= \iint_{xy} \rho(x', y') e^{-2\pi i [x' k'_x + y' k'_y]} dx' dy' \\ &= m(k'_x, k'_y) \end{aligned} \tag{2.37}$$

where the new k-space coordinates k'_x and k'_y are related to the original k-space coordinates k_x and k_y by

$$\begin{aligned} \begin{bmatrix} k'_x \\ k'_y \end{bmatrix} &= \begin{bmatrix} \cos\theta & -\sin\theta \\ \sin\theta & \cos\theta \end{bmatrix} \begin{bmatrix} k_x \\ k_y \end{bmatrix} \\ k'_x &= k_x \cos\theta - k_y \sin\theta \\ k'_y &= k_x \sin\theta + k_y \cos\theta \end{aligned} \tag{2.38}$$

which is the same rotational transformation of the spatial domain coordinates expressed in Eq.2.33. Therefore we can say that $m'(k_x, k_y)$ is equal to the original Fourier transform $m(k_x, k_y)$ after it has been rotated to the coordinate frame of (k'_x, k'_y). In other words, the rotation of the object caused an equivalent rotation of its conjugate k-space.

2.7.2. Gridding Reconstruction Algorithm

When k-space is sampled on a uniform grid, an inverse FFT can be used to quickly reconstruct the image. The computational advantage of the FFT can be used for non-Cartesian k-space trajectories if the data is first interpolated or gridded onto a uniform grid and then applied to the inverse FFT. The most general and currently widely used method of reconstruction in MRI is referred to as the gridding reconstruction algorithm (Jackson et al., 1991; Meyer et al, 1992; O'Sullivan, 1985). As illustrated in Figure 2.7,

all the non-Cartesian points in a certain distance Δ (window width) interpolate on the Cartesian grid point in the center.

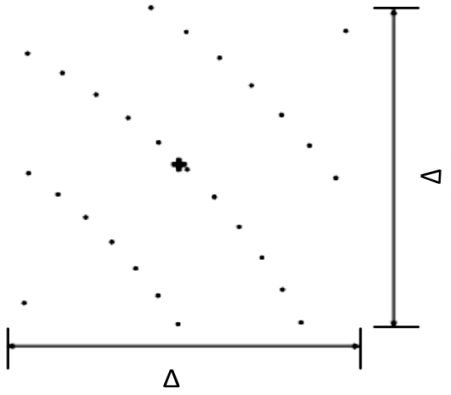

Figure 2.7. Gridding interpolation, the "+" denotes a Cartesian grid point which value is unknown and the "·" represent the surrounding non-Cartesian samples which contribute to the interpolation on "+". Δ is the width of the convolution kernel. (from Xuguang, 2011).

The entire method is summarized by the following equation.

$$M_c = \{[(M \cdot S \cdot W) \otimes C] \cdot R\} \otimes^{-1} C \qquad (2.39)$$

where M_c is the data in k-space gridded onto a Cartesian grid, $M \cdot S$ is the sampled data on the k-space trajectory, W is the density compensation function, C is the convolution function used for gridding the data, R denotes the Cartesian grid sampling function, and $\otimes$ denotes convolution. There are four main steps to gridding:

- Multiply the data that is sampled on the k-space trajectory, $M \cdot S$ with a density compensation function, W, to account for the unequal sampling of k-space.
- Convolve the weighted data with a chosen convolution function, C, and resample onto a Cartesian grid, R.
- Apply an inverse FFT to reconstruct an image.

- Perform deapodization to remove the effect of the convolution function by dividing the result by the Fourier Transform of the convolution function, this is denoted by $\otimes^{-1}$ in Eq. 2.39.

In the first step, the non-uniform sampling density is usually corrected by a density compensation function, or DCF. The DCF can be defined and computed in a variety of ways. This step is important in reducing the reconstruction error in the image. Jackson et al. (1991) introduced a numerical method called the area density function, or ADF, as density compensation. An iterative method which extends the ADF was provided by Pipe et al. (1999). Meyer et al. (1992) introduced an analytic function as the DCF for spiral sampling trajectory. Hoge et al. (1997) described another analytic DCF for spiral trajectory which is based on the Jacobian determinant for the transformation between the Cartesian grid and the spiral trajectory parameters of time and interleaf rotation angle. Rasche et al. (1999b) proposed a Voronoi-diagram method to compute DCF. The DCF is the inverse of the area of the Voronoi cell around each sample. The Voronoi-diagram approach is a powerful method to compute the local density. It can be used on both 2D and 3D problems.

The optimal gridding method is to first convolve with an infinite sinc function and then perform resampling (O'Sullivan, 1985). For practical reasons, this infinite function needs to be replaced by a finite convolving function. This finite convolution kernel will contribute two artifacts into the reconstructed image. Firstly, the inverse of the Fourier transform of this kernel has side lobes, which will be aliased back to the image causing an artifact. Also, the central lobe is typically not flat. It shows a roll-off effect. Thus the intensity of the image is changed. This can be corrected by a post-compensation step, which requires dividing the image by this central lobe. Jackson et al. (1991) compare the performance of several kinds of kernels including two-term cosine (Hamming window, Hanning window), three-term cosine (Blackman window), Gaussian window and Kaiser-Bessel kernel, and conclude that in the sense of minimum aliasing energy in the reconstructed image, the Kaiser-Bessel kernel with an optimal parameter is the best choice. To reduce the artifact in the reconstructed image, an over-sampling ratio is

applied to the reconstruction. Gridding is usually applied on a larger (denser) grid in k-space, and then only the center region of the image after inverse FFT is kept (Jackson et al., 1991; Moriguchi et al., 2000; Rosenfeld, 1998). Typically a double sized (2x) grid, which corresponds to over-sampling ratio of 2, is used.

Gridding is widely used due to its simple and easy implementation. The kernel width is typically small, 2-4 according to Jackson et al. (1991), making it still a fast algorithm to implement. However, one drawback of the gridding method is the definition and computation of the density compensation. This is typically time consuming.

2.7.3. Non-Uniform Fast Fourier Transform (NUFFT) reconstruction Algorithm

In non-uniform Cartesian MRI, the Fourier transformation from image was remapped to a non-uniform k-space grid. This is achieved by interpolating the uniformly spaced samples to the non-uniform sample locations. Instead of k-space interpolation of the grids, it is possible to directly calculate the non-uniform Fourier transform by means of the non-uniform discrete Fourier transform (NDFT). The NDFT has the form:

$$X(\omega_m) = \sum_{n=0}^{N-1} x_n e^{-i\omega_m n}, \qquad m = 1, \dots, M \qquad (2.40)$$

where x_n are equally-spaced signal samples, ranging from 1 to N and ω_m, the non-uniformly spaced frequency nodes ranging from 1 to M. The Fourier transform thus needs to be computed for every non-uniform frequency node. The result of the NDFT is exact but has a computational cost of $O(MN)$ operations. In real-world applications, the computation time required by the NDFT will be too large to be practical. The NUFFT is an approximation of the NDFT that allows a fast solution to the non-uniform transform problem. Since the introduction of the technique by Dutt and Rokhlin (1993), several NUFFT methods have been proposed (Beylkin, 1995; Liu et al., 1998). The NUFFT has been extended to multidimensional transforms (Greengard et al., 2004; Sarty et al., 2001). In this study we use the NUFFT implementation by Fessler et al. (2003).

Mathematically, the NUFFT can be described by:

$$Y_k = \sum_{n=0}^{N-1} x_n e^{-i\frac{2\pi}{K}kn}, \quad k = 1, \dots, K-1 \qquad (2.41)$$

$$\hat{X}(\omega_m) = \sum_{j=0}^{J} Y_{(k_m+j)} u_j(\omega_m), \quad m = 1, \dots, M \qquad (2.42)$$

where Y_k denotes the resampled FFT with K points of signal x and $\hat{X}(\omega_m)$ is the approximated non-uniform frequency samples of signal x. The $u_j(\omega_m)$'s are the appropriate frequency interpolation coefficients (Fessler et al., 2003) and J is the neighborhood size used in the interpolation. Determining the optimal interpolation coefficients and applying them in a computationally efficient manner (through pre-computing) is a key to all NUFFT methods.

There are many ways to choose the interpolation function. Dutt et al. (1993) introduced a Gaussian based interpolation. Starty et al. (2001) proposed a generalized FFT (GFFT) and demonstrated that a Gaussian kernel can provide a more accurate reconstruction compared to the Kaiser-Bessel based gridding method. Beylkin (1995) used the B-spline based interpolation. Anderson et al. (1996) took the Taylor series expansion method. Fessler et al. (2003) introduced a min-max interpolation, which is a fixed-width interpolator that minimizes the worst case approximation error of all signals with unit norm. Sha et al. (2003) used a similar criterion by using a kernel matrix that fit for the k-space trajectory in the sense of least square approximation error. The performance of the NUFFT method with min-max interpolation was shown to be more accurate than other interpolation methods.

2.7.4. The Gridding versus the NUFFT

The gridding operation is a method to interpolate the grid data based on the non-equally spaced samples. The k-space operation includes a density compensation, convolution and resampling. Note that the gridding operation is in k-space only; the entire reconstruction

process contains an "interpolation" step followed by inverse FFT. On the other hand, NUFFT reconstruction directly relates the image and the k-space samples, making the Fourier transformation an embedded step. The reconstruction procedure is a loop of FFT, interpolation and image updating. Moreover, NUFFT is not only applicable for non-uniform k-space but also for non-uniform image space (image distortion) known as type-1 of NUFFT (Greengard et al., 2004). In addition, an iterative NUFFT is also easy to incorporate regularizations based on image processing techniques such as smoothing, edge-preserving, etc. (Sutton et al., 2003).

2.7.5. Augmented Sensitivity Encoding Reconstruction Algorithm

Augmented SENSE reconstruction was recently introduced in order to retrospectively correct the rigid body motion in MRI of the brain. This reconstruction also addressed the effect of relative motion of a receiving sensitivity field. Here, we briefly describe the motion effect and correction of the resulting artifacts. A full description can be found in the article by Bammer et al. (2007).

An MR signal, m, sampled at time t_i (i.e., at a point $k(t_i)$ in k-space) relates to the object v in the spatial domain r_u as

$$m(t_i) = \sum_u v(r_u) \exp^{-jk(t_i)\cdot r_u} \qquad (2.43)$$

and the matrix of signals, m, from the entire measurement can be expressed as

$$m = \boldsymbol{E}v \qquad (2.44)$$

where $\boldsymbol{E}$ is the so-called forward or encoding operator. In Cartesian-sampled MRI with linear gradient fields and one homogeneous receiver coil, this operator only consists of a discrete Fourier transformation (DFT).

In cases of non-uniform sampling, $k(t_i)$ is not on a uniform Cartesian grid and the simple matrix $\boldsymbol{E}$ in Eq. 2.44 should be replaced by the gridding method (Jackson et al., 1991; Rasche et al., 1999a), so

$$m = \boldsymbol{G}_{F\_kspace}\boldsymbol{F}v \qquad (2.45)$$

where $\boldsymbol{F}$ represents fast Fourier transformation and $\boldsymbol{G}_{F\_kspace}$ is a forward resampling operator transferring the k-space data from a uniform Cartesian to a non-uniform Cartesian grid.

Now we consider the motion effect on the MR signals. The motion of the object is described by a matrix $\boldsymbol{\Omega}$ and its inversion $\boldsymbol{\Omega}_{inv}$, whereas $\boldsymbol{\Lambda}$ is the corresponding transformation rule to $\boldsymbol{\Omega}$ in k-space. The operator $\boldsymbol{\Omega}$ acts on an unperturbed image v_0 which results in a motion-corrupted image v:

$$v = \boldsymbol{\Omega}v_0 = \boldsymbol{F}^H\boldsymbol{\Lambda}\boldsymbol{F}v_0 \qquad (2.46)$$

with $\boldsymbol{F}^H$ is inverse fast Fourier transform. The MR signals relate to the unperturbed image as

$$m = \boldsymbol{G}_{F\_kspace}\boldsymbol{\Lambda}\boldsymbol{F}v_0 \qquad (2.47)$$

In the presence of motion, solving Eq. 2.47 leads to the unperturbed image.

For multi-channel imaging, the signal at time t_i from a coil q can be described as the sensitivity encoding equation (Preussmann et al., 1999):

$$m_q(t_i) = \sum_u v(r_u)c^q(r_u)\exp^{-jk(t_i)\cdot r_u} \qquad (2.48)$$

where $c^q(r_u)$ is the complex spatial receive sensitivity of coil q. In matrix form, the encoding matrix $\boldsymbol{E}$ can be calculated as $\boldsymbol{F}\cdot diag(c^q)$. If the object moves while the coil is fixed with respect to the FOV, the MR-signal matrix from each coil would be

$$m_q = \boldsymbol{G}_{F\_kspace}\boldsymbol{\Lambda}\boldsymbol{F}diag(\boldsymbol{\Omega}_{inv}c^q)v_0 \qquad (2.49)$$

More explicitly, the encoding matrix $\boldsymbol{E}$ which is specific to pose p and coil q can be defined as

$$\boldsymbol{E}^{p,q} = G^{p}_{F\_kspace}\boldsymbol{\Lambda}^{p}\boldsymbol{F}diag\left(\boldsymbol{\Omega}^{p}_{inv}c^{q}\right) \qquad (2.50)$$

Eq. 2.49 shows that, in principle, the exact unperturbed image is obtained only after the two transformations in spatial and Fourier spaces are taken into account. In the text, we refer to two different processes of motion correction involving $\boldsymbol{G}_{F\_kspace}\boldsymbol{\Lambda}$ and $\boldsymbol{\Omega}_{inv}c^{q}$ as signal and sensitivity map correction, respectively.

It is obvious that the encoding scheme in Eq. 2.50 appears much more complex than the conventional Fourier encoding as shown in Eq. 2.44. This linear system is too large to be handled by the direct inverse methods. Thus, desired image v_0 corresponding to the encoding operator in Eq.2.43 was generally estimated via a linear least-square approach that minimizes the squared Euclidean norm of the residual (Eq. 2.51) using the conjugate gradient (CG) method.

$$\min_{v_0}\left\{\sum_{p,q}\|m^{p,q} - \boldsymbol{E}^{p,q}v_0\|_2^2\right\} \qquad (2.51)$$

❖ **The Conjugate Gradient (CG) Algorithm**

The method of conjugate gradient describes a class of iterative techniques having the property of guaranteed convergence in a finite number of iterations (Golub et al., 1996). Also, even when the system is ill conditioned, good estimates of the largest and smallest eigenvalues are not needed to determine the algorithm parameters. The basic idea of this method is to eliminate the residual error (i.e., the difference between the right-hand and left-hand sides of the linear system equation) along directions that are all mutually orthogonal with under transformation with the system matrix and spanning the space of the solution. The original formulation of this iteration requires the system to be real, square, symmetric and positive definite for the algorithm to work and provide a unique solution to the system. The conjugate gradient algorithm for solving the normal equation $\boldsymbol{E}^H\boldsymbol{E}v = \boldsymbol{E}m$ ($\boldsymbol{E}^H$**:** a complex conjugate of $\boldsymbol{E}$) is shown below.

1. Compute the intermediate image $a = \boldsymbol{E}^H\boldsymbol{m}$**.**
2. Set the initial solution $v_0 = 0$.
3. Set the initial residual $r_0 = a$.
4. Set the first direction $p = a$.
5. Update the solution in CG loop;

for i=0, 1, 2,…Nit (Nit: number of iterations)

$$q = \boldsymbol{E}^H\boldsymbol{E}p$$

$$v_{i+1} = v_i + \frac{r_i^H r_i}{p^H q}p$$

$$r_{i+1} = r_i - \frac{r_i^H r_i}{p^H q}p$$

$$p = r_{i+1} + \frac{r_{i+1}^H r_{i+1}}{r_i^H r_i}p$$

end

CHAPTER 3

3. CORRECTION OF RELATIVE MOTION OF COIL SENSITIVITY

The work presented in this chapter was accepted as a poster presentation:

Yarach U, Stucht D, Godenschweger F, Speck O. The Correction of Motion-Induced Coil Sensitivity Miscalibration in Parallel Imaging with Prospective Motion Correction. *In: Proceedings of the 23rd Annual Meeting of the ISMRM, 2015, Toronto, Canada.*

3.1. Preface

It is now commonplace in MRI to use multichannel receiver coils that increase SNR and enable parallel imaging reconstruction approaches, but which inevitably have non-uniform spatial sensitivity. When motion occurs in measurements with stationary multi-coil receive arrays, the coil sensitivities will change relative to the moving object. With PMC, the coil sensitivities effectively move relative to a stationary object. The interactions between head motion and receive radiofrequency (RF) coils result in the variation of signal amplitude and phase, leading to shading artifacts particularly when applying the parallel MR imaging (Atkinson et al. 2004, Banerjee et al. 2013). Recently, this effect in inter-scan motion was observed; it introduced erroneous signal intensity variations across the EPI time series, and also generated a negative impact on the accuracy of quantitative T1 mapping (Papp et al., 2015). Their studies show the improvement of parameter maps when addressing the effect of inter-scan motion on the receiving sensitivity field.

Several MRI applications (Brown et al., 2010; Stucht et al., 2015) require very high spatial resolution which can be achieved by high field MRI systems, such as 7T scanners. However, high resolution scans may require long acquisition times, which in turn increase the discomfort for the subject and the risk of intra-scan motion. Although the rigid body motion within intra-volume can be successfully corrected by PMC, the relative

motion of coil sensitivity may increase the variation of quantitative MR parameter maps (Callaghan et al., 2015).

In this chapter, we demonstrate a systematic study quantifying artifacts from the relative motion of coil sensitivity within intra-scan motion data with PMC enabled, and the necessity of the sensitivity profile correction step, which was proposed by Bammer et al. (2007), termed augmented SENSE reconstruction as described in section 2.7.5. Both fully-sampled and under-sampled MR data acquired at different motion scales were observed.

3.2. Theory

We remind the readers that this chapter attempts to investigate the effect of the relative motion of coil sensitivity within the intra-scan dataset which was acquired using the uniform Cartesian sampling technique. In rigid body motion, the Eq. 2.49 describes the corrupted MR signals that are acquired by either uniform Cartesian or non-uniform Cartesian sampling techniques, since both cases require the gridding operator to resample the motion data. In the next section we describe the encoding operator of Cartesian MR signal after applying PMC.

3.2.1. The Encoding Operator

The motion corrupted MR signal received from multiple coil arrays is described in Eq. 2.49. With highly accurate PMC, the object motion $\boldsymbol{\Omega}$ can be fully compensated by the gradient rotation matrix $\boldsymbol{\Omega}_{PMC}$ determined by the tracking system consisting of six parameters of rigid body motion (i.e, $\boldsymbol{\Omega} \cdot \boldsymbol{\Omega}_{PMC} = \boldsymbol{\Lambda} \cdot \boldsymbol{\Lambda}_{PMC}$ = ***Id, Id:*** identity matrix). This means that the PMC can maintain k-space consistency during the data acquisition. Thus, k-space gridding ($\boldsymbol{G}_{F\_kspace} \cdot \boldsymbol{\Lambda}$**)** is no longer required, the encoding operator with PMC can simplify to

$$\boldsymbol{E}^{p,q} = \boldsymbol{M}^{p}\boldsymbol{F}\boldsymbol{C}^{p,q} \qquad (3.1)$$

For simplicity, the coil sensitivity of channel q specific to object pose p ($\boldsymbol{C}^{p,q}$) was used here instead of $diag\{\boldsymbol{\Omega}_{inv}^{p} c^{q}\}$. $\boldsymbol{M}^{p}$ is a Cartesian sampling mask (1=sampled, 0=otherwise).

The key information required for Eq. 3.1 is information on the spatial distribution of the RF coil sensitivities**.** In general, the sensitivity information can be obtained with any established sensitivity estimation method (Bydder et al., 2002a; Griswold et al., 2006; Lin et al., 2003; Pruessmann et al., 1999). For example, the sensitivity map can be obtained with an additional body coil image that is assumed to have homogeneous sensitivity. In the absence of a body coil image, the square-root of the sum-of-squares (RSS) image can also be used. Another common method is to use a low resolution image that is either acquired with an extra navigator or with a self-navigated trajectory, for example a variable density spiral (Kim et al., 2003). The self-navigation approach avoids the need for a separate calibration scan and errors from mis-registration. The separate calibration scan based method for coil sensitivity estimation is described in detail in (Pruessmann et al., 1999) and is illustrated in Figure 3.1.

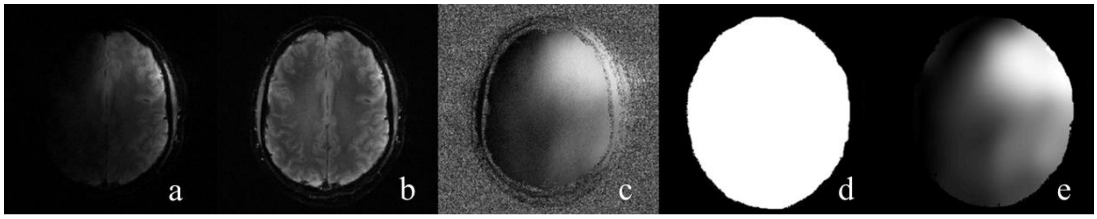

Figure 3.1. Illustration of the sensitivity map determination. The ratio between an individual surface coil image (a) and a body coil image (b) gives the surface coil sensitivity estimate (c). The object support mask (d) is generated using the threshold point of the reference image. To reduce noise, a local polynomial fit is applied in the limits of the object mask to get a smoothed sensitivity map (e).

3.2.2. Image Reconstruction Algorithm

In general, the desired reconstructed images v_0 encoded by the operator $\boldsymbol{E}$ in Eq.3.1 can be obtained by the standard CG method. However, this method may exhibit unstable

convergence behavior. This is because the encoding matrix seems seriously ill-conditioned due to the large dimension used, as well as the fact that the measured data is usually corrupted by noise. To overcome this difficulty, L2-regularization was also incorporated,

$$\min_{v_0}\left\{\sum_{p,q}\|m^{p,q}-\boldsymbol{E}^{p,q}v_0\|_2^2+\lambda\|\boldsymbol{L}v_0\|_2^2\right\} \qquad (3.2)$$

The regularization parameter λ (lambda) is a positive real constant, and $\boldsymbol{L}$ is here an identity matrix. The processing steps of iterative reconstruction for the present purpose are as follows:

Prior iteration, the intermediate image a is estimated by summing all products of multiplication between the matrix $\boldsymbol{E}^{(p,q)H}$ and the measured data vector $m^{i,j}$. $\boldsymbol{E}^{(p,q)H}$ is an inversion of $\boldsymbol{E}^{(p,q)}$ in Eq. 3.1, termed decoding or a reconstruction operator. It consists of the inverse FFT ($\boldsymbol{iF}$) and the complex conjugate of the coil sensitivity ($\boldsymbol{C}^{(p,q)*}$).

$$a=\sum_{p,q}\boldsymbol{E}^{(p,q)H}\cdot m^{p,q}=\sum_{p,q}\boldsymbol{C}^{(p,q)*}\cdot\boldsymbol{iF}\cdot m^{p,q},$$

$$p=1,\dots,N,q=1,\dots,N_c \qquad (3.3)$$

N is the total pose number, and N_c is the total channel number.

During iteration, the proposed reconstruction algorithm consists of four steps in each iteration: data encoding, data decoding, channel and pose combination, and the CG unit. Given the vector residuum $w^{(n)}$ ($w^{(0)}=a$) from the previous iteration n, the current iteration of number $n+1$ is carried out as follows.

Step 1, data encoding of pose p, channel q:

$$d^{p,q}=\boldsymbol{E}^{(p,q)}w^{(n)}=\boldsymbol{M}^{p}\cdot\boldsymbol{F}\cdot\boldsymbol{C}^{p,q}w^{(n)} \qquad (3.4)$$

The previous $w^{(n)}$ is encoded by $\boldsymbol{E}^{(p,q)}$ to get the partial k-space data of each pose and channel $d^{p,q}$. This step consists of coil-wise multiplication by coil sensitivity, followed by FFT, and then multiplied by the sampling mask. The sampling mask keeps only acquired k-space lines, the rest are set to zeros.

Step 2, data decoding of pose p, channel q:

$$h^{p,q} = \boldsymbol{E}^{(p,q)H} \cdot d^{(p,q)} = \boldsymbol{C}^{p,q*} \cdot \boldsymbol{iF} \cdot d^{p,q} \qquad (3.5)$$

The partial k-space data $d^{p,q}$ are reconstructed by $\boldsymbol{E}^{(p,q)H}$, obtaining the partial image of each pose and channel $h^{p,q}$. This step performs inverse FFT, followed by an individual weighting by a complex conjugate of coil sensitivity.

Step 3, channel and pose combination:

$$I_{comb} = \sum_{p}^{N} \left\{ \sum_{q=1}^{N_c} h^{p,q} \right\} \qquad (3.6)$$

The partial complex image $h^{p,q}$ of different channels and poses are combined.

Step 4, the CG unit: (L2-norm based regularization)

Finally, the combined image I_{comb} is fed back into the CG unit. The residuum after CG is then used as the initialization for the next iteration.

A schematic diagram of the proposed algorithm is shown in Figure 3.2. The four steps above are repeated until the maximum iteration number or the stopping criteria are reached.

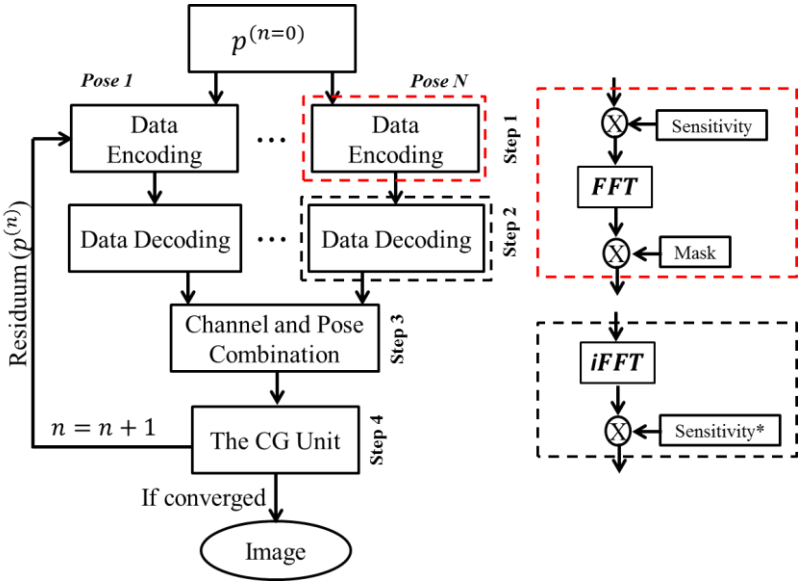

Figure 3.2. Schematic diagram of the augmented CG-SENSE. The main diagram of the four steps in each iteration is shown on the left. The right diagram shows the implementation details of the data encoding (red dashed box) and the data decoding (black dashed box). The notation * denotes complex conjugate.

The performance of both reconstruction techniques were evaluated by calculation of the root mean square error (RMSE), which was computed as

$$\mathrm{RMSE} = \sqrt{\frac{\sum_{k=1}^{n}[im(k) - ref(k)]^2}{n}} \qquad (3.7)$$

where ref is the reference image (no motion) and im is the reconstructed image, n denotes the total number of pixels.

3.3. Materials and Methods

3.3.1. Numerical simulations

The artifact quantification and the performance of the augmented SENSE were first tested in numerical simulations using a Shepp-Logan phantom assuming a 2D axial

image (FOV=256 mm^2, pixel size=1 mm^2). The ideal prospective motion correction was assumed. This means that the coil sensitivity profiles moved around the static phantom. The data encoding in Eq. 3.3 was applied to the static phantom in order to generate the motion-corrupted MR signal of each pose and channel $d^{p,q}$. The $\boldsymbol{C}^{p,q}$ was simulated using Biot–Savart's law (Ulaby, 1997). It is assumed that the coils are placed in space such that the coil plane is parallel to the B_0 field. The coils are circular, with centers which are equidistant to the origin, and their axes are uniformly distributed radii (See the illustration of the setup in Figure 3.3).

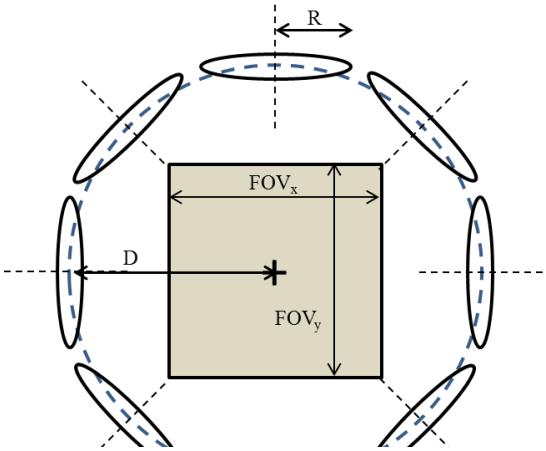

Figure 3.3. Coil array setup for the generation of sensitivity maps.

The 8-channel coil (D=1.2xFOV/2, R=100 mm.), and the highly localized 12-channel coil (D=1.2xFOV/2, R=70 mm.) were used. The example of 1st channel profiles from 8- and 12-channel coils are illustrated in Figure 3.4a. Since the sensitivity profiles changed much more during rotations about its circular cross section, than during translations along its longitudinal axis, therefore, only in-plane rotation (around the z-axis) was observed in this study. The rotation pattern shown in Figure 3.4b that creates 8-time motion for each dataset (i.e., N=8, 32 k-space lines along phase direction per pose) were applied to rotate the sensitivity profiles around the object. This pattern was scaled by factors 2.5, 5, 7.5, and 10 to create the maximum rotations of 5, 10, 15, and 20 degrees, respectively. These same patterns with different motion amplitudes were applied to simulate the corrupted k-space data in multiple RF receiver coils (N_c= 8, and 12). Note that identical information

as used in artifact generation was applied in the correction process when using the augmented SENSE reconstruction. On the other hand, only the coil sensitivities specific to the initial pose were employed in conventional SENSE.

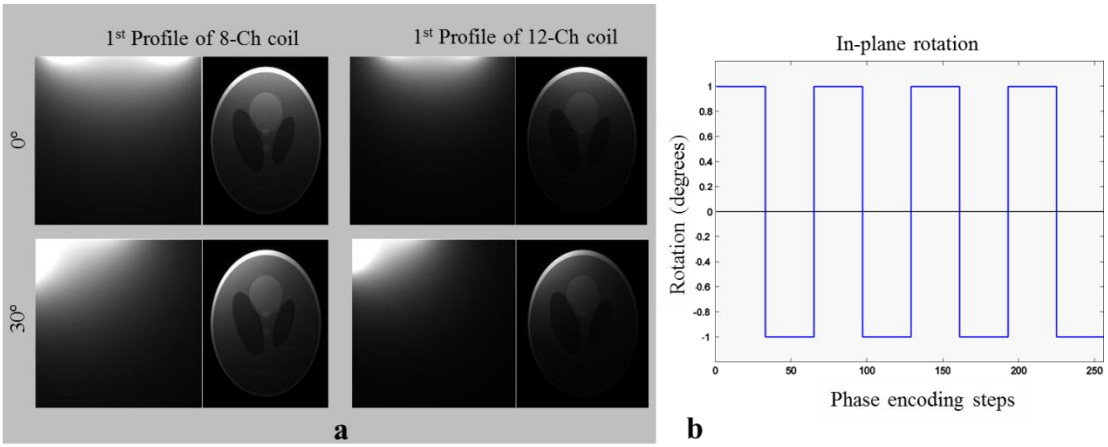

Figure 3.4. (a) The example of 1st channel profiles from 8- and 12-channel simulated coils. The 12-ch coil shows more localized signal than the 8-ch coil. With PMC enabled, the sensitivity profile seemed to be rotated by -30 degrees when the subject rotated 30 degrees (lower row). (b) The in-plane rotation pattern was used to simulate the MR corrupted signal.

3.3.2. MRI Experiments

All experiments were performed on an ultra-high field whole-body 7T MRI scanner (Siemens Healthcare, Erlangen, Germany) equipped with a 70mT/m whole body gradient system (SC72). PMC was performed with a tracking system consisting of a single camera mounted inside the scanner bore and a tracking marker with a multilayer structure, which generates moiré patterns for accurate orientation measurement (Maclaren et al., 2012). Communication with the tracking system was implemented directly on the real-time control unit of the scanner as previously described in (Zaitsev et al., 2006).

3.3.2.1. Phantom experiments

The data collection protocols are as follows:

1. ***Scan 1***: the homogeneous phantom was scanned at the constant pose with PMC enabled by using the low-resolution 3D Fast Low Angle Short (FLASH) with matrix: 208x208x208, voxel size: 3x3x3 mm, TR/TE: 6.00/2.55 ms, and readout bandwidth (BW): 750 Hz/pixel. This dataset was used to generate the coil sensitivity maps that correspond to the first half of k-space data in scan 2.
2. ***Scan 2***: The intra-volume motion with PMC enabled was performed by rotating the phantom approximately 5 degrees half-way through the scan. The acquisition parameters were 3D FLASH with voxel size: 1x1x1 mm, TR/TE, the matrix size, and BW were same as in the scan 1.
3. The scan 1 was repeated in order to provide the coil sensitivity maps that correspond to the second half of k-space data in scan 2.
4. The phantom was moved back to the initial pose.
5. Steps 2-4 were repeated. The amplitudes of intra-volume motion in the scan 2 were increased.

Note that there was restricted movement from outside the scanner when using a small head coil (24- or 32-channel), therefore, the larger 8-channel head coil (Rapid Biomedical, Rimpar, Germany) that allows greater motion was used in phantom experiments.

3.3.2.2. In Vivo applications

The previous phantom experiments were performed in order to quantify the impact of the relative motion of coil sensitivity at different amplitudes of motion. And the augmented SENSE was implemented to reconstruct the corrupted data under the condition that the coil sensitivity maps at any motion pose are given. However, it is impractical and time consuming to acquire the calibration data for updating the coil sensitivities before or after every adjustment of intra-scan motion. Instead, the calibration data acquired at the beginning was regridded. After regridding, this data was used to estimate the coil sensitivity corresponding to motion data.

The study was carried out with one healthy male volunteer after receiving informed consent according to the IRB-approved protocol. All data were acquired with PMC enabled using a 24-channel head coil (Nova Medical, Wilmington, MA, USA). The marker was securely attached to a mouth guard which was individually molded to the volunteer's upper teeth using medical grade hydroplastic (see Figure 3.5). The data collection protocols are as follows:

1. ***Scan 1***: The low resolution calibration data was acquired at the constant pose with PMC enabled. The imaging sequence and parameters were same as the scan 1 in phantom study.
2. ***Scan 2***: The intra-scan motion with PMC enabled was performed using 3D MPRAGE with matrix: 208x208x208, voxel size: 1x1x1 mm, TR/TE/TI; 1800/1.99/1050 ms, and BW; 750 Hz/pixel. The volunteer was instructed to perform head rotations during the scan.

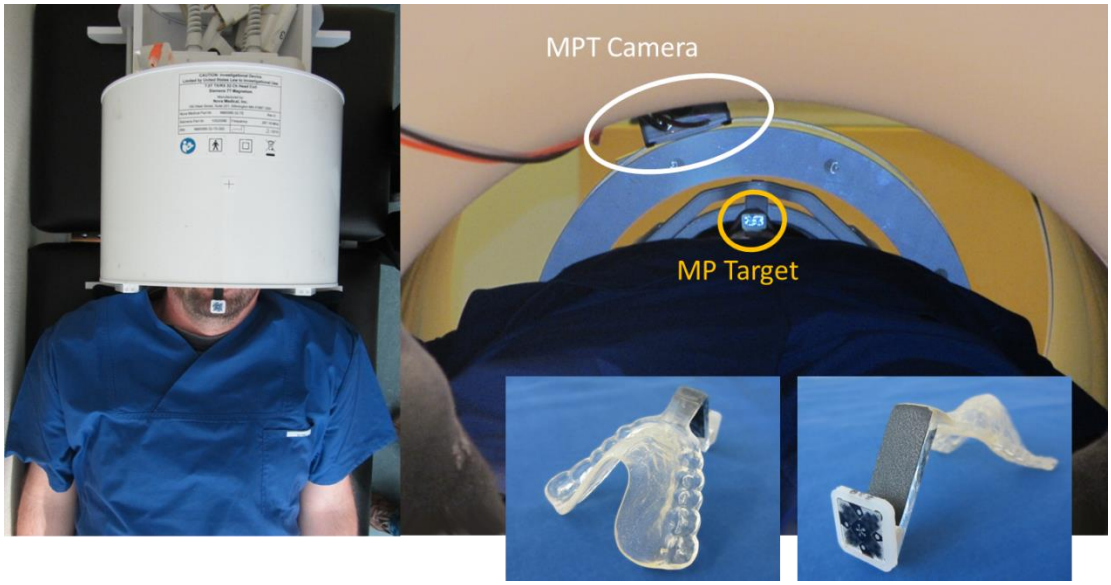

Figure 3.5. A volunteer with the mouth piece and tracking marker taken from approximately the same angle as where the moiré phase tracking (MPT) camera would be located in the scanner bore. (from BMMR, Magdeburg).

3.3.3. Data processing

The reconstruction was offline performed using MATLAB (version 12, The MathWorks Inc.), running on a Linux system. Before performing augmented SENSE reconstruction, both the k-pace line/group specific motion poses and the coil sensitivities at any motion pose need to be prepared as the following steps.

❖ **Position Binning**

Following the steps were described by Banerjee et al. (2013). The first step is to partition (segment) the acquired data into bins, in which all of the data within a bin have been collected while the object was considered to be in a single position. The number of bins is determined dynamically as the algorithm partitions the data. Position binning uses the position estimates already determined by the PMC system, which can be expressed by six parameters for each acquisition segment: three translation parameters (t_x, t_y, t_z), collectively denoted by $\vec{T}_j$, and three rotation parameters (r_x, r_y, r_z), collectively denoted by $\vec{R}_j$, where j indexes the acquisition segments. The relative motion between any two phase encoding lines (phases) $j1$ and $j2$ can be expressed by two scalar numbers representing the net translation and rotation between the two phase: $\Delta T = \left\|\vec{T}_{j1} - \vec{T}_{j2}\right\|$ and $\Delta R = \left\|\vec{R}_{j1} - \vec{R}_{j2}\right\|$, where $\|\cdot\|$ denotes the L2 norm. In this work, ΔT and ΔR are computed by comparing the j^{th} phase to all previously acquired data phases. If a preexisting bin is found in which ΔT and ΔR between all bin members and the j^{th} phase are below preset translation and rotation thresholds, the phase is added to that bin. If no matching bin is found, a new bin is created. Once the data assigned to bins is complete, the mean position parameters (translations and rotations) are computed as an average of N phase encoding lines associated with data allocated to that bin.

❖ **The coil sensitivity profile preparation**

The sensitivity maps obtained by the steps in Figure 3.1 may be insufficient for reconstructing the motion data since the fact that large motion can result in acquired data

outside the measured coil sensitivity maps. In addition, the low resolution calibration data inherently produce the ringing artifacts around the image edges. Therefore, the further processing steps were required. Firstly, the low-pass filter so-called cosine taper window was applied to minimize ringing artifacts. Then, filtered data were zero-filled to a size corresponding to the reconstructed images, i.e. in this case 208 x 208 x 208. Inverse Fourier transformation takes the data from k-space to image space. Each surface coil image was divided by their RSS to yield raw sensitivity map. Although the interpolation-extrapolation method such as polynomial fitting can be used to reduce noise from the maps and provide local extrapolation, the extrapolation area is very small, as shown in figure 3.1e. Here, we used the 2D thin-plate spline (TPS) function (Lui et al., 2007) for smoothing the coil sensitivity. Each 2D raw coil sensitivity map (in the slice direction) was multiplied by the binary mask obtained from the RSS image (see Figure 3.6b). A small set of support points was then randomly selected within the masked region and used to solve Eq. 22 in (Lui et al., 2007) (see Figure 3.6c). This set of control points consists of only 10% of the total points inside the masked region. As can be seen, the thin-plate spline function not only provides a good fitting to the support points within the object, but also provides a reasonable extrapolation beyond the boundary of the object (see Figure 3.6d).

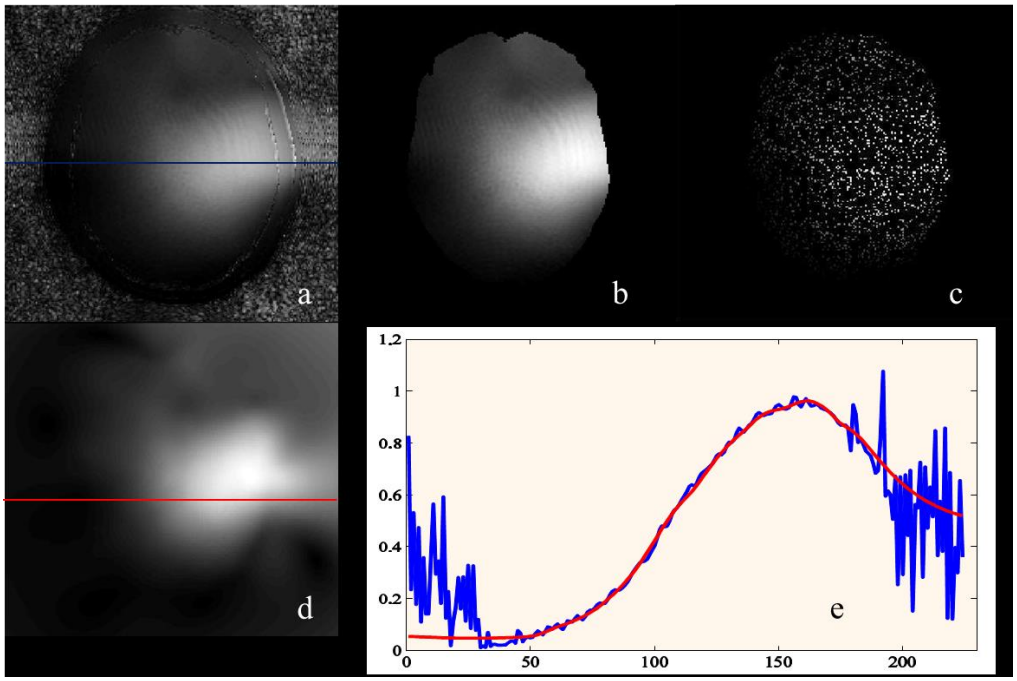

Figure 3.6. The estimation of coil sensitivity map using 2D thin-plate spline (TPS) fitting. (a) An example of a raw coil sensitivity map calculated by dividing the coil image with the RSS image. (b) The raw sensitivity map is masked to exclude the region outside the subject and regions of low signal intensity. (c) A small set of random control points are selected within the masked region. These control points are used to fit a 2D thin-plate spline function to the real and imaginary part of the sensitivity map independently. (d) The fitting of the sensitivity map. The fitted maps are smooth and provide both sensitivity interpolation and extrapolation. (e) A line profile of the sensitivity map through the center of the map. The blue curve indicates the raw sensitivity, while the red curve indicates the TPS fitted sensitivity.

Note that the calibration data corresponding to each motion bin can be prepared by regridding this single dataset using the mean position vector of that position bin. A diagram of the regridding operation is shown in Figure 3.8. The TPS-based coil sensitivity estimation described above was applied to each regridded data. Finally, all sensitivity maps were incorporated in augmented SENSE reconstruction.

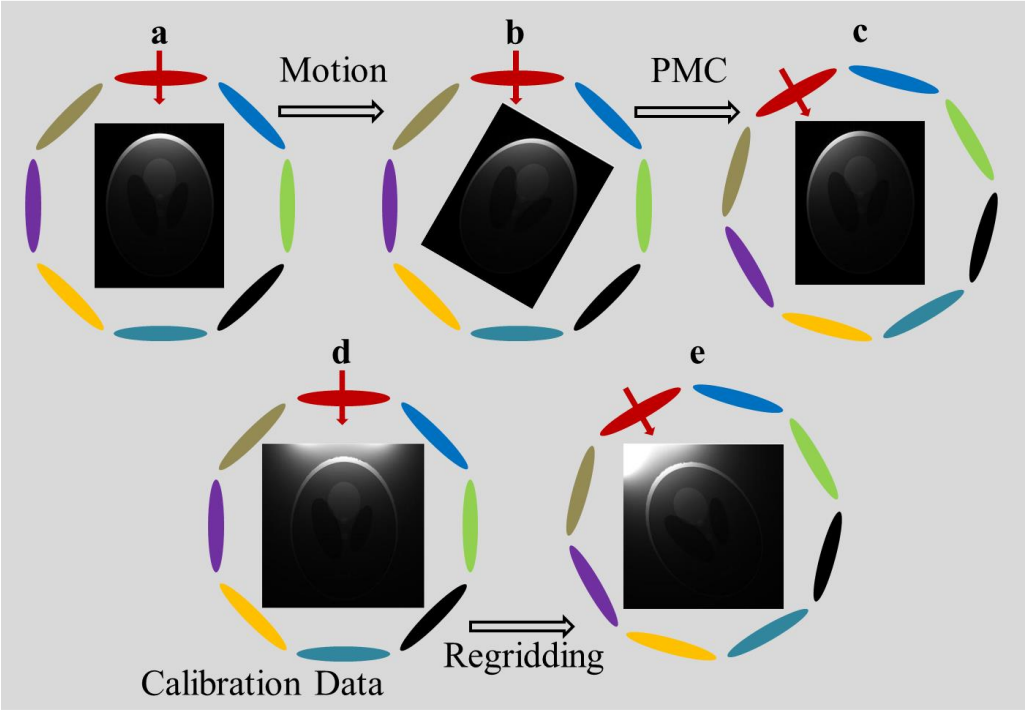

Figure 3.7. A diagram of the regridding operation for calibration data preparation. The top row shows the relative positions of the subject, imaging volume, and the stationary coils initially (a), after subject motion (b) and after prospective motion correction (c). The bottom row shows a scheme of the regridding operation for preparing calibration data suitable for the PMC data with position state (c). Please note that the initial position state is identical for the partial (a) and calibration data (d). After regridding, the relative position between the imaging volume and the stationary coils is identical for the partial PMC data (c) and the calibration data (e).

3.4. Results

3.4.1. Simulation Results

Figure 3.8 shows the signal change observed in the first set of simulations, which were designed to investigate the effects of shifting the phantom poses within the 8-channel head matrix receiver coil. The relative motion of coil sensitivity can degrade the quality of perfect PMC images. The degradations increased with larger motion and under-sampled data. Simulated artifacts are shown for examples of 0, 10, 15, and 20 degrees in-plane rotation under RSS and standard SENSE for fully sampled and 2x under-sampled data, respectively. Note that the sensitivity maps which are specific to the initial pose were used for standard SENSE. The artifactual signal change does not coincide with the anatomical features of the phantom, which are mostly deep within the phantom, but rather is prominent in regions where the coil sensitivity maps change most rapidly, near the phantom's surface (shown in the 2^{nd} and 4^{th} columns).

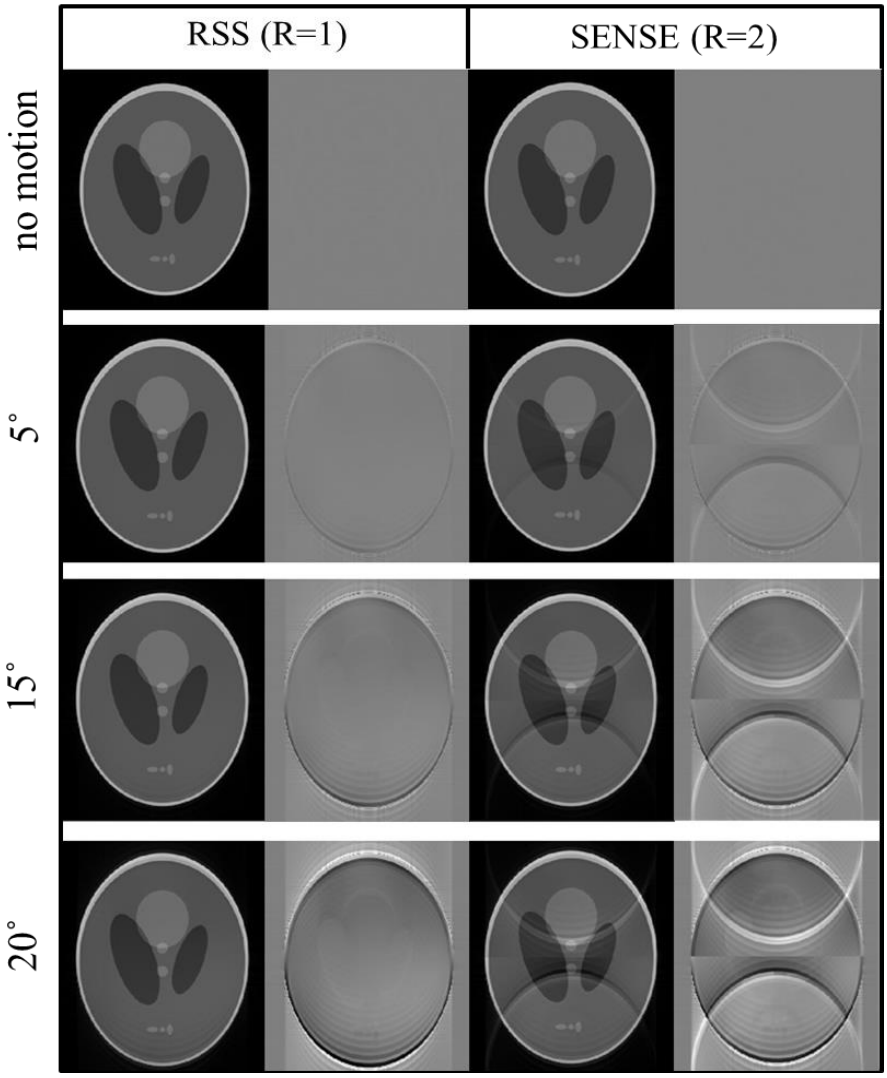

Figure 3.8. The identical windowed images for different rotation scales, reconstructed by RSS (1st column) and standard SENSE (3rd column), the artifacts increases with stronger motion in both fully sampled (R=1) and under-sampled (R=2) data. The image differences (2nd and 4th columns) between each reconstructed image and reference (no motion image) also increase with larger motion and higher reduction factor.

Conversely, Figure 3.9 shows that the augmented SENSE can significantly reduce the artifacts for all motion amplitudes as well as under-sampled data – the intensity of the corrupted images was recovered to almost the level of the reference after 20 iterations.

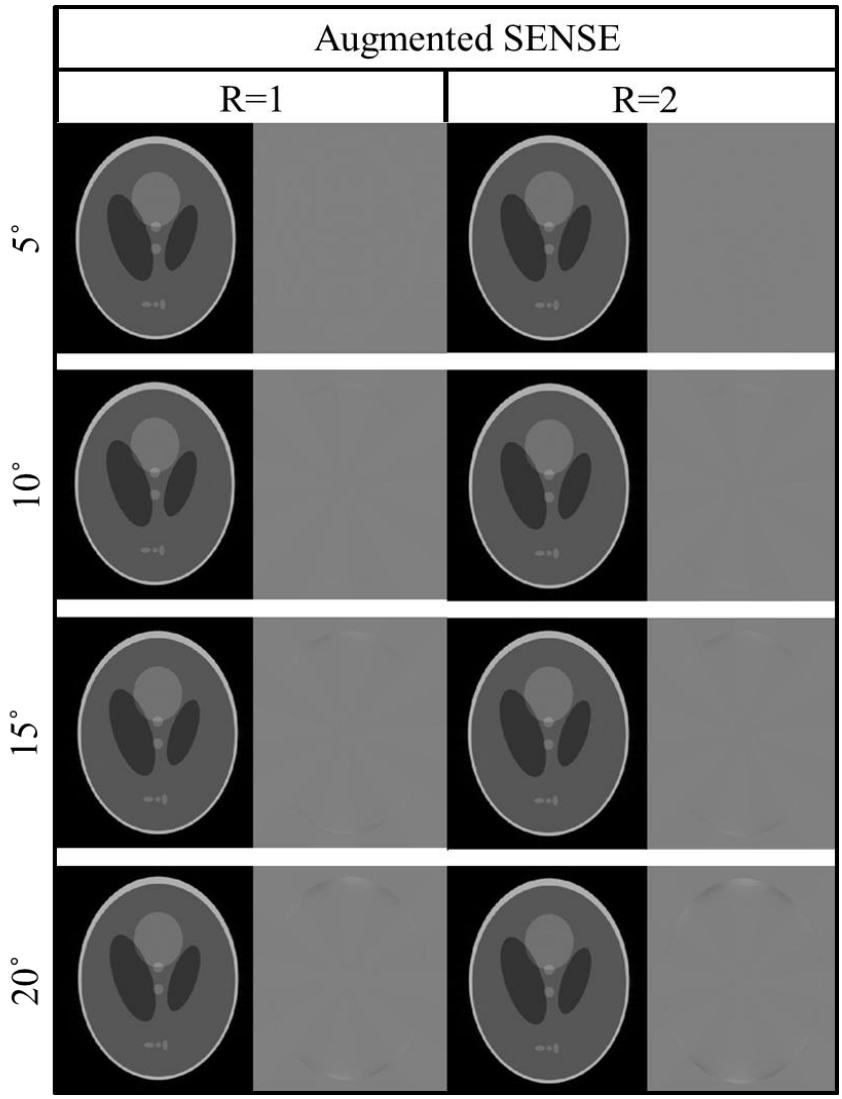

Figure 3.9. The identical windowed images for different rotation scales, reconstructed by augmented SENSE. The artifacts are notably reduced in all motion amplitudes, for both fully sampled (R=1) and under-sampled (R=2) data. The images in 2nd and 4th columns show the differences between each reconstructed image and reference (no motion image).

Figure 3.10 shows the RMSE values. For the standard reconstruction, the RMSEs of highly localized 12-channel receiver coil are slightly higher than 8-channel coil in both fully sampled and 2x under-sampled data. Moreover, they are increased as a function of motion amplitude. For augmented SENSE, the RMSEs of both coil type, both datasets and all motion amplitudes are very small, lower than 0.05.

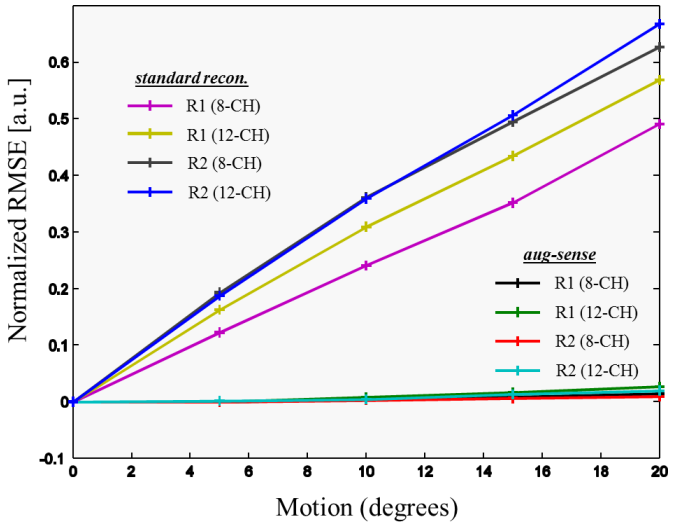

Figure 3.10. Normalized RMSE of simulations. Augmented SENSE provides smaller errors than standard reconstruction (RSS for R=1, and SENSE for R=2) in all motion amplitudes and all coil types.

3.4.2. Phantom Results

Figure 3.11 illustrates the signal change caused by the relative motion of coil sensitivity. For fully sampled data (R=1), the artifact appears somewhat small when ~5 and ~9 degrees of rotation were performed. The image became largely inhomogeneous when a large rotation (~25 degrees) was performed. For under-sampled data (R=2 and 3), only no motion images were likely to be acceptable. The rest were corrupted; the artifacts increased proportionally with the motion amplitudes.

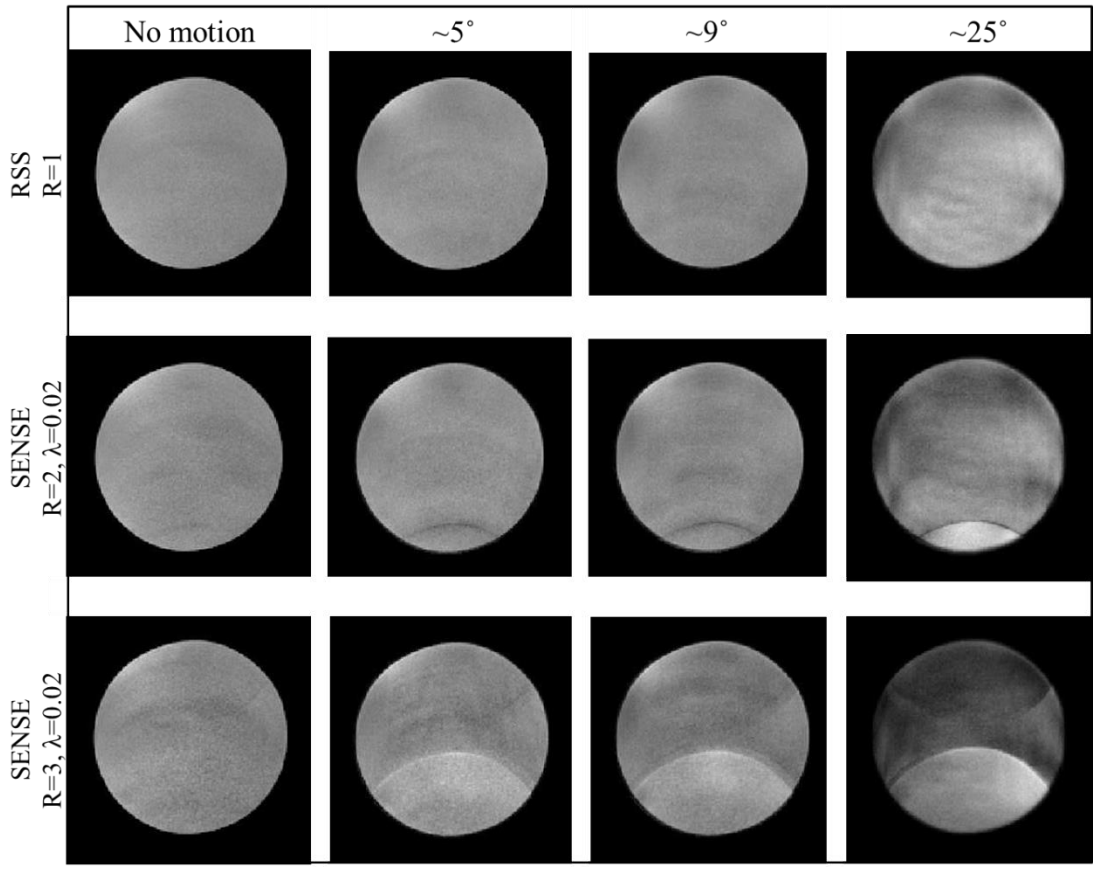

Figure 3.11. The identical windowed images reconstructed by RSS (R=1), and standard SENSE (R=2, 3). (1st column) no motion was performed during data acquisition. (2nd-4th columns) ~5, ~9, ~25 degrees of rotation around z-axis half-way through a scan were performed.

Figure 3.12 shows that the artifacts appear remarkably reduced after applying the augmented SENSE reconstruction. Although the homogeneity was much improved in large motion case, the residual artifacts were still higher than the small or no motion cases. Figure 3.13 shows the RMSE values obtained by the standard and the augmented SENSE reconstructions. In all experiments the augmented SENSE have always smaller RSME values. All the tests require only 20 CG iterations. The regularization parameters (λ), reported in the figures, are relative to the best reconstructions.

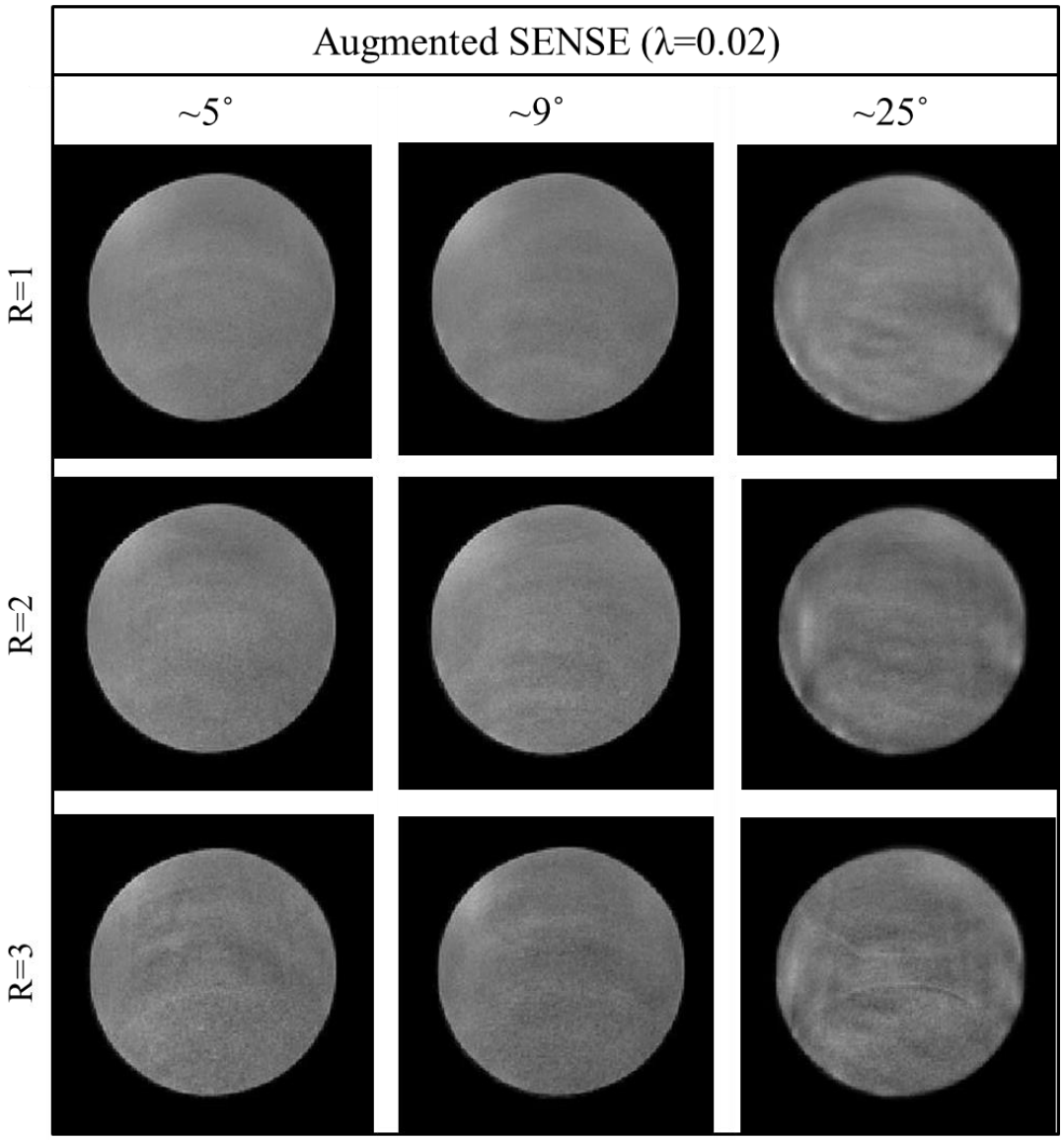

Figure 3.12. The identical windowed images reconstructed by augmented SENSE. (1st-3rd columns) ~5, ~9, ~25 degrees of rotation around z-axis half-way through a scan were performed.

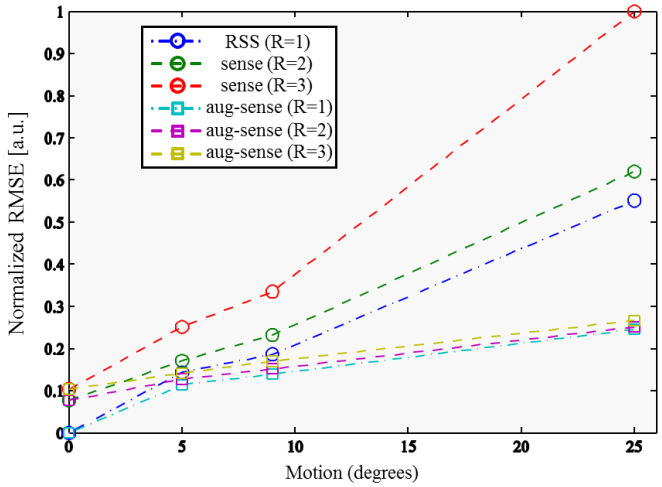

Figure 3.13. Normalized RMSE of homogeneous phantom experiments. Augmented SENSE provides smaller errors than standard reconstruction (root-sum-of-squares for R=1, and SENSE for R=2, 3) in all motion amplitudes.

3.4.3. In vivo Results

Figure 3.14a shows the motion pattern when the subject performed the head rotation during the data acquisition. A maximum rotation around the *z*-axis of approx. 12° was detected. Figure 3.14b illustrates the motion data with different acceleration factors (R=1, 2, and 3) reconstructed by the standard reconstruction (i.e., root-sum-of-squares for fully sampled data (R=1) and SENSE for under-sampled data (R=2, 3)). The quality of fully sampled and 2x under-sampled images appears likely to be comparable to the images obtained by the augmented SENSE (see Figure 3.15c). However, the residual folding artifact still remains high in the 3x under-sampled image obtained by the standard SENSE. In contrast, the abovementioned artifact was remarkably reduced in the images obtained by the augmented SENSE.

Figure 3.15 shows the artifact in the larger motion (approx. 26° rotation around z-axis and 22 mm. translation in x-axis). Although, the RSS provides an acceptable image for fully sampled data (R=1), the small details are missing as indicated in Figure 3.15b. For under-sampled data, the augmented SENSE shows much better improvement.

Note that the regularized parameters (λ) superimposed on all reconstructed images are the appropriate values which were selected manually.

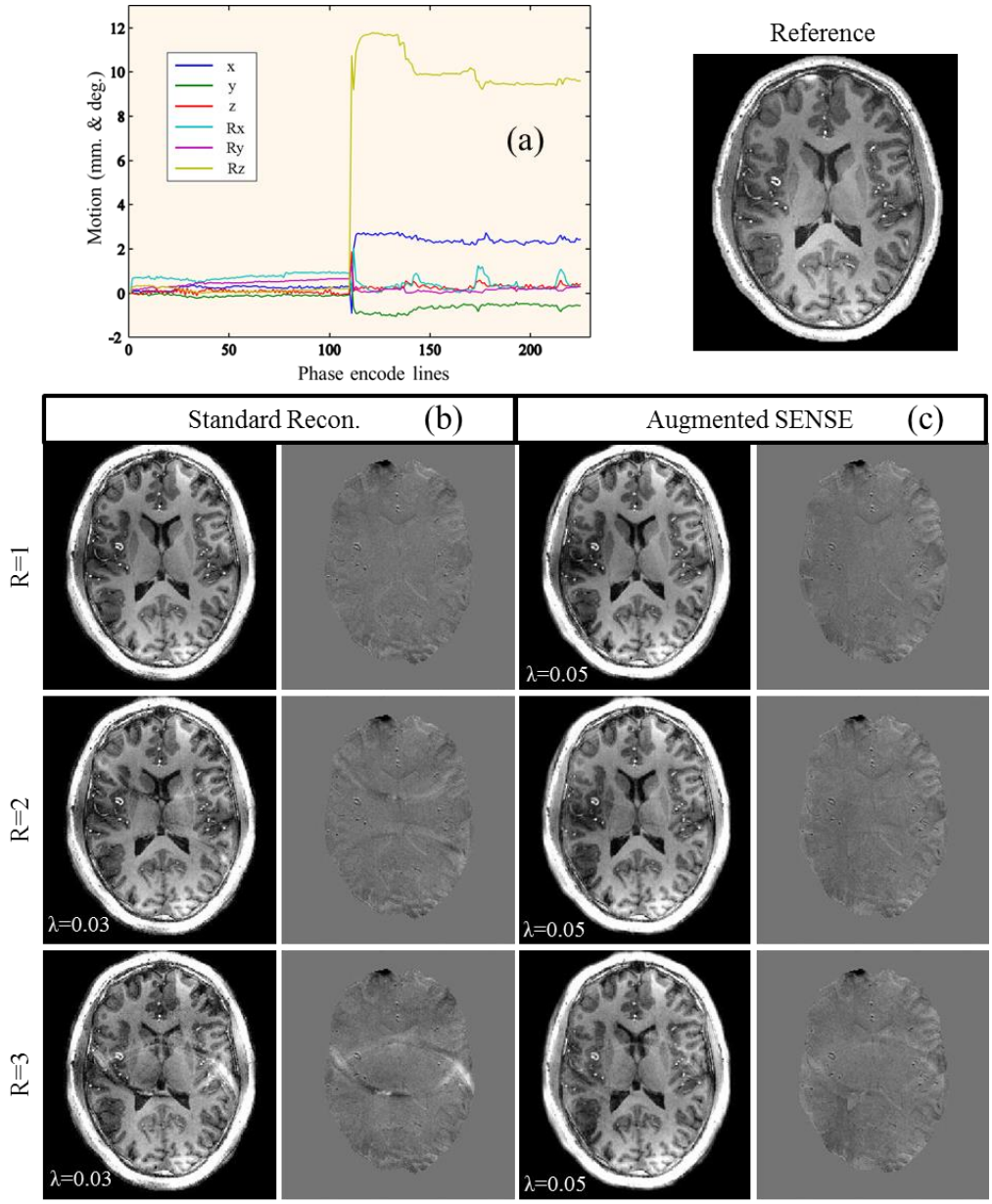

Figure 3.14. (a) The motion occurred during the acquisition of the corresponding images in b and c. (b) and (c) The identical windowed images for fully sampled and synthetic under-sampled data are reconstructed by standard techniques (1st columns) and augmented SENSE (3rd columns), respectively. The image differences (2nd and 4th columns) between each reconstructed image and reference (no motion image) are shown.

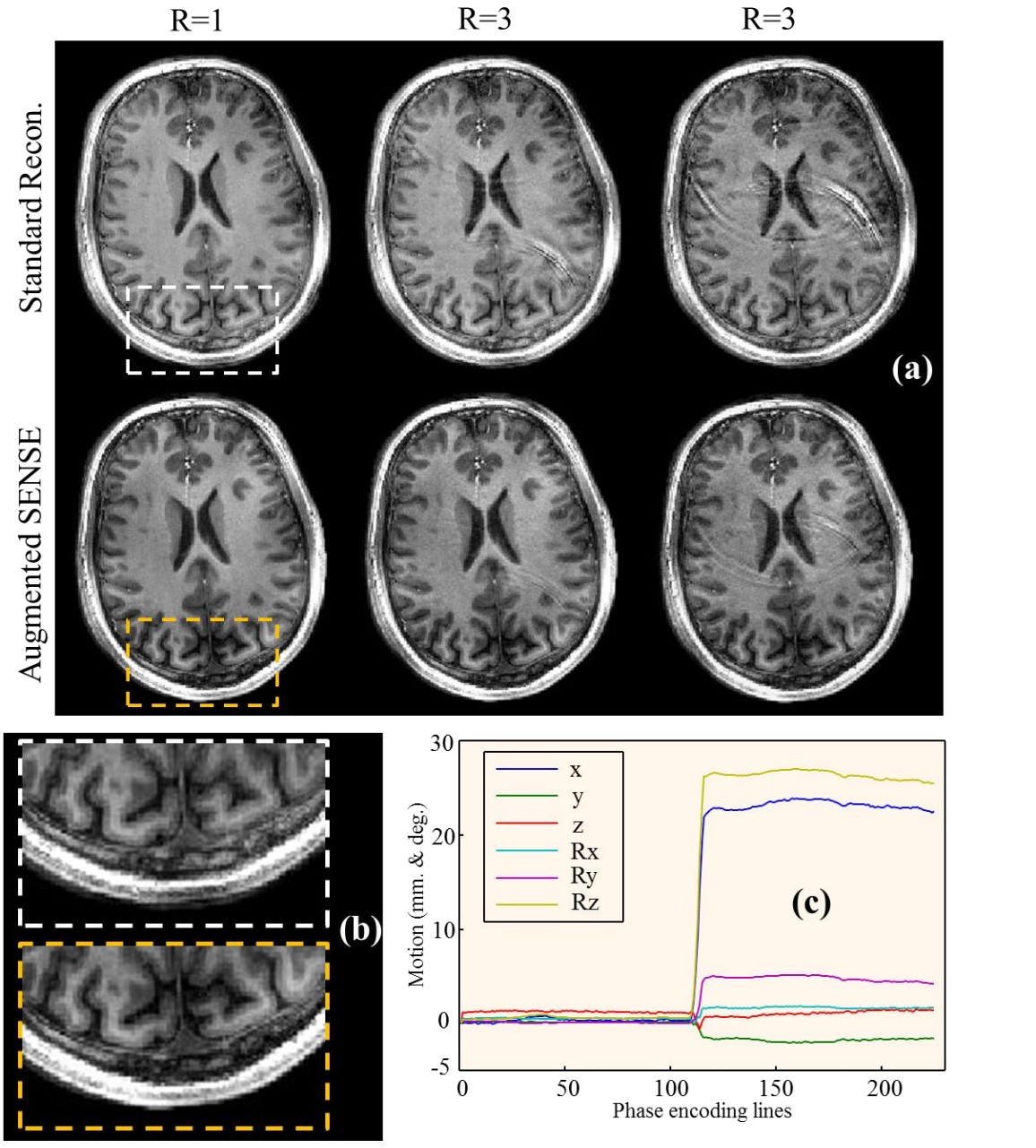

Figure 3.15. (a) The identical windowed images for fully sampled and synthetic under-sampled data reconstructed by standard techniques (1st row) and augmented SENSE (2nd row), respectively. **(b)** The enlarged images correspond to the same color boxes in **(a)**. **(c)** The motion pattern occurred during the acquisition of the corresponding images in **(a)**.

CHAPTER 4

4. CORRECTION OF GRADIENT NONLINEARITY INDUCED GEOMETRIC DISTORTION

The work presented in this chapter was accepted for publication:

Yarach U, Luengviriya C, Danishad A, Stucht D, Godenschweger F, Schulze P, Speck O (2015) Correction of gradient nonlinearity artifacts in prospective motion correction for 7T MRI. Magn Reson Med, 73(4), 1562-1569.

4.1. Preface

Standard *GNL* correction techniques, such as those widely available on commercial MR systems, are implicitly based on the assumption that an infinite set of continuous, noise-free k-space samples have been acquired (Glover et al., 1986). In this correction scheme, following inverse (continuous) Fourier transformation of the dataset, the nominal and actual images of the continuous physical object are related by a (continuous, conformal) coordinate mapping and intensity scaling based on the mapping's Jacobian determinant (Doran et al., 2005). Presuming that this mapping is both a priori known and bijective (i.e., invertible), the actual object image can be recovered from the distorted one simply by inverting these operations. In practice, however, only a finite set of discrete samples is acquired, and image domain interpolation is used to approximate the coordinate mapping operation (Doran et al., 2005; Glover et al., 1986; O'Donnell et al., 1985). Recently, a model-based MR image reconstruction method with integrated *GNL* correction was reported (Tao, Trzasko, Shu, HustonBernstein, 2015). As opposed to the conventional method where distortion is corrected after image reconstruction, this method prospectively accounts for the *GNL* effect during reconstruction and was shown to reduce the blurring and resolution loss caused by the conventional method, while still correcting the geometric distortion. For acquisitions with full k-space sampling, this method can be performed using type-1 of NUFFT. This advance method was mainly proposed for

mitigated *GNL* effect in static MRI. It may be also applicable for inter-scan motion MRI. However, its application for intra-scan motion MRI is not obvious.

Unlike in static or inter-scan motion MR applications, the *GNL* in inter-scan motion manifests as spatial distortion and blurring since object geometry at multiple object poses within the non-linear gradient fields and thus the k-space data become inconsistent between phase encoding steps. Recently, the correction of *GNL* for MR data acquired by using the continuous table motion technique, which is one kind of intra-scan motion, was introduced (Polzin et al., 2004). The fact that the subject and the receive coils move simultaneously in this acquisition scheme. As a consequence, there is no impact of the coil sensitivity misalignment. Only the impact of *GNL* was considered in their study. They applied a standard *GNL* correction (Glover et al., 1986) to the complex partial image and added it up to the previous corrected partial image via a non-iterative pathway, as shown in Figure 4.1. In practice, there are several challenges associated with the image-based interpolation required for the standard *GNL*'s correction. Due to the intrinsic smoothing effect of interpolation, there is often a noticeable loss in image quality, particularly in the presence of high spatial frequency components (Slavens, 2008; Tao et al., 2015; Thevenaz et al., 2000). Furthermore, image discretization can also be problematic, particularly when *GNL* causes the target object to shrink substantially and force a large amount of information into only a few pixels or even a single pixel.

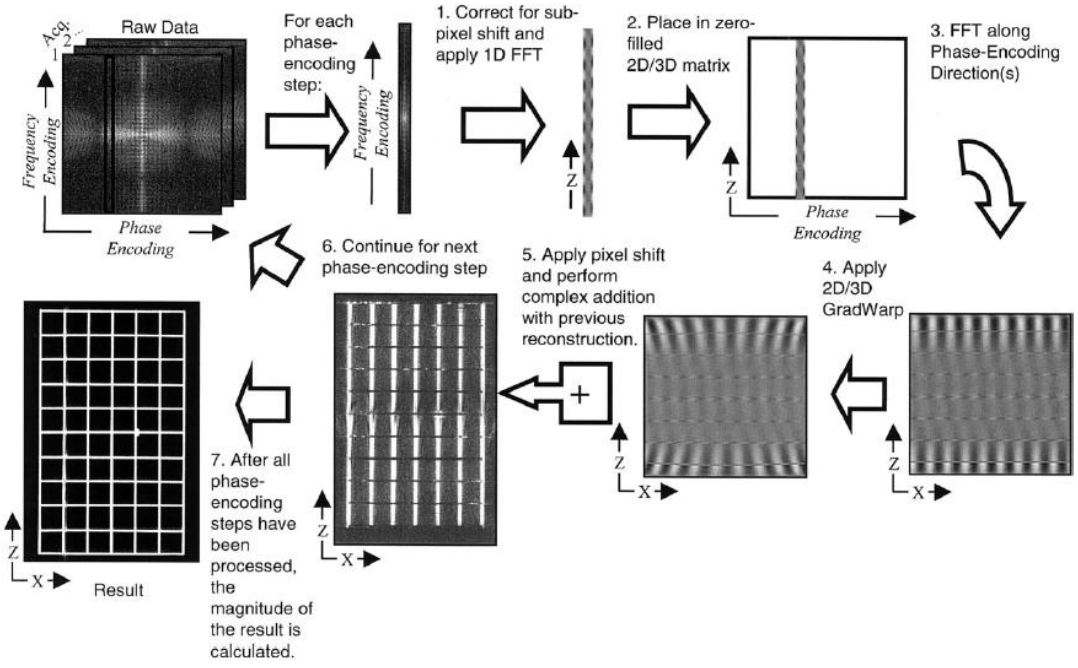

Figure 4.1. Processing steps for moving table reconstruction. Raw data shown for 2D (or 3D) coronal acquisition with frequency-encoding along physical Z, phase encoding along X (and Y). Each acquisition corresponds to entire set of *k*-space data acquired at a range of table positions. 1) Data from individual phase encoding is Fourier-transformed along the frequency-encoding direction. 2) The result is placed in a zero-filled matrix at a location corresponding to its position in *k*-space along the phase (and slice) encoding axis. 3) This 2D (or 3D) volume is then Fourier-transformed along the phase- (and slice-) encoding direction(s). 4) The resulting slice (or imaging volume) is then corrected for gradient nonlinearity. 5) The result is shifted by an integer amount corresponding to the table travel distance and added to the previously reconstructed data. 6) The procedure is repeated for each phase-encoding step and across all acquisitions. 7) After all phase-encoding steps have been processed, the magnitude is calculated. (from Polzin et al., 2004).

As shown in (Fessler 2010; Tao et al., 2015; 2015) and also in the chapter 3, the model-based reconstruction is a powerful framework for solving a variety of inverse problems in imaging. In this chapter, the encoding (forward) operator described in Eq. 3.1 was extended further by the spatial warping operator (i.e., the *GNL*'s effect). Since the data in spatial domains do not fall on uniform grid, the NUFFT-based iterative reconstruction was employed instead of the standard FFT. The effectiveness of the proposed iterative method with respect to the *GNL* artifact was evaluated through numerical simulations as well as phantom studies.

4.2. Theory

4.2.1. The Signal Model

More detail can be found in Tao et al. (2015). In practice only a finite number of k-space samples can be collected and will contain noise. As a result, the Fourier domain signal measured during a Cartesian MRI acquisition with non-ideal spatial encoding gradients can be modeled as:

$$s[\kappa] = \int_{FOV_x} \rho(x) \cdot e^{-j\omega[\kappa]\psi(x)} dx + n[\kappa] \quad (4.1)$$

Where $\psi(x)$ is the (presumed a priori known) distortion field caused by *GNL*; $s[\kappa]$ is κ-th signal measurement at k-space position $\omega[\kappa]$; and n is the zero-mean proper complex Gaussian noise.

The problem of reconstructing the continuous image function, $p(x)$, from a finite measurement vector, s, is intrinsically ill-posed without auxiliary assumptions about the target signal. Typically, a finite series representation of $p(x)$ is assumed (Fessler, 2010), that is, $p(x) \approx \sum_i u[i] b(x - r[i])$, where $b(x)$ is the (continuous) pixel basis function, $r[i]$ is the pixel position vector, and $u[i]$ is the corresponding display coefficient of the i-th pixel. Assuming a Dirac delta pixel model (i.e., $b(x) = \delta(x)$), the signal model in Eq. 4.1 gives:

$$s[\kappa] = \sum_i \int_{FOV_x} u[i]\delta(x - r[i])\, e^{-j\omega[\kappa]\cdot\psi(x)} dx + n[\kappa]$$

$$= \sum_i u[i]\, e^{-j\omega[\kappa]\cdot\psi(r[i])} + n[\kappa] \qquad (4.2)$$

Denoting the forward matrix operator $A[\kappa, i] = e^{-j\omega[\kappa]\cdot\psi(r[i])}$, the ensemble of measured data can be modeled in affine algebraic form as:

$$s = Au + n \qquad (4.3)$$

For fully sampled Cartesian imaging, the set of k-space samples lie on a discrete uniform grid. Although image pixels are also generally assumed to lie on a similar uniform grid ($r[i]$), the presence of a distortion field (i.e., when $\psi(r[i]) \neq r[i]$) causes these to be displaced in the discrete forward model according to $\psi(r[i])$. Therefore, the nominal spatial grid of an image reconstructed under Eq. 4.3 may actually be non-uniform. Thus, A essentially represents a non-uniform to uniform linear mapping for the Cartesian case. Note that without *GNL*, that is $\psi(r[i]) = r[i]$, the forward operator A reverts to the standard discrete Fourier transform (DFT) matrix. The forward operator, A in Eq. 4.3 can be efficiently implemented using the type-I non-uniform fast Fourier transformation (NUFFT) which is defined as follows:

$$A = (DF\Gamma)_\psi \qquad (4.4)$$

where Γ is a matrix representing convolution interpolation operation that maps the irregular image grid onto an oversampled uniform image grid, F is an oversampled DFT (implemented using FFT), and D is pixel-wise deapodization function (i.e., diagonal matrix) that compensates for blurring induced by a convolutional kernel, Γ.

❖ **The encoding operator of PMC for Cartesian sampled MRI**

We remind the readers that the motion corrupted MR signal received from multiple coil arrays was described in Eq. 2.49. After applying the highly accurate PMC, the

forward operator $\boldsymbol{E}^{p,q}$ that assumes linear magnetic field gradients across the sample is clearly shown in Eq. 3.1. When the *GNL* is also considered, the FFT in Eq. 3.1 can be replaced by operator $\boldsymbol{A}$ (Eq. 4.4). Thus, the forward operator with considered *GNL* specific to pose p and coil q can be defined as:

$$\boldsymbol{E}^{p,q} = \boldsymbol{M}^{p}\boldsymbol{A}^{\boldsymbol{p}}\boldsymbol{C}^{p,q} = \boldsymbol{M}^{p}(DF\Gamma)_{\boldsymbol{\psi}_{\_p}}\boldsymbol{C}^{p,q} \qquad (4.5)$$

❖ **The warped coordinate preparation**

Unlike the FFT, the NUFFT requires the explicit transformed coordinate which is called here the warped coordinate caused by *GNL*. In this study, the warped coordinates were prepared by applying the warping operator $\boldsymbol{\psi}_{\_p}$ to the uniform xyz grid points. More explicitly, the operator $\boldsymbol{\psi}_{\_p}$ consists of a set of rigid ($\boldsymbol{\Omega}^{p}_{PMC}$) as well as non-rigid ($\boldsymbol{D}_X, \boldsymbol{D}_Y,$ and $\boldsymbol{D}_Z$).

$$\begin{aligned}
&[x'_p, y'_p, z'_p]^T = \boldsymbol{\psi}_{_p}[x, y, z]^T \\
&[x_p, y_p, z_p]^T = \boldsymbol{\Omega}^{p}_{PMC}[x, y, z]^T \\
&x'_p = x + \boldsymbol{D}_X(x_p, y_p, z_p) \\
&y'_p = y + \boldsymbol{D}_Y(x_p, y_p, z_p) \\
&z'_p = z + \boldsymbol{D}_Z(x_p, y_p, z_p)
\end{aligned} \qquad (4.6)$$

where $\boldsymbol{D}_X, \boldsymbol{D}_Y, \boldsymbol{D}_Z$ are the gradient nonlinearities in each of the three directions. They are functions of the spatial coordinates at any pose p. Obtaining an accurate description of the gradient field distribution is not a simple task. The most general approach is to expand the field using spherical harmonics as the basis function (Janke et al., 2004a). The field generated by a gradient field ($V = X, Y, or\ Z$) can be written in spherical coordinates as follows, where $\boldsymbol{B}_{V(m,n)}(r, \theta, \varphi)$ is a spherical harmonics (SPH) expansion of order *n* and degree *m* of each component of the gradient field, and has the form

$$\boldsymbol{B}_{V(m,n)}(r,\theta,\varphi) = r^n\left[a_{V(n,m)}cos(m\varphi) + b_{V(n,m)}sin(m\varphi)\right] \times P_{(n,m)}(cos\theta) \quad (4.7)$$

$$\boldsymbol{D}_{(V=X,Y,or\ Z)} = \sum_n \sum_m \boldsymbol{B}_{V(m,n)}(r,\theta,\varphi) \quad (4.8)$$

In this equation, V stands, in turn, for Cartesian coordinates x, y, and z; and r, θ, and φ are spherical coordinates in an ideal coordinate system; $a_{V(n,m)}$ and $b_{V(n,m)}$ are constants: the so-called 'SPH coefficients'. The associated Legendre functions are $P_{(n,m)}(cos\theta)$.

4.2.2. The Image Reconstruction Algorithm

The desired reconstructed images according to the operator $\boldsymbol{E}$ in Eq.4.5 were obtained by using the L2-norm based regularization. The processing steps using the CG method are the same as described above, but the FFT and iFFT are replaced by the NUFFT and its adjoint (iNUFFT), respectively. A schematic diagram of the proposed algorithm is shown in Figure 4.2. The four steps described in chapter 3 are repeated until the maximum iteration number or the stopping criteria are reached.

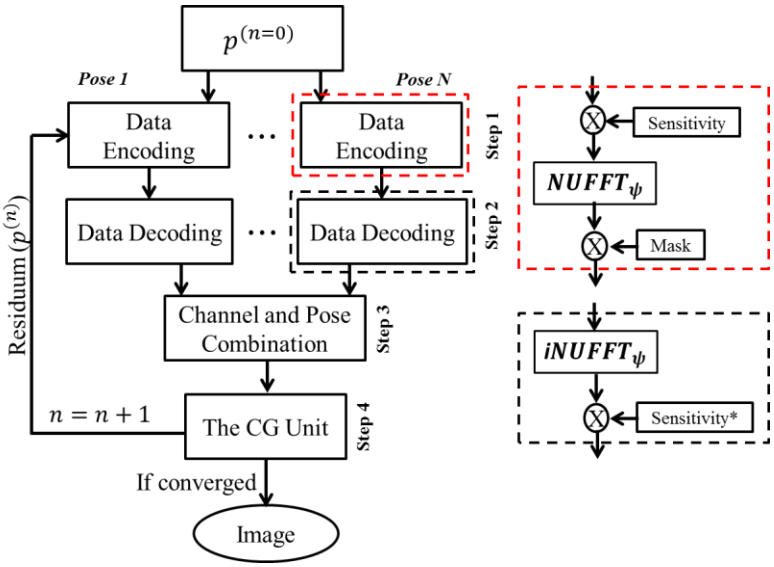

Figure 4.2. Schematic diagram of the augmented CG-SENSE with integrated *GNL* correction.

4.3. Materials and Methods

4.3.1. Numerical Simulations

The performance of the proposed reconstruction was first tested in numerical simulations using a Shepp-Logan phantom assuming a 2D axial image (FOV=256 mm^2, pixel size=1 mm^2). The ideal prospective motion correction was assumed. This means that the coil sensitivity profiles moved around the static phantom. The data encoding in Eq. 4.5 was applied to the static phantom in order to generate the motion-corrupted MR signal of each pose and channel. The 8-channel coil specific motion pose ($\boldsymbol{C}^{p,q}$) was simulated by using Biot–Savart's law as illustrated in chapter 3. The *GNL* field at the any pose was prepared by using spherical harmonics information specific for the gradient system of the 7T scanner. The 8-time intra-scan motion was assumed (every 32 k-space lines in a phase direction per pose). Note that to avoid the interference of the relative motion of coil sensitivity; the in-plane rotation was kept the same, only the translation in the z-direction was assumed to generate three corrupted datasets, including mild motion (0-10 mm), moderate motion (0-20), and large motion (0-30 mm). The motion patterns are shown in Figure 4.4. The identical information as used in artifact generation was applied in the image reconstruction

4.3.2. The MRI Phantom Experiments

All experiments were performed on an ultra-high field whole-body 7T MRI scanner (Siemens Healthcare, Erlangen, Germany) equipped with a 70mT/m whole body gradient system (SC72). PMC was applied to all scans. A 24-channel head coil (Nova Medical, Wilmington, MA, USA) was used. The acquisition parameters were 3D FLASH with matrix: 256x256x160; voxel size: 1x1x1 mm; TR/TE: 10/3.2 ms; and BW: 849 Hz/pixel. The structure phantom was scanned at four different constant poses to avoid any effects of internal motion in the object and potential inaccuracies, such as delays of the pose tracking. For the initial pose the phantom was placed at the center of the scanner (iso-center) then the table was moved -10, 10, and 20 mm away from the iso-center for the 2nd

– 4th poses, respectively. All poses were scanned with PMC enabled. Synthetic 3D data corrupted by residual artifacts after PMCs were created by combining the raw data of four poses, assuming mild, moderate, and large motions.

4.3.3. Data Processing

The reconstruction was performed using MATLAB (version 12, The MathWorks Inc.), running on a Linux system. Before performing the image reconstruction, the data binning and the coil sensitivities corresponding to motion pose were prepared as same as described in chapter 3. The *GNL* specific motion pose was analytically expanded as a linear combination of spherical harmonics (Eq. 4.7 and 4.8). Note that the higher-order SPH coefficients (n=3, 5, 7, and 9) were provided by the scanner manufacturer. Figure 2 shows the absolute error in cm for a 40 cm FOV within a Sonata (SC72) gradient coil set in whole-mode for each axis. It can be seen from the colour maps that there is very little error (less than 1cm) at the center portion of the FOV, but over 8cm of position error toward the FOV extremities. Furthermore, the forward and inverse of type-1 NUFFT operators using min-max interpolation on a denser grid (2x oversampling) were calculated using Fessler's NUFFT package (Fessler, 2014).

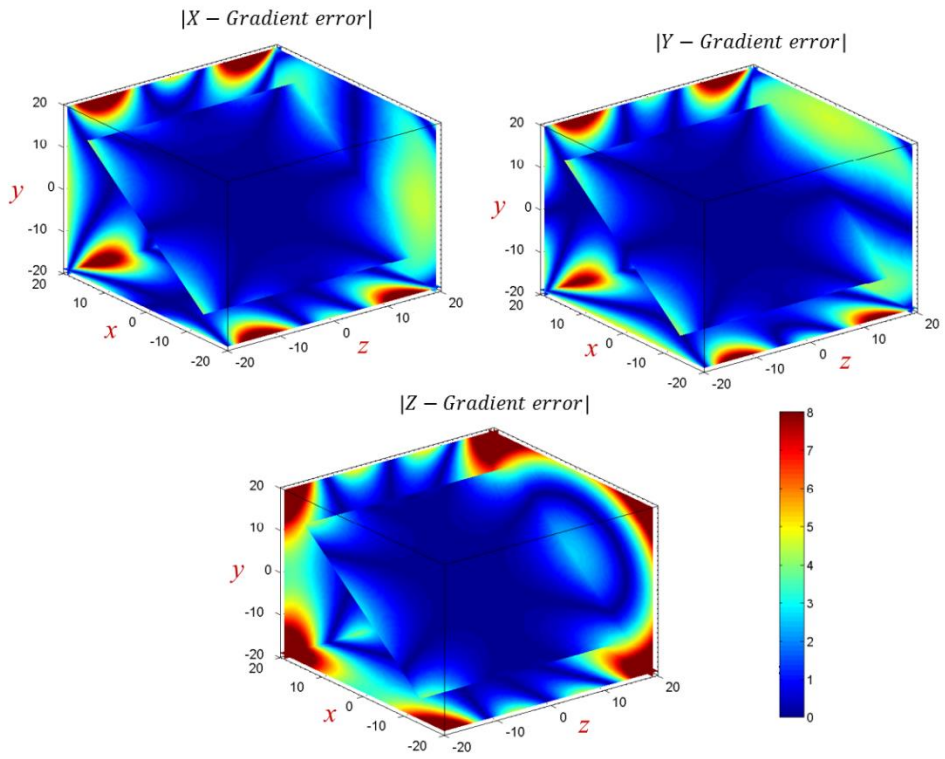

Figure 4.3. Gradient error as a function of position in centimeters within a 40cm field of view.

4.4. Results

4.4.1. Simulation Results

Figure 4.4 shows that the gradient nonlinearity can degrade the quality of perfect PMC images. The degradations increased with larger motion, i.e., the translations in the z direction were increased. Note that the shading artifact caused by coil sensitivity in all images appears small, visible, and identical due to corruption by the small and same patterns of in-plane rotation (R_z). Figure 4.5a shows that although the coil sensitivity artifact was already compensated for by the augmented SENSE, the residual artifact caused by *GNL* still remains and increases proportionally to the motion amplitudes. This remaining error was significantly reduced by the augmented SENSE with integrated *GNL* correction (see Figure 4.5b). Both shape and intensity of the corrupted images were recovered to almost the level of the reference after a few iterations. Figure 4.5c shows the

RMSE values for mild, moderate, and large motions. Without *GNL* correction, the RMSE values were 0.37, 0.41 and 0.55, respectively. With *GNL* correction, the values were largely reduced to 0.09, 0.09, and 0.11, respectively.

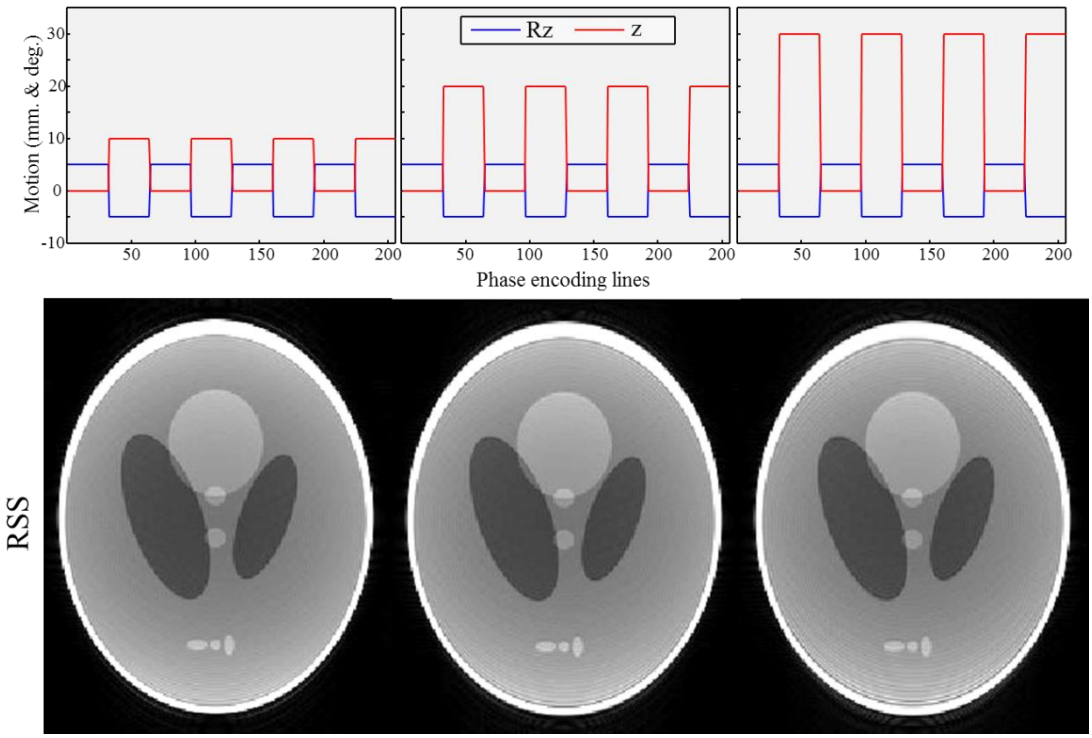

Figure 4.4. Identically windowed RSS images for three scales of motion. The artifact caused by *GNL* increases with stronger motion.

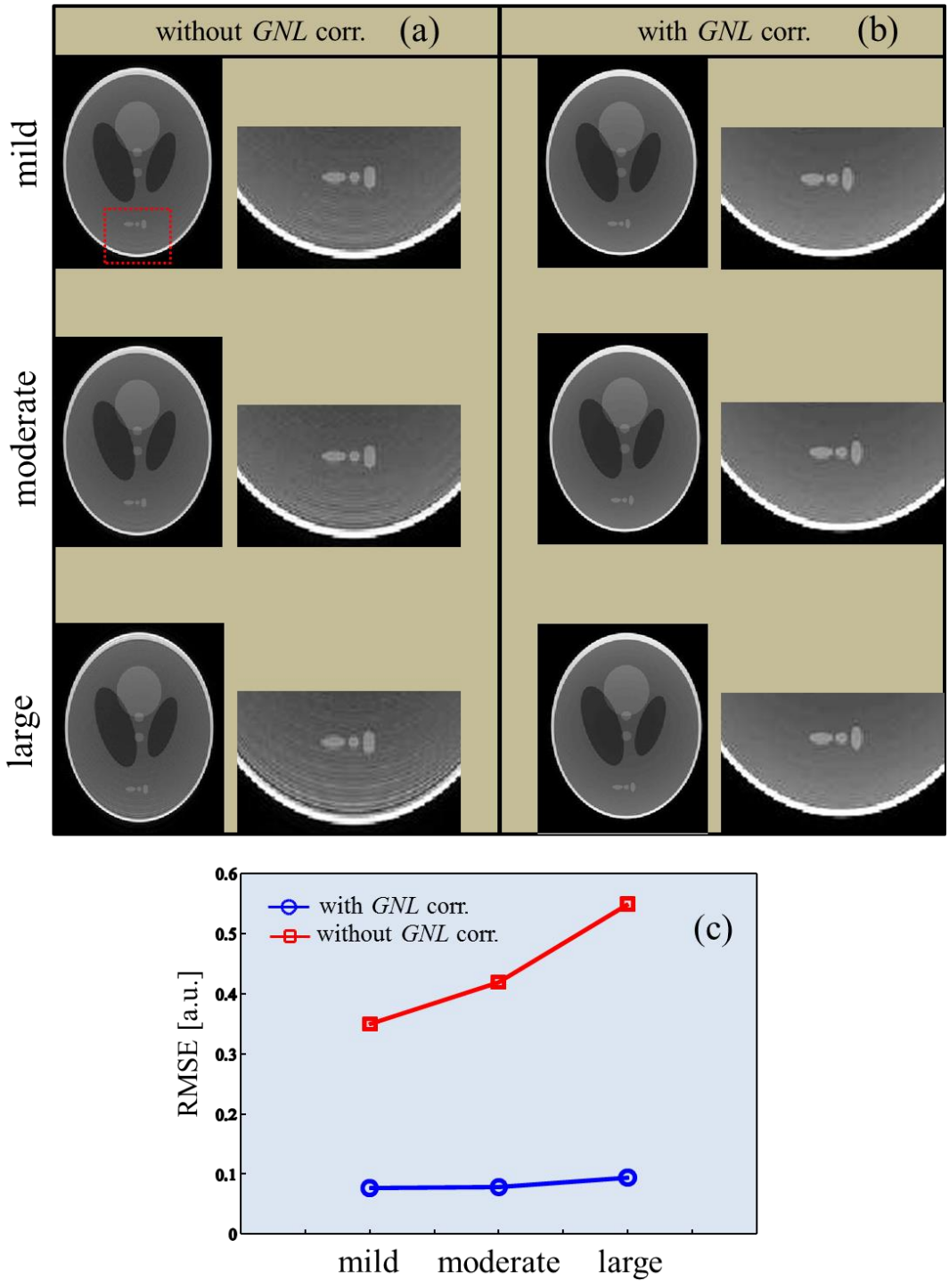

Figure 4.5. Three datasets at different scales of motion reconstructed by the augmented SENSE (a). Augmented SENSE with integrated *GNL* correction (b). The RMSE values obtained from both reconstructions (c).

4.4.2. MRI Phantom Results

Figure 4.6 can confirm that the changes of the B_0 field were relatively small; this is approx. 8 times smaller than displacements caused by gradient non-linearity when the phantom was moved ~25 mm in z-direction. This is due to the use of high sampling bandwidth (849 Hz/pixel). Moreover, the phantom is also somewhat homogeneous. Therefore, gradient imperfections are the dominant cause of residual artifacts after rigid body motion correction.

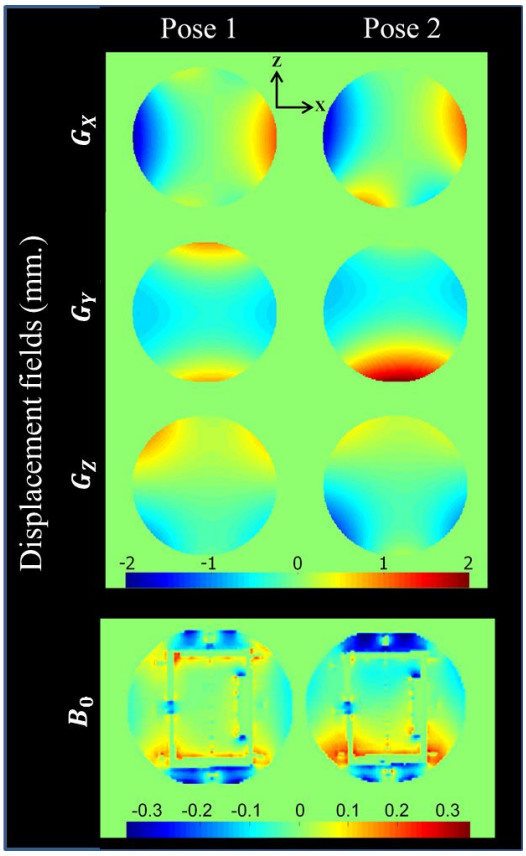

Figure 4.6. The change of displacements of the three gradients ($\boldsymbol{G_X}, \boldsymbol{G_Y}, \boldsymbol{G_Z}$) and the main magnetic field $\boldsymbol{B_0}$ corresponding to the chosen coronal slice at isocenter (Pose1) and -25 mm off-isocenter in the Z direction (Pose2). Note that the $\boldsymbol{B_0}$ induced shift is much smaller than the gradient distortion for the FLASH sequence used.

Figure 4.7 shows the images obtained by the standard Fourier reconstruction. The central slice closed to iso-center was less affected; when the object moving within the ranges of -10-0 and -10-10 mm. in the *z*-direction. The reconstructed images appear mostly to be free of artifact. However, in larger motion (-10-20 mm.), the blurring artifacts are slightly visible, particularly at the image edges (zoomed out region). For the peripheral slice (+55 mm. away from the iso-center), the standard reconstruction provided undesired images. The artifacts are highly visible even with mild motion and increase proportionally to the amplitude of motion.

Figure 4.8 shows high image quality. The blurring at the image edges of both central and peripheral slices became invisible when these images were obtained by the iterative augmented SENSE with integrated *GNL* correction via type-1 of NUFFT operator.

Figure 4.9 indicates that the RMSE values of the large motion data obtained from augmented SENSE without and with *GNL* corrections reduce from 0.085 to 0.049 (central slice), and 0.21 to 0.10 (peripheral slice), respectively.

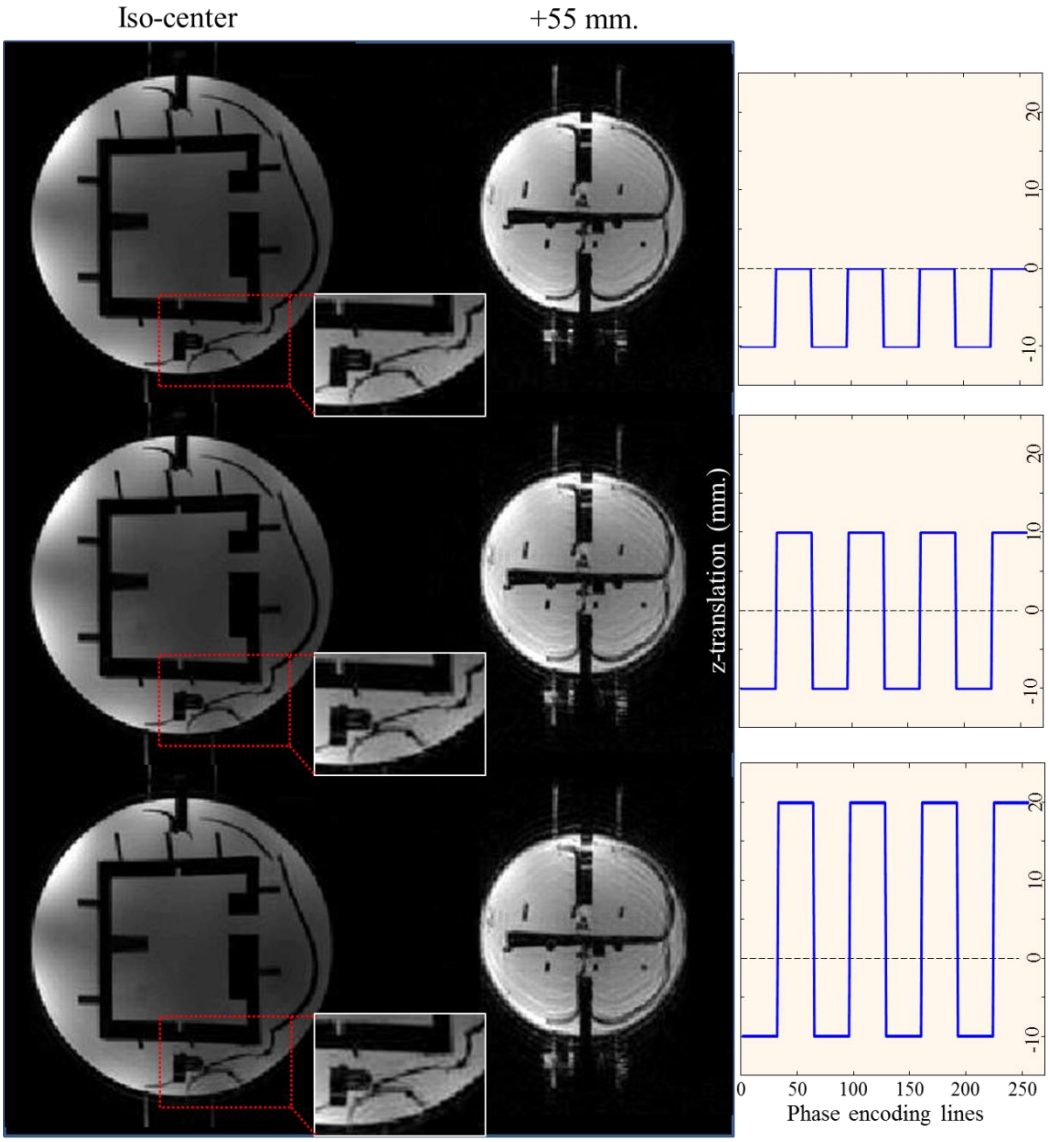

Figure 4.7. Three synthetic motion datasets including mild (-10-0 mm), moderate (-10-10 mm), and large (-10-20 mm) reconstructed by the standard Fourier transformation.

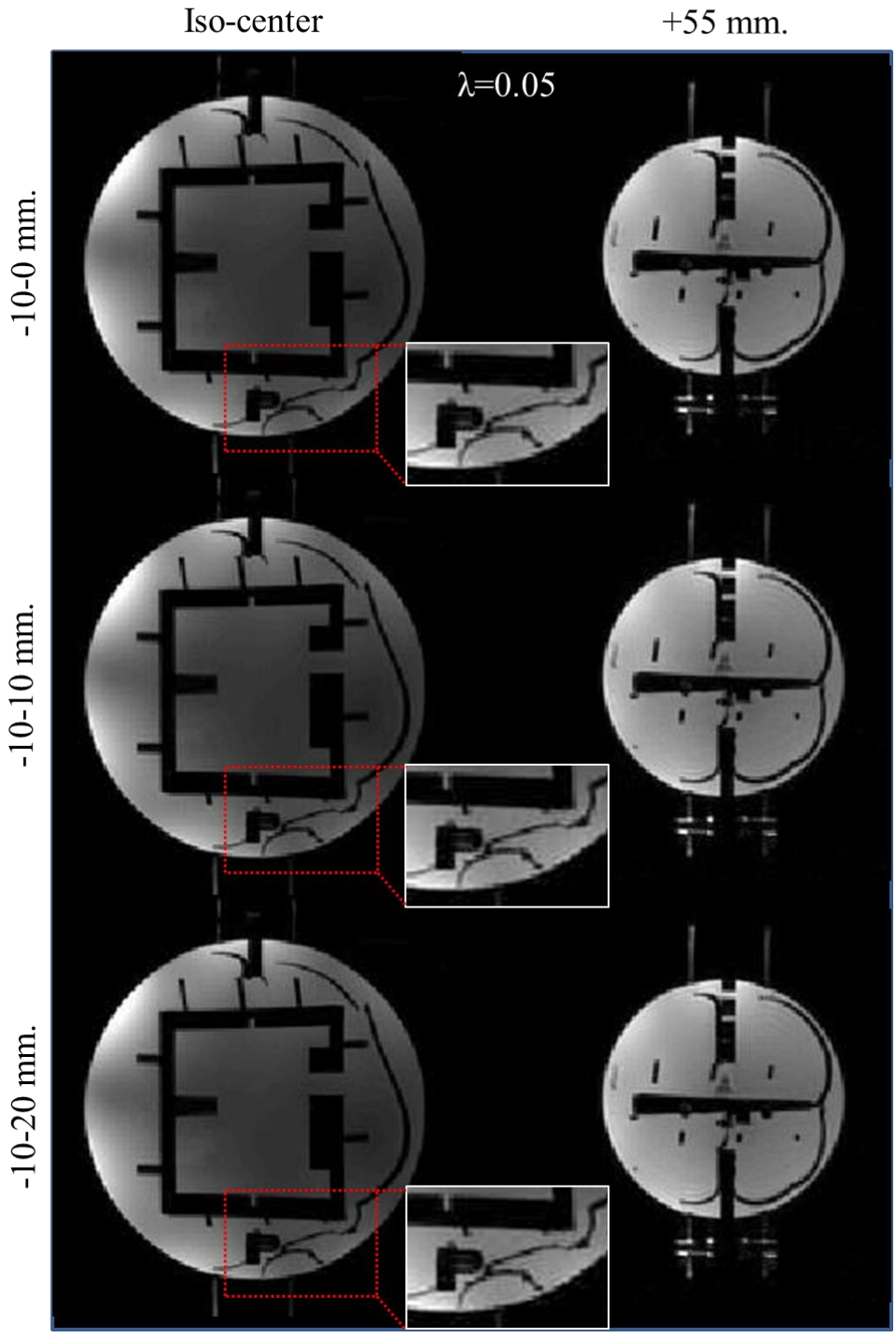

Figure 4.8. Three synthetic motion datasets including mild (-10-0 mm), moderate (-10-10 mm), and large (-10-20 mm) reconstructed by the augmented SENSE with integrated *GNL* correction.

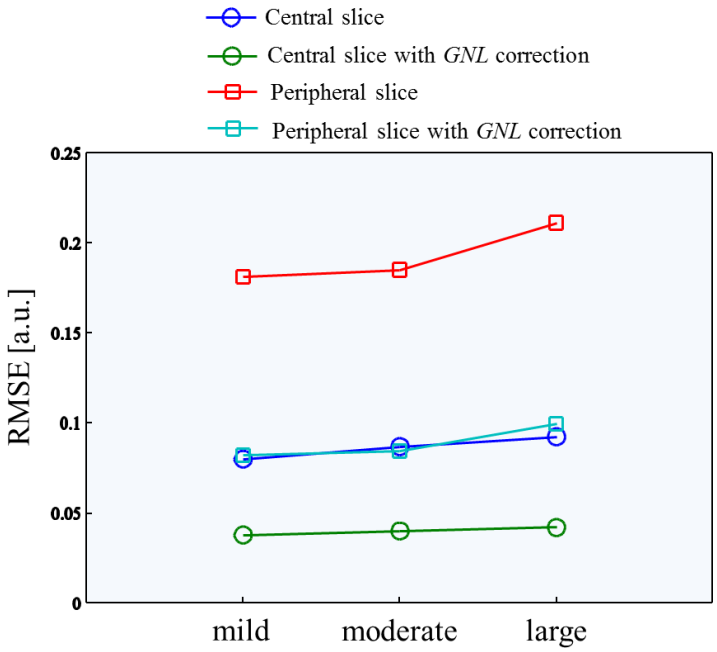

Figure 4.9. The RMSE values obtained from augmented SENSE without and with *GNL* correction.

It should be noted that when there is no interaction between the object's motions and receiving coils the images obtained by the RSS coil combination (for fully sampled data) are equivalent to the images shown in Figure 4.7, otherwise there is a shading artifact smear everywhere on the RSS images, as shown in Figure 4.10a. The shading artifact can be compensated if the coil sensitivities specific to motion pose are given and done via the augmented SENSE reconstruction (see Figure 4.10b). The central regions improve considerably while the residual blurring artifacts remain for both the edge of the center slice and more strongly at the periphery. This suggests that the artifacts cannot be compensated completely by this step alone. Again the shape errors in particular at the edge of the phantom only disappear when the gradient warp correction is integrated (see Figure 4.10c).

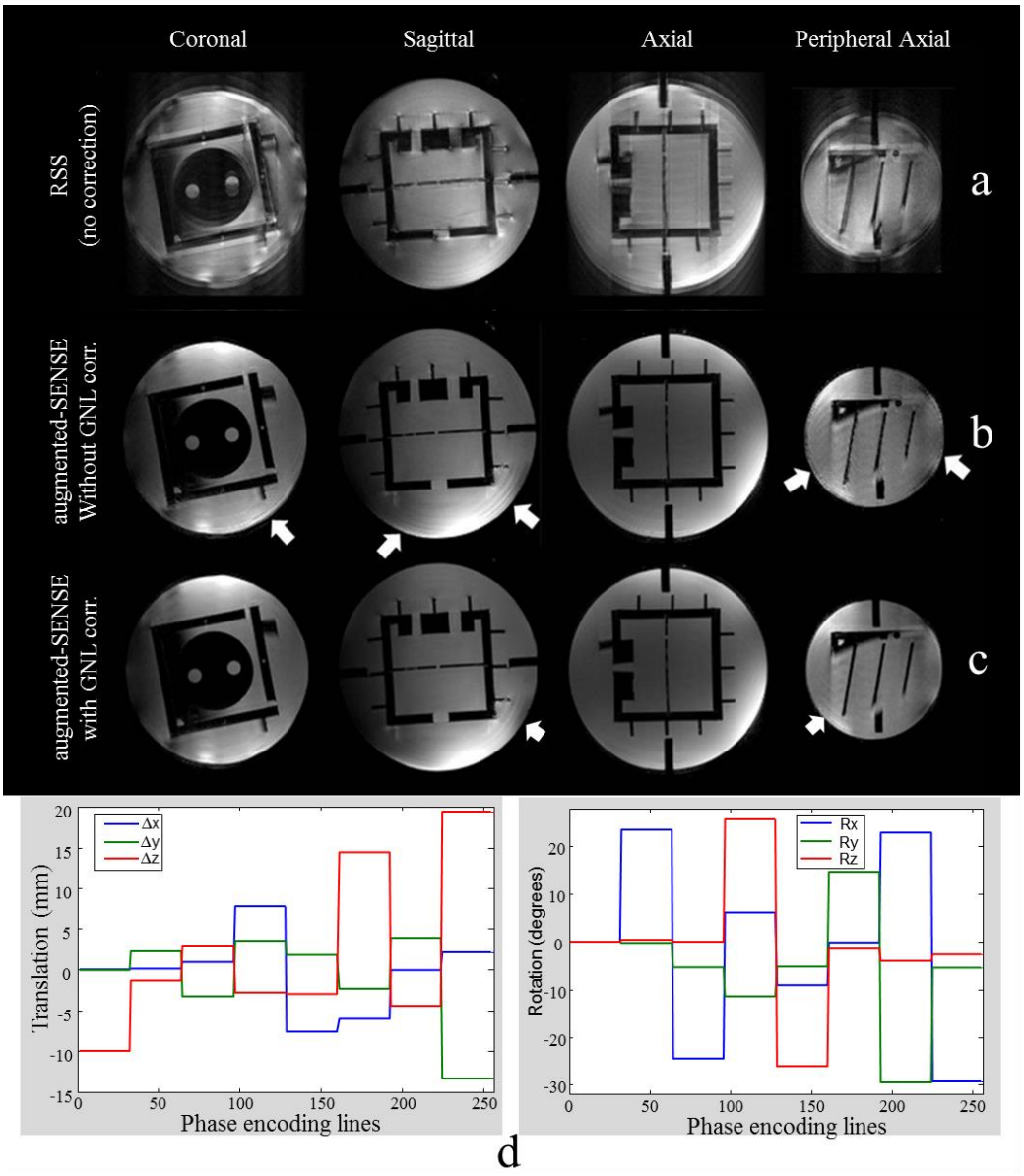

Figure 4.10. (**a**) Mixed k-space data from arbitrary poses lead to a strong artifact. (**b** and **c**) The 15th iteration of augmented SENSE images. (**b**) The intensity appear highly uniform after sensitivity maps correction, but blurring artifacts at the edge (white arrows) still remain after sensitivity map correction. (**c**) High image quality with very little remaining artifacts (white arrows) was achieved by the proposed method. (**d**) The patterns of mixing experimental phantom k-space from eight different poses (32 lines per pose).

CHAPTER 5

5. CORRECTION OF B_0 SUSCEPTIBILITY INDUCED GEOMETRIC DISTORTION

The work presented in this chapter was accepted for publication:

Yarach U, Luengviriya C, Stucht D, Godenschweger F, Schulze P, Speck O (2015). Correction of B_0-induced Geometric Distortion Variations in Prospective Motion Correction for 7T MRI. Magn Reson Mater Phy, 1-14 (Epub ahead of print).

5.1. Preface

In principle, not only *GNL* can result in spatial distortion due to motion but B_0 inhomogeneity caused by magnetic properties of the subject (e.g., air-tissue interfaces) is a relevant source of geometric distortions (Boegle et al., 2010; Jezzard at al., 1995; 1999; Ooi et al., 2013). Its effect is particularly, increased at a high field strength, such as 7T (Speck et al., 2008). Recently, the locations and sizes of B_0 field shifts within the brain at 7T for different head movements were reported (Sulikowska, 2014). These observations showed that the local field changes strongly depend on the subject orientation. As a consequence, the MRI applications with PMC at high field may be impacted by this variation even in conventional Cartesian MRI acquisitions (i.e., Spin-Echo and Gradient-Echo) with low readout-bandwidth (BW) that are often chosen to optimize signal-to-noise (SNR) or contrast-to-noise (CNR) ratios in structural imaging. The B_0 field shifts cause two effects: geometric distortions and signal dropouts. In this study, however, only the geometric distortion was investigated. A common approach for geometric distortion correction in a static or inter-scan motion MRI (e.g., EPI images) is based on physical analysis and the acquisition of dual echo gradient echo images, which provide an estimate of the magnetic field map through data acquisition at two different echo times (Jezzard et al., 1995). The geometric distortion correction using a field map is performed through voxel shift unwarping directly computed from the estimated phase field map value at

each voxel. This standard correction is often applied after the image reconstruction; the image post-processing.

The fact that k-space data acquired during intra-scan motion is inconsistent between the phase encoding steps since a subject experiences within the B_0 inhomogeneity which, changes relative to the subject orientations. A standard correction may be impractical since all corrupted k-space data are already combined during the reconstruction process.

In this study, we investigated B_0 field variations at different head orientations, and proposed a reconstruction scheme to mitigate ΔB_0-induced geometric distortion in the intra-scan motion MRI after PMC. The model-based reconstruction scheme described in chapter 4 was extended by the susceptibility-induced distortion correction. The effectiveness of the proposed iterative NUFFT method with respect to such residual artifacts was evaluated through numerical simulations as well as phantom studies. Finally the proposed method was applied to human brain MRI.

5.2. Theory

In this work, we considered the susceptibility-induced artifact as a spatial warping function. Thus, the MR signal influenced by this artifact can be modeled as shown in Eq. 4.5. However, as we mentioned in chapter 4, the NUFFT requires the transformed coordinates where affected by both *GNL* and B_0 field shifts. Therefore, the warping operator $\boldsymbol{\psi}_p$ shown in Eq. 4.6 needs to be extended by $\boldsymbol{D}_0$ which is the B_0-related displacement (pixel shift map).

$$
\begin{aligned}
&[x_p', y_p', z_p']^T = \boldsymbol{\psi}_{\_p}[x, y, z]^T \\
&[x_p, y_p, z_p]^T = \boldsymbol{\Omega}_{PMC}^{p}[x, y, z]^T \\
&x_p' = x + \boldsymbol{D}_X(x_p, y_p, z_p) + \boldsymbol{D}_0(x_p, y_p, z_p) \\
&y_p' = y + \boldsymbol{D}_Y(x_p, y_p, z_p) \\
&z_p' = z + \boldsymbol{D}_Z(x_p, y_p, z_p)
\end{aligned}
\qquad (5.1)
$$

Note that for non-EPI sequences, the bandwidth in the phase encoding direction is infinite. Therefore, B_0-related distortions need only be considered along the single frequency (read) encoding direction of the image. For example, if the read encoding gradient is aligned with the x axis, phase encoding is performed along the *y* and *z* axes for a 3D MRI (Eq. 5.1).

5.2.1. Measuring Field Map (B_0 Field Mapping)

The proposed reconstruction is required to convert the phase change map (field map) into a map of voxel shifts $\boldsymbol{D}_0(x, y, z)$ that can be used to unwarp the distorted images via the type-1 of NUFFT. Therefore, the effectiveness of proposed reconstruction relies on the accurate measurement of a field map. MRI-based B_0 field mapping (Jezzard et al., 1995; Weisskoff et al., 1992) is dependent on the complex detection of the MR signal, which gives angular phase ($\emptyset$) information on the transverse magnetization generated by the application of a RF excitation field at the Larmor frequency (ω_0) to the aligned nuclear spins. Following excitation, the magnetization phase at the echo time (TE) is given by

$$\emptyset = \emptyset_0 + \omega TE \quad (5.2)$$

where $\emptyset_0$ is the initial phase given by the RF excitation and ω is related to the local static field perturbation (in a rotating reference frame of $\omega_0$with no chemical shift) by

$$\omega = \gamma \Delta B_0 \qquad (5.3)$$

where ΔB_0 is the field perturbation and γ is the gyromagnetic ratio of hydrogen, and Eq. 5.2 becomes

$$\emptyset = \emptyset_0 + \gamma \Delta B_0 TE \quad (5.4)$$

Now consider two images acquired at two different echo times ($\Delta TE = TE_2 - TE_1$) with real and imaginary components related to their magnitudes and complex phase by Euler's formula: $IM_1 = R_1 + iI_1 = M_1 e^{i\emptyset_1}$ and $IM_2 = R_1 + iI_1 = M_2 e^{i\emptyset_2}$ with phases $\emptyset_1 = \emptyset_0 + \omega TE_1$ and $\emptyset_2 = \emptyset_0 + \omega TE_2$.

The phase difference of the two images is

$$\Delta\emptyset = \emptyset_2 - \emptyset_1 = \omega(TE_2 - TE_1) = \gamma \Delta B_0 \Delta TE \quad (5.5)$$

Noting that

$$IM_1^* \cdot IM_2 = M_1 M_2 e^{i(\emptyset_2 - \emptyset_1)} = R_1 R_2 + I_1 I_2 + i(R_1 I_2 - I_1 R_2) \quad (5.6)$$

where IM_1^* is the complex conjugate of IM_1 and the phase difference is also equal to

$$\Delta\emptyset = \emptyset_2 - \emptyset_1 = \arg(IM_1^* \cdot IM_2) \quad (5.7)$$

Then the magnetic field variation is easily computed by

$$\Delta B_0 = \frac{\Delta\emptyset}{\gamma \Delta TE} \quad (5.8)$$

Where the phase differences which is now also given by

$$\Delta\emptyset = tan^{-1}\left(\frac{R_1 I_2 - I_1 R_2}{R_1 R_2 + I_1 I_2}\right) \quad (5.9)$$

Phase differences which are greater than $\mp\pi$ must be unwrapped due to the periodic nature of the tangent function. Figure 5.1 shows an example of wrapped and unwrapped phase differences. Existing phase unwrapping algorithms fall into either spatial or temporal categories. An example of the spatial technique is the Phase Region Expanding

Labeler for Unwrapping Discrete Estimates (PRELUDE), which optimizes a cost function that identifies neighborhoods of unwrapped phases and iteratively merges the regions until a single unwrapped region remains (Jenkinson, 2003). The temporal approach typically acquires several sets of images with increasingly longer TE. The initial phase difference with minimum TE is assumed to be unwrapped (by choosing a small ΔTE), and successive phase differences with increasing ΔTE can have values of $\mp 2\pi$ added until it falls within the unwrapped regime. As each new phase difference is computed, the trend can provide a better estimate of the slope and improve the field map with each additional image set (Kock et al., 2009).

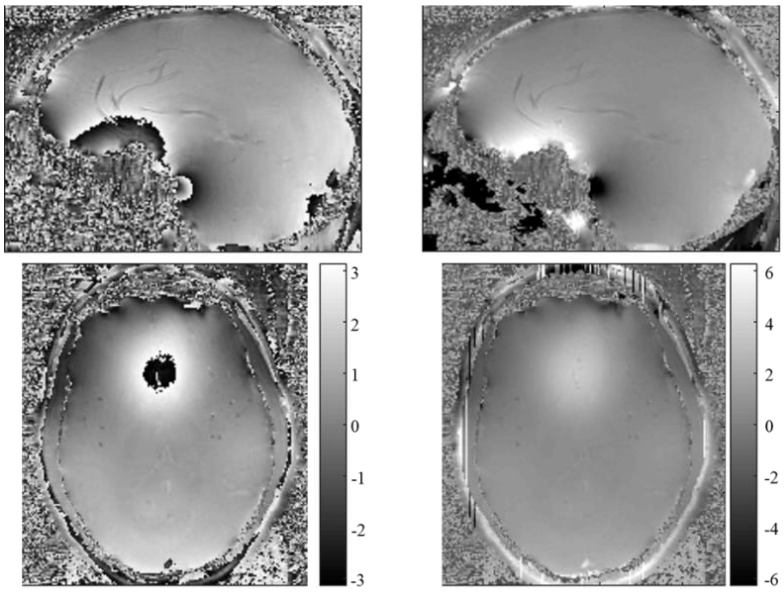

Figure 5.1. *1st column*: the phase difference images with the remaining wrapped phase. *2nd column*: the phase difference images after phase unwrapping. The given scales are in a unit of radians.

Furthermore, the B_0 field map can be converted into a pixel shift in the read encoding direction according to the following equation,

$$\boldsymbol{D}_0(x,y,z) = \frac{\gamma \cdot \Delta B_0}{BW_{read}} = \frac{\Delta \emptyset}{\Delta TE \cdot BW_{read}} \qquad (5.10)$$

where BW_{read} is the readout bandwidth (Hz per pixel).

5.2.2. Image Reconstruction Algorithm

The processing steps of the reconstruction are the same as described in chapter 3, but the FFT and iFFT are replaced by the type-1 NUFFT and its adjoint (iNUFFT), respectively.

5.3. Materials and Methods

5.3.1. Simulations

The performance of the proposed reconstruction was first tested in numerical simulations using a Shepp-Logan phantom assuming a 2D axial image (FOV=256 mm^2, pixel size=1 mm^2). The intensity values in a circular region with diameter 32 mm within the upper circular part of this phantom were replaced by zeros to represent an air inclusion (see Figure 5.4a). The ideal prospective motion correction was assumed. The data encoding in Eq. 4.5 with respect to both *GNL* and B_0-related distortions was applied to the static phantom in order to generate the motion-corrupted MR signal of each pose and channel. The 8-channel coil specific motion pose ($\boldsymbol{C}^{p,q}$) was simulated by using Biot–Savart's law as illustrated in chapter 3. The *GNL* at the any pose was expanded using spherical harmonics information specific for the gradient system of the 7T scanner used in the experimental studies (described in chapter 4). The object-specific field maps (in Hz) at air/water interfaces were analytically calculated by plugging the coordinate $x_p y_p z_p$ which is specific to any pose p ($[x_p, y_p, z_p]^T = \boldsymbol{\Omega}^p_{PMC}[x, y, z]^T$) into Eq. 5.11.

$$\begin{aligned} B_{inhomo\_ex}(x_p y_p z_p) &\approx B_0 \left\{1 + \frac{\chi_{air}}{3} + \frac{r^3(\chi_{air}-\chi_{water})(x_p^2+y_p^2-2z_p^2)}{3(x_p^2+y_p^2+z_p^2)^{5/2}}\right\} \\ B_{inhomo\_in}(x_p y_p z_p) &\approx B_0 \left\{1 + \frac{\chi_{air}}{3}\right\} \\ \Delta B_0 &\approx \gamma\{B_{inhomo} - B_0\} \end{aligned} \tag{5.11}$$

where γ, B_0, B_{inhomo_ex}, and B_{inhomo_in} are the gyromagnetic ratio of hydrogen, main magnetic field (7 Tesla), the magnetic fields outside, and inside the sphere of water of

radius r (16 mm), respectively. The χ_{air} and χ_{water} are the air and water susceptibility with values of -0.72x10^{-6} and -9.77x10^{-6}, respectively. This field map was divided by a readout-bandwidth (assumed 200 Hz/pixel in the x-direction), obtaining the displacement $\boldsymbol{D}_0(x_p y_p z_p)$ in a unit of pixels. These voxel shift maps were applied to warp the object images in the read encoding direction using type-1 of NUFFT. Note that the transformation matrix $\boldsymbol{\Omega}_{PMC}^{p}$, created by using the motion information shown in Figure 5.2b. The examples of the displacement gradients and field maps at any pose are illustrated in Figure 5.2a. Identical information as used in artifact generation was applied in the correction processes.

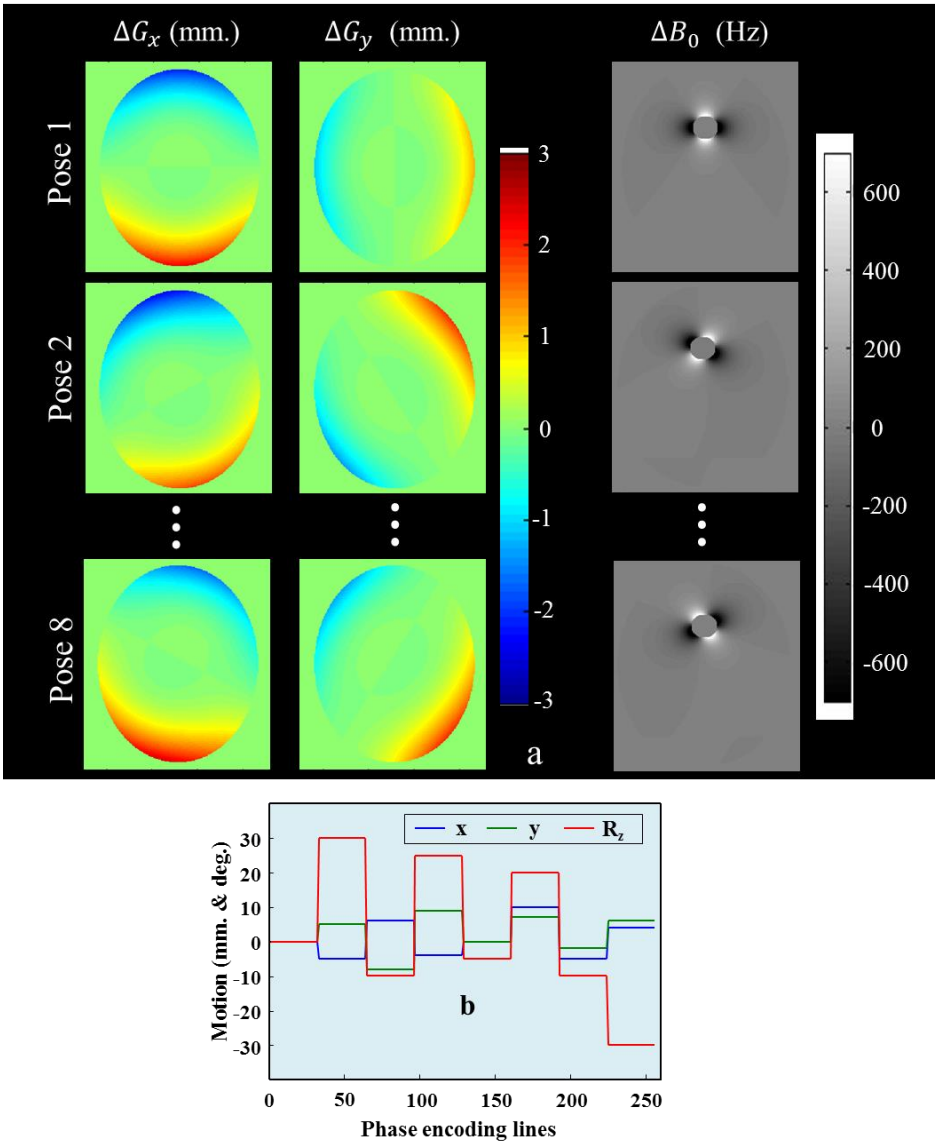

Figure 5.2. The simulated magnetic field displacements and the motion patterns: (a) The gradient displacements ($\Delta G_x, \Delta G_y$) and field maps (ΔB_0) corresponding to pose 1, 2, and 8. (b) The 2D rigid motion patterns of eight motion poses (32 phases/pose).

5.3.2. MRI Experiments

All experiments were performed on an ultra-high field whole-body 7T MRI scanner (Siemens Healthcare, Erlangen, Germany) equipped with a 70mT/m whole body gradient system (SC72). The PMC was applied to all scans.

5.3.2.1. Phantom experiments

An 18 cm diameter homemade phantom with a central air inclusion (ping pong ball) and further small structures was built (see Figure 5.3). This phantom was filled with silicone oil, whose dielectric properties resulted in minor RF-excitation inhomogeneity only (Wey et al., 2006). The phantom was scanned at two different constant poses with PMC enabled. In the second pose, the phantom was rotated ~33 degrees around the y-axis. An 8-channel head coil (Rapid Biomedical, Rimpar, Germany) was used. Each constant pose was scanned at two different echo times (TE). Both TE's data were used to estimate the B_0 field map (ΔB_0) for each pose. The acquisition parameters were 3D FLASH with matrix: 192x192x144, voxel size: 1x1x1.3 mm, TR/TE1/TE2: 6.00/2.55/3.06 ms, and BW=250 Hz/pixel. The synthetic corrupted data were created by combining the raw data of the two poses, assuming 2, 3, 4, 6, and 12 motions (i.e., 96, 64, 48, 32, and 16 k-space lines along phase direction per pose).

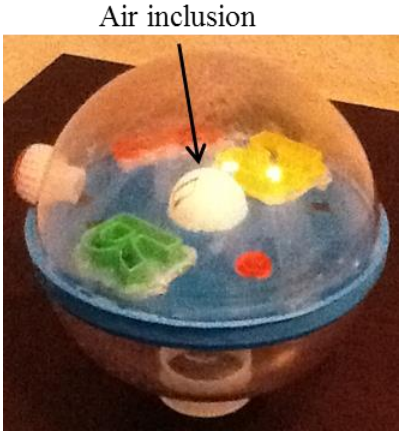

Figure 5.3. An in-house made phantom.

5.3.2.2. In Vivo experiments

Two studies were carried out with one healthy male volunteer after informed consent according to the IRB-approved protocol. All data were acquired with PMC enabled using a 32-channel head coil (Nova Medical, Wilmington, MA, USA). The marker was securely attached to a mouth guard which was individually molded to the volunteer's upper teeth using medical grade hydroplastic.

1. The characterization of size and location of B_0 field shifts within the brain at the different head orientations was performed using dual TE 3D FLASH with matrix; 256x256x176, voxel size; 1x1x1 mm, TR/TE1/TE2; 10.00/3.06/5.84 ms, and BW; 250 Hz/pixel. The volunteer was imaged at five orientations produced by roll rotation (around the z-axis of the scanner). The volunteer was instructed to move the head between poses but otherwise remain still.
2. The application of the proposed method to real motion with PMC enabled was performed using 3D MPRAGE with the same resolution as 3D FLASH, TR/TE/TI; 1800/1.99/1050 ms, and BW; 200 Hz/pixel. After the first half of the acquisition, the volunteer was instructed to perform a one-time head rotation around the z-axis. The motion pattern from the tracking log file is shown in Figure 5.9d. The field maps were also measured before and after motion and incorporated into the proposed reconstruction.

5.3.3. Data processing

The reconstruction was performed using MATLAB (version 12, The MathWorks Inc.), running on a Linux system. Before performing the image reconstruction, the data binning corresponding to motion pose was prepared the same as described in chapter 3. The voxel shift maps (VSM, $\boldsymbol{D}_0$) were generated as follows. First, the phase differences were calculated via the sum over channels N_c of the Hermitian inner product,

$$\Delta\emptyset = \arg\left(\sum_{q=1}^{N_c} IM_1^{q*} \cdot IM_2^{q}\right)$$

Second, since the phase-wrapping artifacts remain particularly near regions with large susceptibility, the phase differences were unwrapped using FSL-PRELUDE. Then, the unwrapped phases were multiplied by FSL-BET's binary mask (FMRIB Software Library, 2012). They were divided by (ΔTE) to yield the field maps in the unit of Hz, followed by a 3x3x3 median filter to reduce noise. Finally, the field map was converted to the VSM using Eq. 7-9 in (Robinson et al., 2011). The coil sensitivities were estimated

from the central 64x64x64 k-space data of 3D FLASH specific to motion pose. These data were truncated by a cosine tapper window, and then transformed to images by FFT. Each individual-channel image was divided by the RSS image. The *GNL* specific motion pose was analytically expanded as a linear combination of spherical harmonics (Eq. 4.7-4.8). Furthermore, the forward and inverse of NUFFT operators using min-max interpolation on a denser grid (2x oversampling) were calculated by using Fessler's NUFFT package (2014).

5.4. Results

5.4.1. Simulation results

Figure 5.4b shows that the RSS combination yielded images with severe artifacts caused by ΔB_0, *GNL*, and coil sensitivities misalignment. After applying standard augmented SENSE the residual geometric distortions and field artifacts remain (5.4d) particularly in the regions where the field effects are strongest as pointed out by the white (*GNL*'s effect) and yellow arrow (ΔB_0's effect) in the subtraction image (5.4e). Integrating the *GNL* corrections into the reconstruction, the strong distortion around the periphery can be effectively reduced (5.4f). The RMSE value was reduced from 0.24 to 0.06 (5.4g). Further improvements can be achieved when taking both ΔB_0 and *GNL* corrections into account (5.4h). Note that the regularization technique was not applied to this simulation, since we found that the outcome did not depend on regularization. This is likely due to the absence of noise. The very small residual difference (5.4i) may be due to an imperfection in the interpolation. The pixel values at transformed coordinates are only an approximation by considering a few closely neighboring known pixels. Consequently, the image will lose quality in particular in regions of strong distortion.

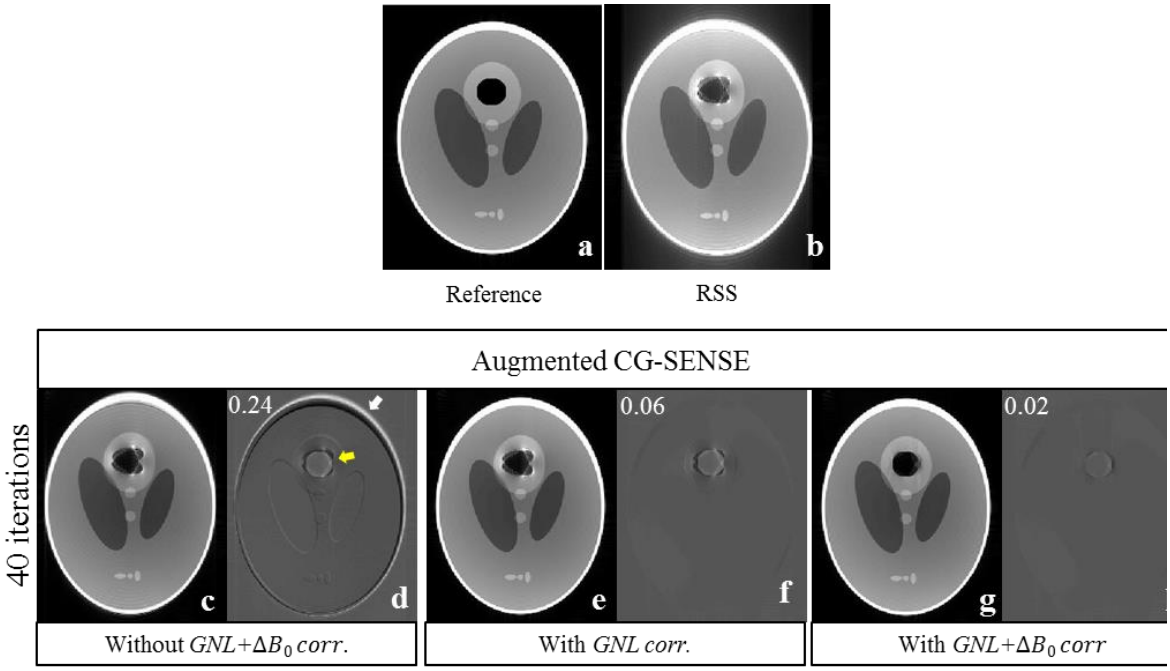

Figure 5.4. The reference (**a**), RSS (**b**), and corrected images (**c**, **e** and **g**) are identically windowed. The corrected images were reconstructed by the augmented SENSE (**c**), with integrated *GNL* correction (**e**), and with integrated *GNL* and ΔB_0 corrections (**g**). The image differences (**d**, **f**, and **h**) are the subtraction between each corrected image and reference. The RMSEs were superimposed on the upper left of the subtraction images.

5.4.2. Phantom Results

Figure 5.5a demonstrates the gradient displacements and B_0 inhomogeneity associated with two object positions. The susceptibility induced field inhomogeneities at air/oil boundaries were up to 670 Hz. It is obvious and expected that their orientations strongly depend on the object pose. The upper row of Figure 5.5b shows two individual distorted images reconstructed by the RSS method. The *GNL* and ΔB_0 resulted in strong shape differences as pointed out by white arrows (*GNL*'s effect) and black arrows (ΔB_0's effect) in the subtraction image. The bottom row of Figure 5.5b shows that after *GNL* and ΔB_0 corrections, their shapes appear highly similar to each other, i.e., the subtracted image showed very small differences, demonstrating the correct estimation of *GNL* and ΔB_0 in

this static situation. Inhomogeneity-induced signal loss due to intra-voxel dephasing was still present and is likely the main cause of the residual differences.

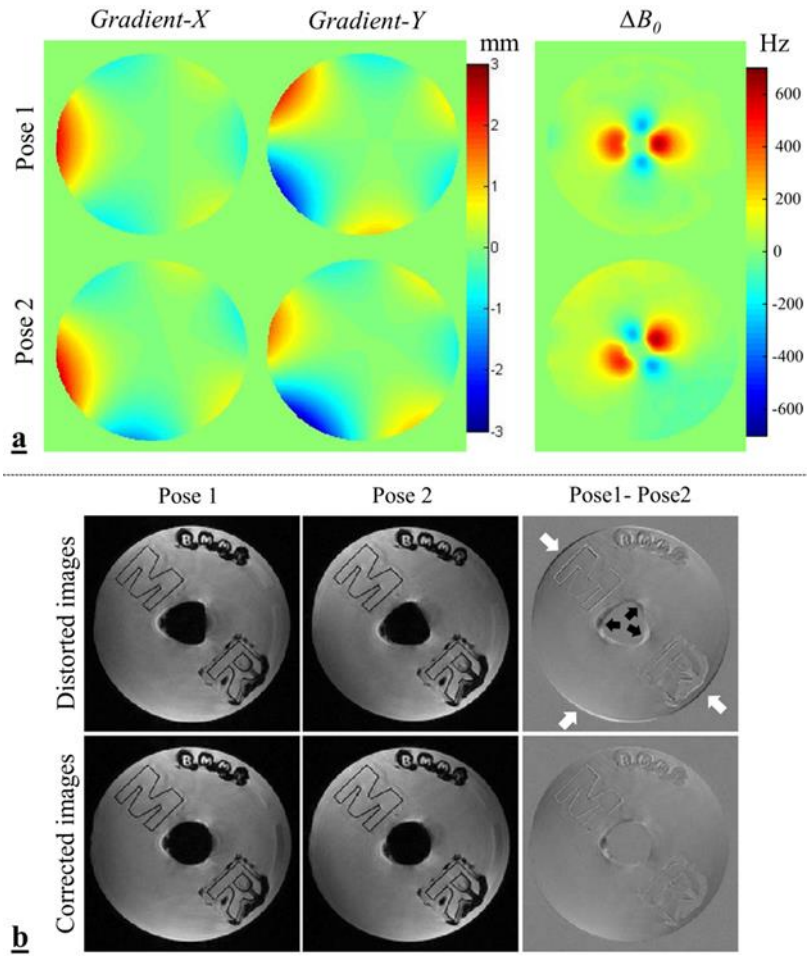

Figure 5.5. (a) The displacements of imaging gradients and B_0 field maps corresponding to pose1 and pose2. (**b**) *Upper row*: the images at different poses were acquired with PMC enabled leading to identical orientations despite large object motion, but still showing distortions due to *GNL* and ΔB_0. (**b**) *Bottom row:* the image quality can be improved after *GNL* and ΔB_0 correction.

Figure 5.6 shows all variants of these combined data reconstructed by the different reconstruction schemes. The RSS method yielded images with severe artifacts caused by *GNL*, ΔB_0, and coil sensitivities misalignment (1st column). Although, augmented SENSE largely reduced the sensitivity maps artifact, the spatial distortions and the blurring at the periphery and air/oil boundaries remain largely visible (2nd column). These regions further improved when both *GNL* and ΔB_0 were addressed in augmented SENSE (4th column). Nevertheless, high intensity variations near air/oil boundaries still remained high.

Figure 5.7a-5.7c show that the intensity variations near air/oil boundaries were remarkably reduced when using the regularization technique. The regularization parameter plays a crucial role in balancing the data-fidelity and regularization terms: small λ-values can lead to noisy estimates (5.7a) while a large λ (5.7c) results in over smoothing and loss of details. They also stabilized the solution, i.e., RMSEs at high iteration counts remain constant in contrast to conventional CG (λ=0) where RMSEs increase (5.7d).

Figure 5.8 illustrates the effectiveness of the proposed reconstruction on the under-sampled data; the fully sampled data were artificially under-sampled using acceleration/reduction factors R=2 and 3. The aliasing artifacts at high reduction factor (R=3) appear smaller in comparison to the image obtained by the standard reconstruction. This may be due to the geometry of coil sensitivity maps between two poses are different. The reconstructed images obtained the proposed reconstruction also appear closely similar to the reference as shown in the image differences (2nd and 4th columns). Conversely, the differences between the standard reconstructed image and the reference remain high.

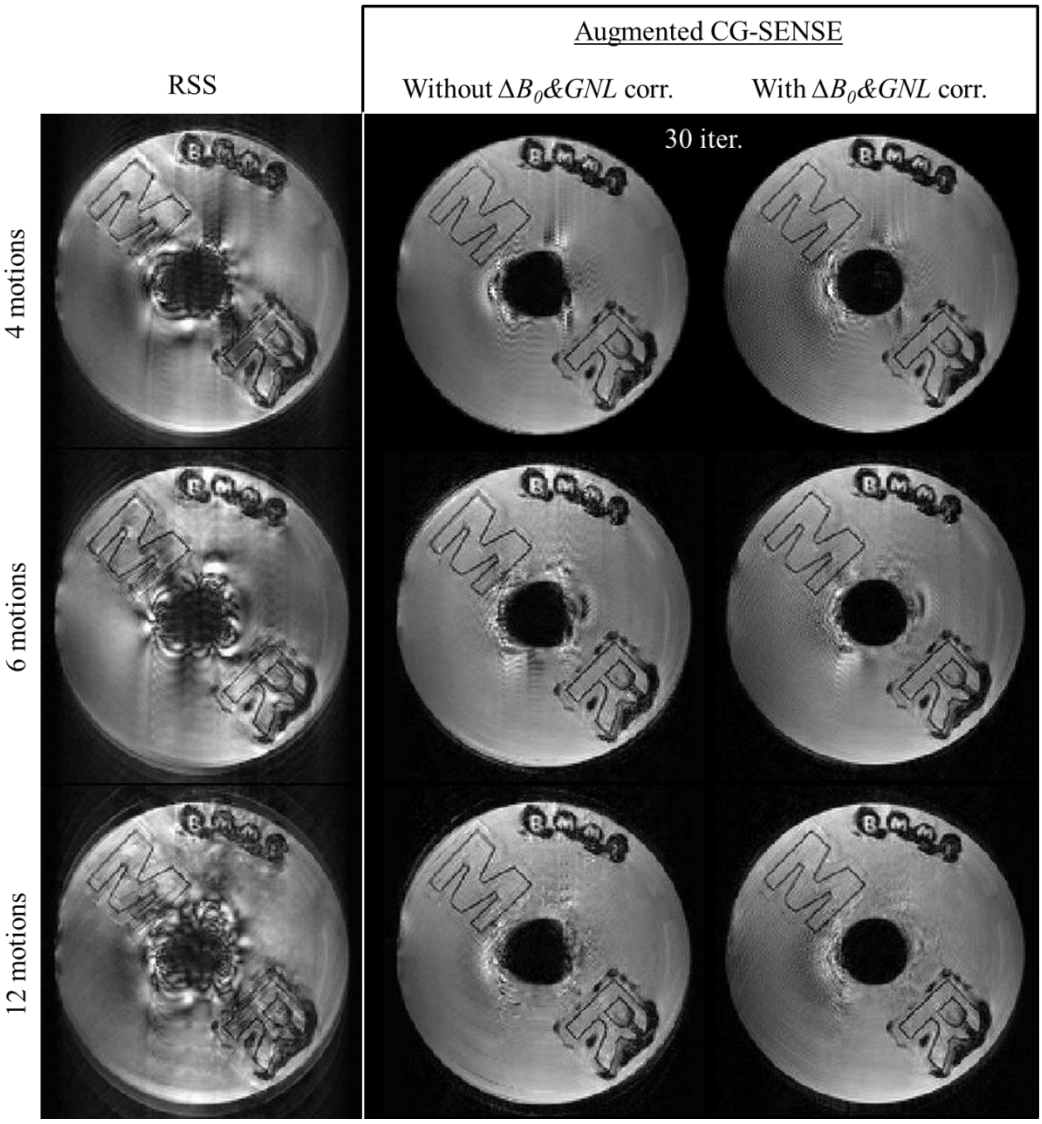

Figure 5.6. All images are identically windowed; *1st column:* RSS images; *2nd and 3rd columns:* images reconstructed by 30 iterations of augmented SENSE without and with integrated ΔB_0 and *GNL* corrections, respectively.

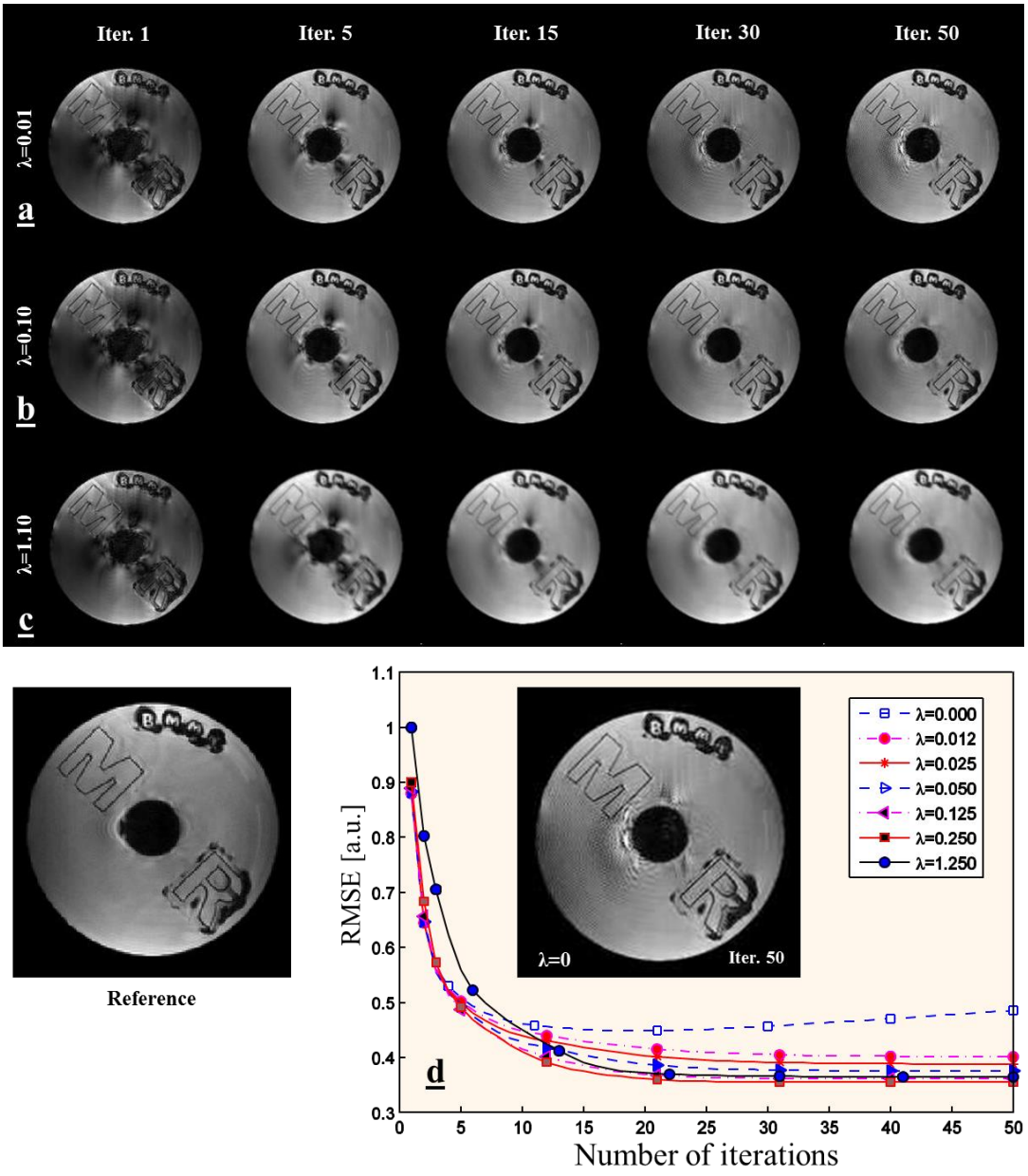

Figure 5.7. (**a-c**) The reconstructed images obtained by different iterative counts and different regularization parameters. (**d**) RMSE values are as functions of iteration counts and regularization parameters. The standard CG (λ=0) provided a diverging solution at high iteration counts.

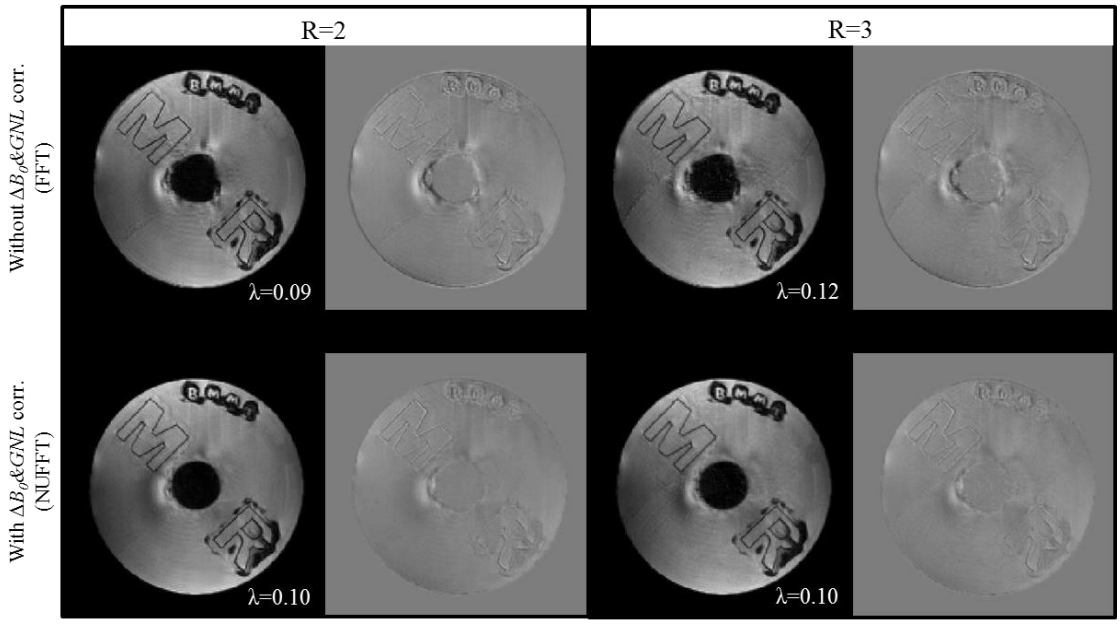

Figure 5.8. (1st and 2nd rows) The under-sampled data (R=2 and 3) were reconstructed by 30 iterations of augmented SENSE without and with integrated ΔB_0 and *GNL* corrections, respectively. (2nd and 4th columns) The difference between each reconstructed image and the reference.

5.4.3. In Vivo Results

Figures 5.9a and 5.9c show examples of B_0 field maps at identical slice positions relative to the volunteer's head, scanned at five poses with prospectively corrected image orientation. The B_0 field variations at the frontal lobes (5.9a) and the temporal lobe (5.9c) were up to 650 Hz and 400 Hz, respectively. Their amplitude and orientation changes relative to pose1 (0 degree) are shown in Figure 5.9b and 5.9d as field differences. The motion induced field differences in the above mentioned regions were up to 250 Hz and 150 Hz, respectively. This maximum observable B_0 shift (250 Hz) can cause 2.50 and 1.25 pixel shifts for the typical bandwidth of 100 and 200 Hz/ pixel, respectively.

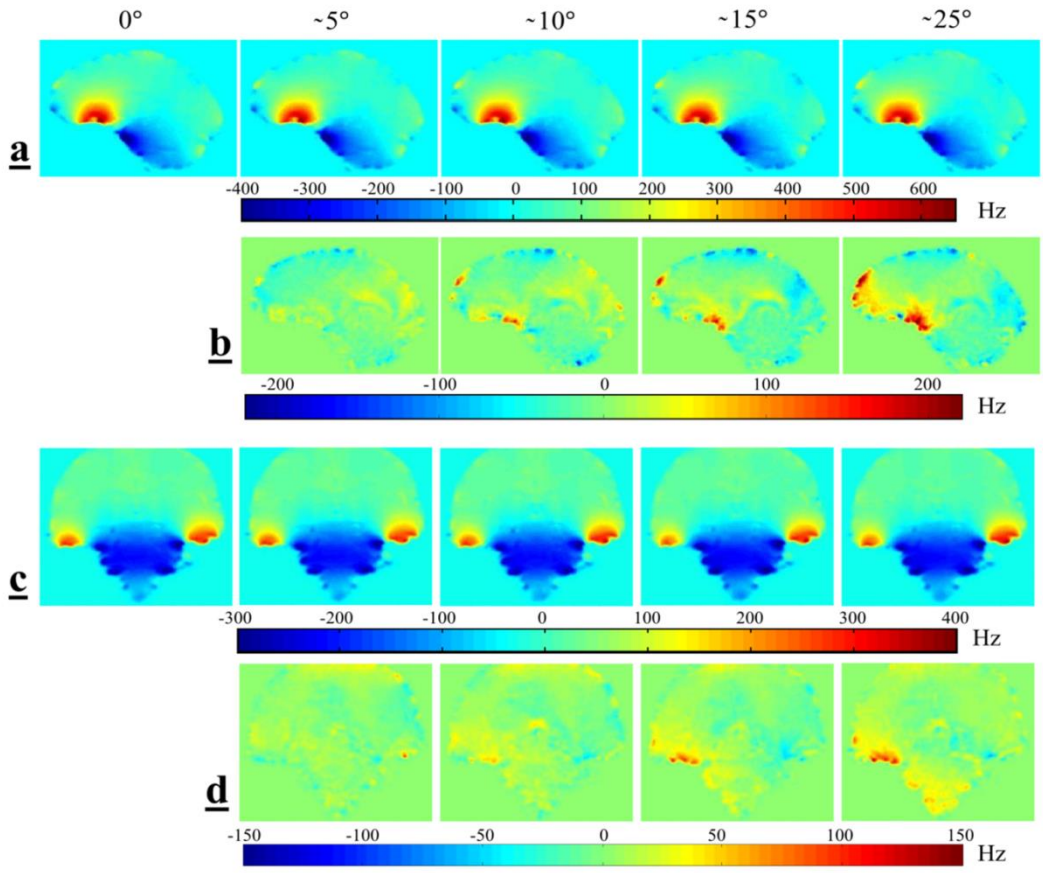

Figure 5.9. The susceptibility effects on the B_0 field in the brain during motion. The field map information acquired at five different constant poses (0°,~ 5°,~ 10°,~ 15°, and~ 25° around z-axis of the scanner). (**a**) and (**c**): the B_0 field maps for the frontal lobes (sagittal plane) and the temporal lobes (coronal plane), respectively. (**b**) and (**d**): the field differences between each field map and the field map obtained in the 0° reference position.

Figure 5.10a illustrates the B_0 field maps calculated from the full k-space, and the central k-space data with zero padding. The field map obtained from the central 32x32x32 k-space data appears largely different from the reference as shown in the field differences (5.10b). We found that the central 64x64x64 k-space data still provided the proper field map with small field differences (5.10b). In this study, these low-res field maps were chosen for the reconstruction in order to demonstrate that the reconstruction can be

accomplished with a low-res field map. Applying fast imaging sequences (Frahm et al., 1986) to acquire the low-res field maps per motion pose may be possible.

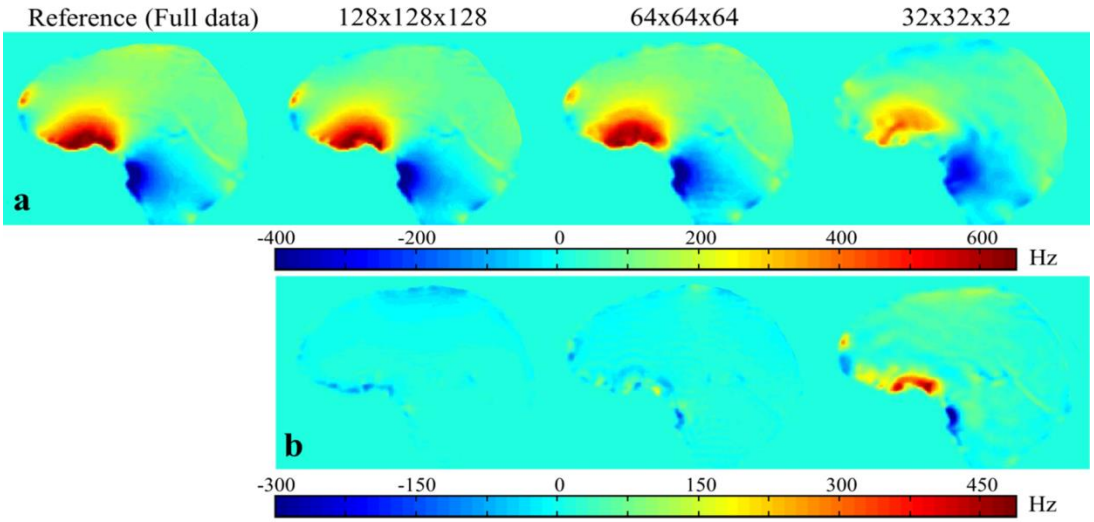

Figure 5.10. (**a**): the B_0 field maps at the frontal region of the brain reconstructed at different resolutions from the same k-space data. (**b**): the field differences between each field map and the field map obtained from full k-space data.

Figure 5.11d shows the motion pattern when the subject performed the head rotation during the data acquisition. A maximum rotation around the z-axis of approx. 23 degrees was detected. The motion data reconstructed by RSS (1st column) show blurring near the strong B_0 field inhomogeneity and gradient field nonlinearity as pointed by yellow arrow (a1) and white arrow (a2), respectively. Moreover, noise and blurring artifacts are obviously seen everywhere in Figure 5.11(a3). When the motion data was divided into two groups according to the tracking information, and then reconstructed by the augmented SENSE with integrated *GNL* correction the peripheries appear much sharper (e.g., white arrow in b2). However, the blurring generated by ΔB_0 as indicated by the yellow arrow (b1) still remains. Finally, the augmented SENSE with integrated ΔB_0 and *GNL* corrections can further improve the reconstructed image leading to a notable reduction of the above-mentioned artifacts (3rd column). It is obvious that the blurring

artifact in the yellow circle regions (c3) appears much less visible when compared with the same region of *GNL* corrected image (b3).

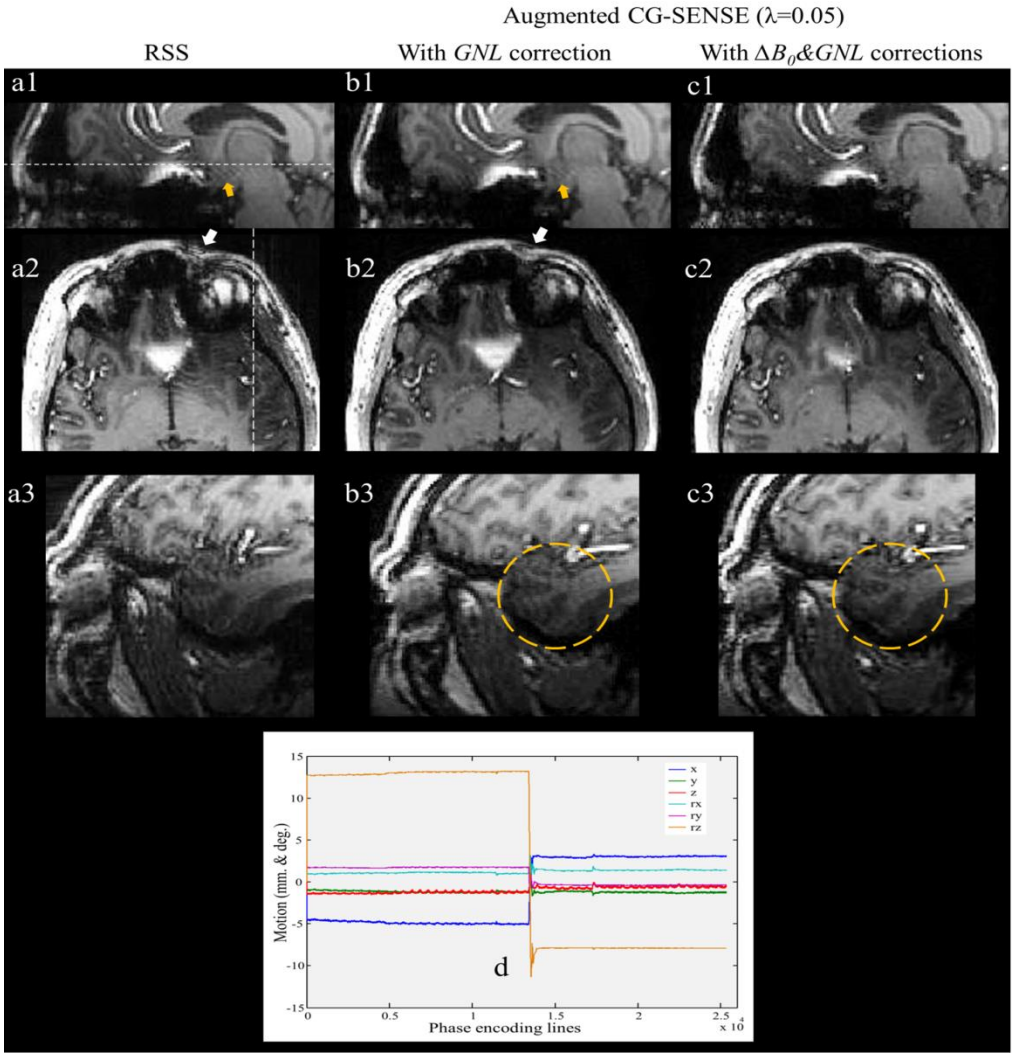

Figure 5.11. 1st column (**a1-a3**): RSS images of the prospectively motion-corrected acquisition. 2nd column (**b1-b3**): images after 10 iterations of augmented SENSE with integrated *GNL*. 3rd column (**c1-c3**): images with integrated ΔB_0 and *GNL* corrections. The axial images in the 2nd row and the sagittal images in the 3rd row correspond to the white lines in images **a1** and **a2**, respectively. The yellow circles in b3 and c3 highlight the artifact from ΔB_0 and the image improvement, respectively. **(d)**: six parameters of 3D motion from tracking log file (x, y, z shifts and R_x, R_y, R_z rotations).

Figure 5.12 demonstrates the effectiveness of the proposed method for undersampled acquisition. The full k-space data were artificially accelerated by factor 2x2 along both phase directions (phase and slice directions). Although, the standard SENSE (Pruessmann et al., 1999) provided the acceptable images (1st column), the remaining aliasing artifacts due to coil sensitivity misalignment and also the blurring artifacts caused by ΔB_0 and *GNL* are clearly visible as shown in the red circles. Note that sensitivity maps specific to the pose during the first half of the acquisition were used in standard SENSE. Superior image quality with very little remaining artifacts was achieved after applying the augmented SENSE with integrated ΔB_0 and *GNL* corrections (2nd column). Note that the regularization parameters superimposed on the reconstructed images were manually selected.

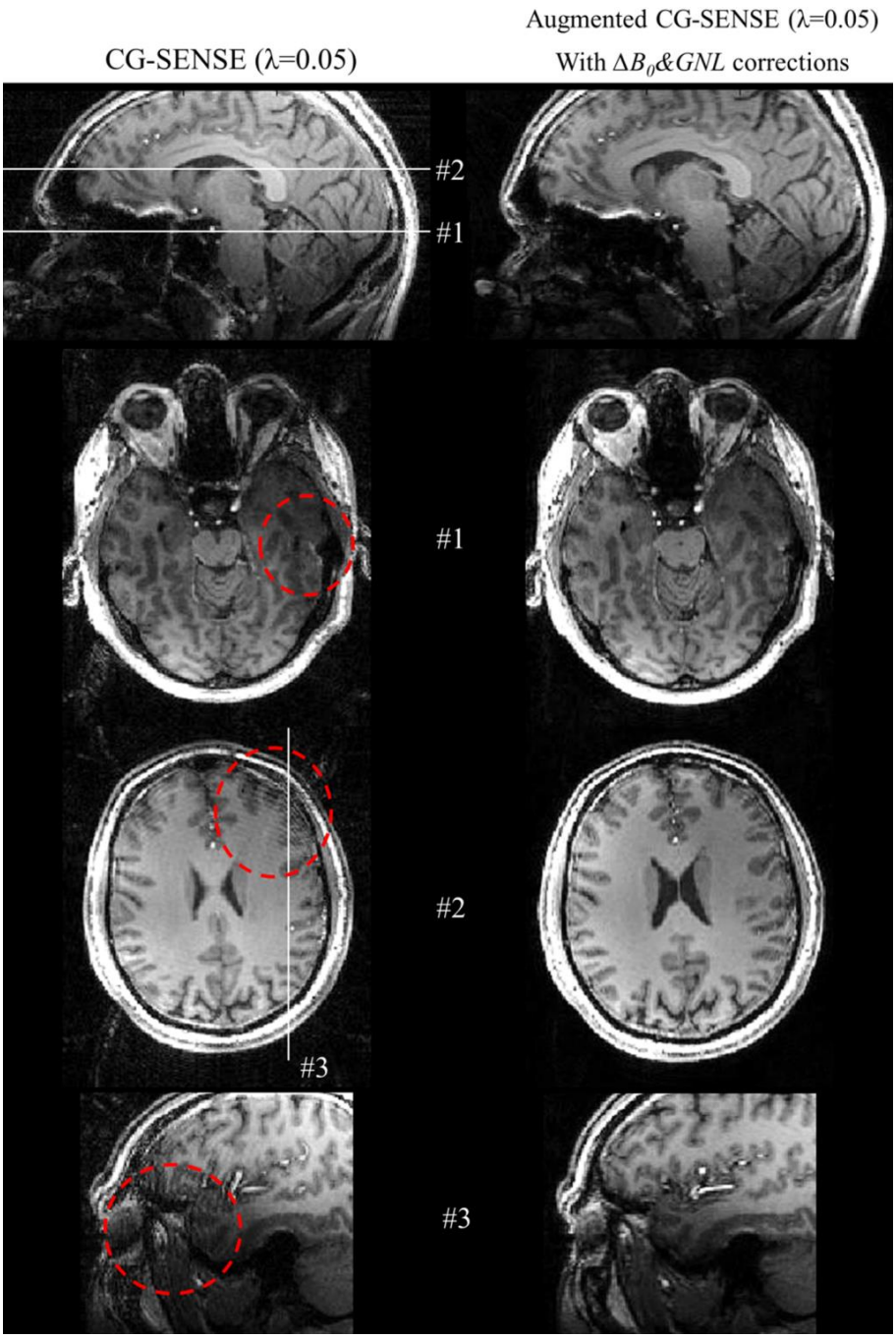

Figure 5.12. The 2x2 undersampled k-space data reconstructed by the standard SENSE and the augmented SENSE with integrated ΔB_0 and *GNL*. The axial images in the 2nd and 3rd rows correspond to the white lines #1 and #2, respectively. The sagittal images in the 4th row correspond to the white lines #3.

CHAPTER 6

6. DISCUSSION

PMC has great benefits for reducing motion artifacts, increasing image quality without time penalty when using external tracking, and avoiding sedation or rescanning of uncooperative patients. However, PMC alone may not be sufficient to restore image/data quality when there is large motion, and therefore, additional retrospective corrections become necessary to either correct some of the changes associated with real-time adjustments of scan coordinates or to implement PMC with other imaging applications.

In this work, the residual motion-related artifacts are categorized into three main types: 1) intensity shading caused by the fact that the RF receiving coils are fixed relative to moving subject, 2) the system imperfection, (i.e., gradient non-linearity induced geometric distortion), and 3) the subject-induced susceptibility effect on geometric distortion.

This work is also the first time that correction techniques have been presented, with respect to all the above residual artifacts. All corrections were combined into one step via the NUFFT model-based iterative regularized reconstruction. However, the performance of this reconstruction algorithm was highly dependent on the input parameters, such as the sensitivity maps, the magnetic displacement fields, the regularization parameters and the stopping criteria. A detailed discussion of the proposed correction scheme is presented in the following section.

6.1. The Coil Sensitivity

In chapter 3, there was strong concurrence between experiments and simulations in that the relative motion of coil sensitivity artifact was slightly visible in the fully sampled data, even with large motion scales. Nevertheless, the in vivo experiment provided evidence that some small structures near to the surface coil were highly interfered with in large motions (see Figure 3.15). The augmented SENSE can effectively recover this

obstacle. Furthermore, this reconstruction scheme was more advantageous for PMC data acquired using parallel imaging techniques. Recently, the effect of the motion-induced coil sensitivity alteration on non-Cartesian under-sampled data was investigated by Aksoy et al. (2008). Their results also suggest that it is necessary to correct for coil sensitivities in the case of large motions and high reduction factors. They give two reasons for this alteration: First, the change in coil sensitivity exposure increases with motion, and second, the retrospective counter-rotation of k-space trajectories for motion correction causes under-sampling in k-space, resulting in a higher "effective" reduction factor. However, we expect that this alteration in both Cartesian and non-Cartesian MRI that is PMC enabled, could be smaller than the use of a retrospective motion correction scheme, because the k-space trajectories are already realigned during data acquisition.

In this study, the quality of the reconstructed images relied on the sensitivity maps, which are key information required for the augmented SENSE reconstruction. Bammer et al. (2007) show that the coil sensitivity information can be directly retrieved from the navigator images, which were acquired using the spiral pulse sequence. The scan-time for this data was ~3-5 milliseconds for 2D low-res data. However, it may take longer when acquiring 3D data. Because of thr scan-time requirement to acquire the exact sensitivity data after adjustment of the imaging volume, Banerjee et al. (2013) propose that a 3D single dataset, acquired in the beginning of the actual scan, can be adjusted for each corresponding motion data. Their results show that the sensitivity maps calculated from single calibration data are sufficient for reconstructing the under-sampled data under the 1.5T scanner. In this study, the single calibration data was also used in the in vivo experiments (under 7T scanner). Small aliasing artifacts still remained (see Figure 3.14 and 3.15). This may be because of the influence of the coil loading effect, which depends in part on the dielectric properties of the load (subject) (Harvey, 2010). The effects of coil loading complicate MRI to the extent that resonant coils are often tuned or adjusted to compensate for the generally undesirable loading effect caused by the body being imaged, particularly at high field strength.

In phantom experiments, although the exact measured data were used to generate the coil sensitivities, the artifacts still remained high with a large motion even without data sub-sampling. These remaining artifacts are more likely an intensity variation rather than an aliasing artifact (see Figure 3.12, R=1 and 2). This may be due to the fact that the phantom was filled with oil, which shakes over a scan time, particularly when a large motion was performed. Consequently, the initial magnetizations are not fully returned before the next excitation pulse. This phenomenon is referred to as the 'spin-history effect', which can generate an intensity modulation (Muresan et al., 2005).

Note that the residual tracking errors may also interfere in the case of the frequent motion. To avoid such problem, therefore, one-time motion data were observed in this study. However, this correction scheme is expected to work well for the frequent motion datasets, when the mentioned interference is minimized.

6.2. Gradient Non Linearity Induced Distortion

Geometric distortions are a well-known problem in MRI, leading to pixel shifts with errors of up to several millimeters, thereby interfering with precise localization of anatomical structures (Archip et al., 2008). Aspects of geometric distortion due to gradient field non-linearity are the barrel distortion (2D and 3D); the potato chip effect (slice-selection, 2D);, and the bow-tie effect (2D) (Sumanaweera et al., 1994). Correction of the potato chip distortion in multi-slice 2D acquisitions is not addressed in this work, which focuses on 3D imaging. Both potato chip and bow-tie effects can be reduced considerably in 3D imaging, where phase encoding is used in two directions with full volume excitation and weak or a no slice selection gradient (Walton., 1997). The remaining barrel distortion in 3D acquisition can be corrected by applying a theoretically derived correction field as implemented in this study. Variations of the 2D slice selection distortion due to motion cause inconsistencies in single slice k-space data that will require a different approach for correction.

The application of the proposed method to experimental data demonstrated a clear improvement in image quality, especially in off-center slices. This can also confirm that

the vendor SPH-based gradient displacement is adequate for minimizing the geometric distortion in 3D PMC data. Note that the diameter of the Shepp-Logan phantom was approximately 220 mm and thus larger than the experimental phantom (~150 mm). The gradient non-linearity artifact is thus more prominent in the simulation than in the experimental data, especially in image edges. We demonstrated that this effect was more pronounced in off-center areas, i.e. for large objects and large object motion. As studied by Wang et al (2004a), the gradient field non-linearity in five different gradient sets varied strongly. Within a volume of $(240\ \text{mm})^3$, the geometric errors are between 10 and 25 mm in MRI systems equipped with fast gradient systems, while MRI systems equipped with conventional gradient systems showed only 2 to 4 mm errors. Other authors have reported maximum distortions over similar (but not identical) imaging volumes of: 9 mm at 1.5T (Doran et al., 2005), 7 mm at 3T (Baldwin et al., 2007). In this study, the maximum gradient-related displacements based on the manufacturer's SPH coefficients in measurement volumes of 200, 240 or $(300\ \text{mm})^3$ were 6.7, 14.5 or 43.8 mm, respectively. Therefore, the relevance of the *GNL* in PMC data will vary depending on the design of the gradient system.

The information about the gradient coil $\boldsymbol{D}_x(x,y,z),\ \boldsymbol{D}_Y(x,y,z), \boldsymbol{D}_z(x,y,z)$ (see Eq. 4.6 and 5.1) provided by the manufacturer is not always readily available. Optionally, several phantom-based distortion correction methods have been reported. Baldwin et al. (2007) characterized and corrected distortion using a three-dimensional (3D) grid phantom and elastic-body spline-kernel transformation function. Carmanos et al. (2010) constructed a DUPLO-based phantom and proposed distortion correction using information characterized by that phantom and spherical harmonic expansion. Schad et al. (1987) carried out an early investigation on two-dimensional (2D) MRI distortion correction using a 2D polynomial equation. Menuel et al. (2005) used phantom including cylindrical rods as fiducial points. Langlois et al. (1999) proposed a correction method based on the Fourier transform and a simple cubic phantom. This method obtained information about distortion to allow correction of both gradient nonlinearity and background field inhomogeneity for many subsequent patients via scans of a phantom of well-known

geometry. The gradient displacements obtained by the abovementioned methods may be incorporated into the proposed reconstruction.

6.3. B_0 Susceptibility Induced Distortion

The geometric distortion caused by susceptibility differences is much more complex, due to the field inhomogeneity's dependency on the material (e.g., tissue, bone, and air), shape of the object, and its orientation relative to the static B_0 field. Recently, the size and location of B_0 field shifts within the brain at 7T for different types of head movement were studied by Sulikowska et al. (2014). Their results show that the maximum B_0 field changes at the frontal lobe for pitch and yaw rotations are 4±2 and 8±11 Hz/degree, respectively. Other authors have reported maximum B_0 field differences caused by head movements of 160 Hz at 2.89T (Maclaren et al., 2013) and 50 Hz at 3T (Jezzard et al., 1999). In the present study, however, the field shifts are larger than those reported in previous studies. The motion induced field differences in the temporal and the frontal lobe were up to 150 Hz and 250 Hz, respectively. This may be because the scale of motion in our study is large with rotations of up to 25 degrees. In addition, the field maps were acquired with very high spatial resolution and therefore localized field variations were detected with little smoothing. In the simulation, residual artifacts after perfect PMC were clearly visible (see Figure 5.4b). These can be largely corrected by the proposed correction scheme (see Figure 5.4h). In the in vivo experiments, the largest B_0 field change due to head movement during the acquisition was 250 Hz, which caused 1.25 pixels shift for a readout BW of 200 Hz/pixel. This field change generated a residual blurring artifact as illustrated in Figure 5.11. However, this artifact is somewhat small. The images reconstructed by RSS and standard SENSE appeared slightly degraded, but still acceptable. This is due to the use of a small head coil (32-channel) that restricted movement. Conversely, when using a larger head coil that allows greater motion, the artifacts may become a more relevant challenge as demonstrated in the phantom experiments. The proposed reconstruction may become more important to improve the image quality especially when scanning heads of children or uncooperative patients. In addition, correction of distortions due to B_0 variation may be most important in

sequences that are highly susceptible to field variations, such as multi-shot EPI, for which the correction may be more relevant even for smaller motions than in the examples in this study with a less sensitive FLASH acquisition.

It is important to note that the proposed reconstruction required an accurate field map. In this study, all acquired GRE data had sufficiently high SNR and small ΔTE. As a result, artifact-free phase differences and field maps can be achieved by using a fast and simple method (i.e., the Hermitian inner product, HP). However, Lu et al. (2008) showed that the naive HP exhibits higher noise sensitivity than SENSE-based methods (Bernstein et al., 1994; Walsh et al., 2000). In addition, using long TEs or high ΔTE may cause severely wrapped phase data that require phase unwrapping with more advanced but computationally expensive methods, e.g. UMPIRE (Robinson et al., 2014).

6.4. Regularization Parameter

Basically, the choice of the regularization parameter λ depends on the noise level (Lin et al., 2008). Difference choices of parameter λ result in a trade-off between the smoothness of the signal, when $\|\boldsymbol{L}v_0\|_2^2$ is small, and a good fit-to-data if $\|m - \boldsymbol{E}v_0\|_2^2$ is small. It should be noted that, even λ=0 in simulation studies (chapters 3, 4, and 5) the best approximate solutions can still be achieved. This is likely due to the absence of noise. However, in experimental studies, regularization played an important role in optimizing the high intensity variations in regions where the magnetizations were perturbed by the strong field inhomogeneities (see Figure 5.6). Moreover, regularization can also prevent divergence of the solution at high iteration counts (see Figure 5.7). In this study, the optimal λ was manually adjusted for subjective good image-quality. Optionally, several quantitative methods for selection of λ such as the L-curve method (Vogel, 1996), generalized cross-validation (Golub et al., 1979) and the discrepancy principle (Galatsanos et al., 1992) may be useful to select the most appropriate λ for the proposed reconstruction. In addition, the tridiagonal regularization matrix also provides a smoother solution (Hansen, 1998) rather than using an identity matrix (the result is not shown in this study). This is advantageous for the regions with high-intensity variation.

6.5. The NUFFT

Although, the inverse FFT has served the MR community very well for image reconstruction, it is unable to directly apply to a motion or to non-uniform sampled MR-data. Fortunately, the NUFFT can overcome such a limitation, and has been widely used (Atkinson et al., 2003; Fessler et al., 2003). The NUFFT not only effectively works for non-uniform k-space data, but also non-uniform image data (Capozzoli et al., 2013; Tao et al., 2015), which is commonly referred to type-1 of NUFFT. The effectiveness of the NUFFT type-1 for correcting the geometric distortion caused by *GNL* in a static MRI with Cartesian sampling is presented in Tao et al. (2015). The application of the NUFFT method for correcting the geometric distortion in prospectively motion-corrected MR-data with Cartesian sampling is demonstrated for first time in this work.

The geometric distortion correction, which is also called image warping, is the process of transforming a sampled image from one coordinate system to another. The two coordinate systems are related to each other by the mapping function of the spatial transformation. In general, during the warping procedure, an interpolation is required for resampling the intensity values in the new coordinates. Several commonly used interpolation algorithms have been suggested, such as nearest neighbor interpolation, linear interpolation, and spline interpolation (Gonzalez et al., 2006). The linear and spline interpolations are most commonly used in medical image processing, because they are computationally efficient (Lehmann et al., 1999; Unser, 2002). Unfortunately, they tend to smooth the image, particularly in the presence of high spatial frequency components (Thevenaz et al., 2000). In contrast, NUFFT-based interpolation (Fessler et al., 2003) can effectively preserve high spatial frequency components including boundaries and small structures (e.g., the cerebellar gyri as well as the morphology of vascular structures) as demonstrated by Tao et al. (2015). Moreover, the NUFFT is also practical for the partial image obtained from a few lines of k-space, as demonstrated in this work. Recently, Capozzoli et al. (2013) concur that the NUFFT significantly outperforms, in terms of accuracy, other techniques, such as nearest neighbor, piecewise linear, four-point and six-point cubic, and the truncated Sinc. However, its accuracy depends on the choices of the

convolving window and the oversampling rate. Using a large window and a high oversampling rate is a computational burden. The tradeoff between accuracy and processing speed, as well as memory requirements, may be managed by changing the window size of the kernel and the over sampling rate (Song et al., 2009). Some work has been done to fine optimal parameters to balance accuracy and computational costs. For example, Beatty et al. (2005) used a minimal oversampling rate, from 1.125 to 1.375 instead of the typically employed grid oversampling ratio of two, to reduce the high computational memory demand in 3D.

CHAPTER 7

7. UNRESOLVED CHALLENGES AND CONCLUSION

7.1. Unresolved Challenges

First, the explicit determination of coil sensitivities for each motion pose is time consuming. Although the sensitivity maps can be prepared by adjusting the initial calibration dataset as demonstrated in chapter 3, the artifacts still remain. However, it is fortunate that the coil sensitivity estimation does not require high resolution (Bammer et al., 2007; Pruessmann et al., 1999; Qu et al., 2007). Thus, using a fast pre-scan for acquiring low-res sensitivity maps prior to imaging (Frahm et al., 1986) may be possible.

Second, although several techniques for dynamic characterization of the B_0 field have been developed (Hutton et al., 2002; In et al., 2012), they require additional scan time and assume that the subject remains still for each measurement step. For stronger motion, the distortion caused by B_0 field inhomogeneity has been considered for single-shot EPI time series where each acquisition can provide a field map (Ooi et al., 2011; 2013). Extension to multi-shot EPI and other spin-warp sequences is not obvious. Recently, there have been several efforts to predict field maps from air/tissue susceptibility distributions of the anatomy using magnetic field models (Jenkinson et al., 2004; Kock et al., 2006) which neither require additional scan time nor suffer from low SNR at air/tissue boundaries. Boegle et al. (2010) show that the quality of distortion correction using the model-based field maps in phantom experiments with arbitrary orientations is comparable to distortion correction based on measured field maps of the same object. The distortion-free PMC imaging of a large moving object may be feasible if such corrections are employed.

Third, even if the field maps can be determined for each motion pose, local signal dropouts cannot be recovered retrospectively. Such signal variations due to intra-voxel dephasing are likely to be the cause of residual artifacts in the corrected images (see Figure 5.5b: the corrected images are geometrically correct, but show significant signal loss around the air inclusion). Dynamic shimming may be able to address this aspect in

part. Recently, Ward et al (2002) introduced real-time auto shimming by means of a navigator pulse sequence (shim NAV) to acquire field information for first order shim-compensated EPI acquisition in the presence of subject motion. A 3D EPI navigator (Hess et al., 2011) was also employed to achieve simultaneous motion and shim correction in single voxel MR spectroscopy. Keating et al. (2012), showed that fast B_0 mapping for an MRS voxel (20x20x1.17 mm3) can be performed in approximately 120 msec. Moreover, field map free dynamic shimming (Shi et al., 2015) using a larger number of field map templates, together with non-linear registration methods can produce a homogeneous field without acquisition time penalty. Knowing the higher than first order dynamic field fluctuations around the head may be helpful. These fluctuations can be monitored by field cameras (Barmet et al., 2008) concurrently with image acquisition. Feedback of these global field changes into the high order shim coils (Duerst et al., 2015) or reconstruction (Wilm et al., 2011) may minimize the field fluctuation-induced artifacts in motion correction.

Finally, the proposed reconstruction is much more time consuming than traditional Fourier reconstruction, due to the separation of data into several pipelines and iterative calculations. The applications of parallel computing by graphics processing units (GPUs) (Hansen et al., 2008), and coil compression techniques (Zhang et. al., 2013) that reduce the data from many channels into fewer virtual coils, may be ideally suited to improve the reconstruction speed.

7.2. Conclusion

This work provides evidence that large scale head motion in relation to a fixed multi-channel receiver coil can introduce unwanted signal variations in particular when using parallel imaging. This residual artifact was mitigated when the coil sensitivities specific motion were given. The coil sensitivity maps can be prepared by directly measuring or adjusting a single calibration datum. The correction process can be done via the proposed model-based iterative reconstruction.

This work also demonstrates that geometric distortions due to gradient non-linearity can induce residual artifacts even in perfectly prospectively motion-corrected data, in particular in off-center regions. These artifacts can be minimized by the proposed technique that accounts the NUFFT type-1 instead of FFT. Unlike FFT, the NUFFT can directly be used to transform the distorted image to uniform k-space. The combined correction of gradient non-linearity and sensitivity map variation leads to a pronounced reduction of residual motion artifacts in prospectively motion-corrected data of the homogeneous object.

In an in vivo experiment, not only the gradient field nonlinearity caused the geometric distortion after PMC application, but also caused the subject-induced susceptibility effect, especially at air/tissue interfaces. The field changes occur as the subject's orientation changes relative to the B_0 field. We found that if the magnetic displacements at any orientation are given, this residual artifact can be alleviated by the proposed model-based iterative reconstruction. The combined corrections of gradient non-linearity, sensitivity map variation, and subject-induced distortions leads to a more pronounced reduction of residual motion artifacts in non-homogeneous object and human brain with PMC application.

BIBILIOGRAPHY

Ackerman, J., Offutt, M., Buxton, R., Brady, T. (1986). Rapid 3D tracking of small RF coils. *In: Proceedings 5th Scientific Meeting, Society for Magnetic Resonance in Medicine, Montreal*, p 1131-1132.

Aksoy, M., Bammer, R. (2008). Effect of Motion-Induced Altered Coil Sensitivity on Parallel Imaging Performance. *In: Proceedings of the 16th scientific meeting, International Society for Magnetic Resonance in Medicine, Toronto*, p 3111.

Aksoy, M., Forman, C., Straka, M., Cukur, T., Hornegger, J., Bammer, R. (2012). Hybrid prospective and retrospective head motion correction to mitigate cross-calibration errors. *Magn Reson Med, 67*(5), 1237-1251.

Aksoy, M., Forman, C., Straka, M., Skare, S., Holdsworth, S., Hornegger, J., Bammer, R. (2011). Real-time optical motion correction for diffusion tensor imaging. *Magn Reson Med, 66*(2), 366-378.

Aksoy, M., Liu, C., Moseley, M., Bammer, R. (2006). A self-navigated spiral in & out pulse sequence design for retrospective motion correction. *In: Proceedings of the 14th Annual Meeting of ISMRM, Seattle, WA, USA*, p 3197.

Alhamud, A., Tisdall, M. D., Hess, A. T., Hasan, K. M., Meintjes, E. M., van der Kouwe, A. J. (2012). Volumetric navigators for real-time motion correction in diffusion tensor imaging. *Magn Reson Med, 68*(4), 1097-1108.

Anderson, C., Dahleh, M. (1996). Rapid computation of the discrete Fourier transform. *SIAM J. Sci. Comput., 17*(4), 913-919.

Andrews-Shigaki, B. C., Armstrong, B. S., Zaitsev, M., Ernst, T. (2011). Prospective motion correction for magnetic resonance spectroscopy using single camera Retro-Grate reflector optical tracking. *J Magn Reson Imaging, 33*(2), 498-504.

Archip, N., Clatz, O., Whalen, S., Dimaio, S. P., Black, P. M., Jolesz, F. A., . . . Warfield, S. K. (2008). Compensation of geometric distortion effects on intraoperative magnetic resonance imaging for enhanced visualization in image-guided neurosurgery. *Neurosurgery, 62*(3 Suppl 1), 209-215; discussion 215-206.

Atkinson, D., Hill, D. L. (2003). Reconstruction after rotational motion. *Magn Reson Med, 49*(1), 183-187.

Atkinson, D., Hill, D. L., Stoyle, P. N., Summers, P. E., Clare, S., Bowtell, R., Keevil, S. F. (1999). Automatic compensation of motion artifacts in MRI. *Magn Reson Med, 41*(1), 163-170.

Atkinson, D., Larkman, D. J., Batchelor, P. G., Hill, D. L., Hajnal, J. V. (2004). Coil-based artifact reduction. *Magn Reson Med, 52*(4), 825-830.

Baldwin, L. N., Wachowicz, K., Thomas, S. D., Rivest, R., Fallone, B. G. (2007). Characterization, prediction, and correction of geometric distortion in 3 T MR images. *Med Phys, 34*(2), 388-399.

Bammer, R., Aksoy, M., Liu, C. (2007). Augmented generalized SENSE reconstruction to correct for rigid body motion. *Magn Reson Med, 57*(1), 90-102.

Banerjee, S., Beatty, P. J., Zhang, J. Z., Shankaranarayanan, A. (2013). Parallel and partial Fourier imaging with prospective motion correction. *Magn Reson Med, 69*(2), 421-433.

Barmet, C., De Zanche, N., Pruessmann, K. P. (2008). Spatiotemporal magnetic field monitoring for MR. *Magn Reson Med, 60*(1), 187-197.

Barmet, C., De Zanche, N., Wilm, B. J., Pruessmann, K. P. (2009). A transmit/receive system for magnetic field monitoring of in vivo MRI. *Magn Reson Med, 62*(1), 269-276.

Batchelor, P. G., Atkinson, D., Irarrazaval, P., Hill, D. L., Hajnal, J., Larkman, D. (2005). Matrix description of general motion correction applied to multishot images. *Magn Reson Med, 54*(5), 1273-1280.

Beatty, P., Nishimura, D., Pauly, J. (2005). Rapid gridding reconstruction with a minimal oversampling ratio. *IEEE Trans Med Imaging, 24*(6), 799-808.

Bernstein, M. A., Grgic, M., Brosnan, T. J., Pelc, N. J. (1994). Reconstructions of phase contrast, phased array multicoil data. *Magn Reson Med, 32*(3), 330-334.

Beylkin, G. (1995). On the Fast Fourier Transform of Functions with Singularities. *Applied and Computational Harmonic Analysis, 2*(4), 363-381.

Boegle, R., Maclaren, J., Zaitsev, M. (2010). Combining prospective motion correction and distortion correction for EPI: towards a comprehensive correction of motion and susceptibility-induced artifacts. *MAGMA, 23*(4), 263-273.

Breuer, F. (2006). *Development and application of efficient strategies for parallel magnetic resonance imaging (Doctoral dissertation).* Retrieved from https://opus.bibliothek.uni-wuerzburg.de/files/1760/thesis_breuer.pdf.

Brown, T., Kuperman, J., Erhart, M., White, N. S., Roddey, J., Shankaranarayanan, A., . . . Dale, A. (2010). Prospective motion correction of high-resolution magnetic resonance imaging data in children. *Neuroimage, 53*(1), 139-145.

Bydder, M., Larkman, D. J., Hajnal, J. V. (2002a). Combination of signals from array coils using image-based estimation of coil sensitivity profiles. *Magn Reson Med, 47*(3), 539-548.

Bydder, M., Larkman, D. J., Hajnal, J. V. (2002b). Detection and elimination of motion artifacts by regeneration of k-space. *Magn Reson Med, 47*(4), 677-686.

Callaghan, M. F., Josephs, O., Herbst, M., Zaitsev, M., Todd, N., Weiskopf, N. (2015). An evaluation of Prospective Motion Correction (PMC) for high resolution quantitative MRI. *Frontiers in Neuroscience, 9*.

Capozzoli, A., Curcio, C., Liseno, A. (2013). FAST GPU-BASED INTERPOLATION FOR SAR BACK-PROJECTION. *Progress in Electromagnetics Research, 133*.

Caramanos, Z., Fonov, V. S., Francis, S. J., Narayanan, S., Pike, G. B., Collins, D. L., Arnold, D. L. (2010). Gradient distortions in MRI: Characterizing and correcting for their effects on SIENA-generated measures of brain volume change. *Neuroimage, 49*(2), 1601-1611.

Chen, Z., Ma, C. M., Paskalev, K., Li, J., Yang, J., Richardson, T., . . . Chen, L. (2006). Investigation of MR image distortion for radiotherapy treatment planning of prostate cancer. *Phys Med Biol, 51*(6), 1393-1403.

Derbyshire, J. A., Wright, G. A., Henkelman, R. M., Hinks, R. S. (1998). Dynamic scan-plane tracking using MR position monitoring. *J Magn Reson Imaging, 8*(4), 924-932.

Doran, S. J., Charles-Edwards, L., Reinsberg, S. A., Leach, M. O. (2005). A complete distortion correction for MR images: I. Gradient warp correction. *Phys Med Biol, 50*(7), 1343-1361.

Dumoulin, C. L., Souza, S. P., Darrow, R. D. (1993). Real-time position monitoring of invasive devices using magnetic resonance. *Magn Reson Med, 29*(3), 411-415.

Dutt, A., Rokhlin, V. (1993). Fast Fourier Transforms for Nonequispaced Data. *SIAM Journal on Scientific Computing, 14*(6), 1368-1393.

Dutt, A., Rokhlin, V. (1995). Fast Fourier Transforms for Nonequispaced Data, II. *Applied and Computational Harmonic Analysis, 2*(1), 85-100.

Edelstein, W. A., Hutchison, J. M., Johnson, G., Redpath, T. (1980). Spin warp NMR imaging and applications to human whole-body imaging. *Phys Med Biol, 25*(4), 751-756.

Ehman, R. L., Felmlee, J. P. (1989). Adaptive technique for high-definition MR imaging of moving structures. *Radiology, 173*(1), 255-263.

Eviatar, H., Saunders, J., Hoult, D. (1997). Motion compensation by gradient adjustment. *In: Proceedings of the International Society for Magnetic Resonance in Medicine, Vancouver*, p 1898.

Feinberg, D. A., Giese, D., Bongers, D. A., Ramanna, S., Zaitsev, M., Markl, M., Gunther, M. (2010). Hybrid ultrasound MRI for improved cardiac imaging and real-time respiration control. *Magn Reson Med, 63*(2), 290-296.

Fessler, J. A. (2010). Model-Based Image Reconstruction for MRI. *IEEE Signal Processing Magazine, 27*(4), 81-89.

Fessler, J. A. (2014). Image reconstruction toolbox. The University of Michigan, Ann Arbor, Michigan, USA. http://web.eecs.umich.edu/_fessler/irt/fessler.tgz. Accessed 12 April 2014.

Fessler, J. A., Sutton, B. P. (2003). Nonuniform fast Fourier transforms using min-max interpolation. *IEEE Trans. Sig. Proc., 51*(2), 560-574.

FMRIB Software Library, U. o. O. (2012). http://www.fmrib.ox.ac.uk/fsl. Accessed on 12 April 2015.

Forman, C., Aksoy, M., Hornegger, J., Bammer, R. (2010). Self-encoded marker for optical prospective head motion correction in MRI. *Med Image Comput Comput Assist Interv, 13*(Pt 1), 259-266.

Frahm, J., Haase, A., Matthaei, D. (1986). Rapid NMR imaging of dynamic processes using the FLASH technique. *Magn Reson Med, 3*(2), 321-327.

Fu, Z. W., Wang, Y., Grimm, R. C., Rossman, P. J., Felmlee, J. P., Riederer, S. J., Ehman, R. L. (1995). Orbital navigator echoes for motion measurements in magnetic resonance imaging. *Magn Reson Med, 34*(5), 746-753.

Galatsanos, N., Katsaggelos, A. (1992). Methods for choosing the regularization parameter and estimating the noise variance in image restoration and their relation. *Image Processing, IEEE Transactions on, 1*(3), 322-336.

Glover, G., Pelc, N. (1986). Method for correcting image distortion due to gradient nonuniformity. *US Patent, 4,591,789*.

Golub, G., Heath, M., Wahba, G. (1979). Generalized cross-validation as a method for choosing a good ridge parameter. *Technometrics, 21*(2), 215-223.

Golub, G. H., Loan, C. F. V. (1996). *Matrix computations (3rd ed.)*: Johns Hopkins University Press.

Gonzalez, R. C., Woods, R. E. (2006). *Digital Image Processing (3rd Edition)*: Prentice-Hall, Inc.

Greengard, L., Lee, J. (2004). Accelerating the nonuniform fast Fourier transform. *SIAM Review, 46*(3), 443-454.

Griswold, M. A., Breuer, F., Blaimer, M., Kannengiesser, S., Heidemann, R. M., Mueller, M., . . . Jakob, P. M. (2006). Autocalibrated coil sensitivity estimation for parallel imaging. *NMR Biomed, 19*(3), 316-324.

Gunter, J. L., Bernstein, M. A., Borowski, B. J., Ward, C. P., Britson, P. J., Felmlee, J. P., . . . Jack, C. R. (2009). Measurement of MRI scanner performance with the ADNI phantom. *Med Phys, 36*(6), 2193-2205.

Haacke, E. M. (1999). *Magnetic resonance imaging : physical principles and sequence design*. New York: Wiley.

Haeberlin, M., Kasper, L., Barmet, C., Brunner, D. O., Dietrich, B. E., Gross, S., . . . Pruessmann, K. P. (2015). Real-time motion correction using gradient tones and head-mounted NMR field probes. *Magn Reson Med, 74*(3), 647-660.

Hansen, P. (1998). *Rank-deficient and discrete ill-posed problems: numerical aspects of linear inversion* (Vol. 4): Siam.

Harvey, P. R. (2010). Magnetic resonance imaging system and method: Google Patents.

Harvey, P. R., Katznelson, E. (1999). Modular gradient coil: A new concept in high-performance whole-body gradient coil design. *Magn Reson Med, 42*(3), 561-570.

Herbst, M., Maclaren, J., Korvink, J., Zaitsev, M. (2011). A practical tracking system to avoid motion artifacts. *In: Proceedings 19th Scientific Meeting, International Society for Magnetic Resonance in Medicine, Montreal*, p 2683.

Hoge, R. D., Kwan, R. K., Pike, G. B. (1997). Density compensation functions for spiral MRI. *Magn Reson Med, 38*(1), 117-128.

Hu, H. H., Madhuranthakam, A. J., Kruger, D. G., Glockner, J. F., Riederer, S. J. (2005). Continuously moving table MRI with SENSE: application in peripheral contrast enhanced MR angiography. *Magn Reson Med, 54*(4), 1025-1031.

Jackson, J., Meyer, C., Nishimura, D., Macovski, A. (1991). Selection of a convolution function for Fourier inversion using gridding [computerised tomography application]. *IEEE Trans Med Imaging, 10*(3), 473-478.

Jackson, J. I., Meyer, C. H., Nishimura, D. G., Macovski, A. (1991). Selection of a convolution function for Fourier inversion using gridding [computerised tomography application]. *IEEE Trans Med Imaging, 10*(3), 473-478.

Janke, A., Zhao, H., Cowin, G. J., Galloway, G. J., Doddrell, D. M. (2004a). Use of spherical harmonic deconvolution methods to compensate for nonlinear gradient effects on MRI images. *Magn Reson Med, 52*(1), 115-122.

Janke, A., Zhao, H., Cowin, G. J., Galloway, G. J., Doddrell, D. M. (2004b). Use of spherical harmonic deconvolution methods to compensate for nonlinear gradient effects on MRI images. *Magn Reson Med, 52*(1), 115-122.

Jenkinson, M. (2003). Fast, automated, N-dimensional phase-unwrapping algorithm. *Magn Reson Med, 49*(1), 193-197.

Jezzard, P., Balaban, R. S. (1995). Correction for geometric distortion in echo planar images from B0 field variations. *Magn Reson Med, 34*(1), 65-73.

Jezzard, P., Clare, S. (1999). Sources of distortion in functional MRI data. *Hum Brain Mapp, 8*(2-3), 80-85.

Jovicich, J., Czanner, S., Greve, D., Haley, E., van der Kouwe, A., Gollub, R., . . . Dale, A. (2006). Reliability in multi-site structural MRI studies: effects of gradient non-linearity correction on phantom and human data. *Neuroimage, 30*(2), 436-443.

Kim, D. H., Adalsteinsson, E., Spielman, D. M. (2003). Simple analytic variable density spiral design. *Magn Reson Med, 50*(1), 214-219.

Kober, T., Marques, J. P., Gruetter, R., Krueger, G. (2011). Head motion detection using FID navigators. *Magn Reson Med, 66*(1), 135-143.

Koch, K., Rothman, D., de Graaf, R. A. (2009). Optimization of static magnetic field homogeneity in the human and animal brain in vivo. *Prog Nucl Magn Reson Spectrosc, 54*(2), 69-96.

Korin, H. W., Farzaneh, F., Wright, R. C., Riederer, S. J. (1989). Compensation for effects of linear motion in MR imaging. *Magn Reson Med, 12*(1), 99-113.

Langlois, S., Desvignes, M., Constans, J. M., Revenu, M. (1999). MRI geometric distortion: a simple approach to correcting the effects of non-linear gradient fields. *J Magn Reson Imaging, 9*(6), 821-831.

Lauterbur, P. C. (1989). Image formation by induced local interactions. Examples employing nuclear magnetic resonance. 1973. *Clin Orthop Relat Res*(244), 3-6.

Lehmann, T. M., Gonner, C., Spitzer, K. (1999). Survey: interpolation methods in medical image processing. *IEEE Trans Med Imaging, 18*(11), 1049-1075.

Lin, F. H., Chen, Y. J., Belliveau, J. W., Wald, L. L. (2003). A wavelet-based approximation of surface coil sensitivity profiles for correction of image intensity

inhomogeneity and parallel imaging reconstruction. *Hum Brain Mapp, 19*(2), 96-111.

Lin, Y., Wohlberg, B. (2008, 24-26 March 2008). *Application of the UPRE Method to Optimal Parameter Selection for Large Scale Regularization Problems.* Paper presented at the Image Analysis and Interpretation, 2008. SSIAI 2008. IEEE Southwest Symposium on.

Liu, C., Bammer, R., Moseley, M. E. (2007). Parallel imaging reconstruction for arbitrary trajectories using k-space sparse matrices (kSPA). *Magn Reson Med, 58*(6), 1171-1181.

Liu, Q. H., Nguyen, N. (1998). An accurate algorithm for nonuniform fast Fourier transforms (NUFFT's). *IEEE Microwave and Guided Wave Letters, 8*(1), 18-20.

Lu, K., Liu, T. T., Bydder, M. (2008). Optimal phase difference reconstruction: comparison of two methods. *Magn Reson Imaging, 26*(1), 142-145.

Ludeke, K. M., Roschmann, P., Tischler, R. (1985). Susceptibility artefacts in NMR imaging. *Magn Reson Imaging, 3*(4), 329-343.

Luengviriya, C. (2010). Necessity of sensitivity profile correction in retrospective motion correction at 7T MRI. *IISMRM Workshop on Current Concepts of Motion Correction for MRI & MRS; Kitzbühel, Tyrol, Austria. 2010. (ISMRM Workshop on Current Concepts of Motion Correction for MRI & MRS, Kitzbuhel, Tyrol, Austria).*

Lustig, M., Donoho, D., Pauly, J. M. (2007). Sparse MRI: The application of compressed sensing for rapid MR imaging. *Magn Reson Med, 58*(6), 1182-1195.

Lustig, M., Pauly, J. M. (2010). SPIRiT: Iterative self-consistent parallel imaging reconstruction from arbitrary k-space. *Magn Reson Med, 64*(2), 457-471.

Maas, L. C., Frederick, B. D., Renshaw, P. F. (1997). Decoupled automated rotational and translational registration for functional MRI time series data: the DART registration algorithm. *Magn Reson Med, 37*(1), 131-139.

Maclaren, J., Armstrong, B. S., Barrows, R. T., Danishad, K. A., Ernst, T., Foster, C. L., . . . Zaitsev, M. (2012). Measurement and correction of microscopic head motion during magnetic resonance imaging of the brain. *PLoS One, 7*(11), e48088.

Maclaren, J., Herbst, M., Speck, O., Zaitsev, M. (2013). Prospective motion correction in brain imaging: a review. *Magn Reson Med, 69*(3), 621-636.

Maclaren, J., Lee, K. J., Luengviriya, C., Speck, O., Zaitsev, M. (2011). Combined prospective and retrospective motion correction to relax navigator requirements. *Magn Reson Med, 65*(6), 1724-1732.

Mahesh, M. (2004). AAPM/RSNA physics tutorial for residents: digital mammography: an overview. *Radiographics, 24*(6), 1747-1760.

Manke, D., Nehrke, K., Bornert, P. (2003). Novel prospective respiratory motion correction approach for free-breathing coronary MR angiography using a patient-adapted affine motion model. *Magn Reson Med, 50*(1), 122-131.

Mansfield, P., Maudsley, A. A. (1977). Medical imaging by NMR. *Br J Radiol, 50*(591), 188-194.

Menuel, C., Garnero, L., Bardinet, E., Poupon, F., Phalippou, D., Dormont, D. (2005). Characterization and correction of distortions in stereotactic magnetic resonance imaging for bilateral subthalamic stimulation in Parkinson disease. *Journal of Neurosurgery, 103*(2), 256-266.

Meyer, C. H., Hu, B. S., Nishimura, D. G., Macovski, A. (1992). Fast spiral coronary artery imaging. *Magn Reson Med, 28*(2), 202-213.

Michiels, J., Bosmans, H., Pelgrims, P., Vandermeulen, D., Gybels, J., Marchal, G., Suetens, P. (1994). On the problem of geometric distortion in magnetic resonance images for stereotactic neurosurgery. *Magn Reson Imaging, 12*(5), 749-765.

Moriguchi, H., Wendt, M., Duerk, J. L. (2000). Applying the uniform resampling (URS) algorithm to a lissajous trajectory: fast image reconstruction with optimal gridding. *Magn Reson Med, 44*(5), 766-781.

Muresan, L., Renken, R., Roerdink, J. B., Duifhuis, H. (2005). Automated correction of spin-history related motion artefacts in fMRI: simulated and phantom data. *IEEE Trans Biomed Eng, 52*(8), 1450-1460.

Nehrke, K., Bornert, P. (2005). Prospective correction of affine motion for arbitrary MR sequences on a clinical scanner. *Magn Reson Med, 54*(5), 1130-1138.

Nguyen, N., Liu, Q. H. (1999). The Regular Fourier Matrices and Nonuniform Fast Fourier Transforms. *SIAM Journal on Scientific Computing, 21*(1), 283-293.

O'Donnell, M., Edelstein, W. A. (1985). NMR imaging in the presence of magnetic field inhomogeneities and gradient field nonlinearities. *Med Phys, 12*(1), 20-26.

O'Sullivan, J. (1985). A Fast Sinc Function Gridding Algorithm for Fourier Inversion in Computer Tomography. *IEEE Trans Med Imaging, 4*(4), 200-207.

Ooi, M. B., Krueger, S., Muraskin, J., Thomas, W. J., Brown, T. R. (2011). Echo-planar imaging with prospective slice-by-slice motion correction using active markers. *Magn Reson Med, 66*(1), 73-81.

Ooi, M. B., Krueger, S., Thomas, W. J., Swaminathan, S. V., Brown, T. R. (2009). Prospective real-time correction for arbitrary head motion using active markers. *Magn Reson Med, 62*(4), 943-954.

Ooi, M. B., Muraskin, J., Zou, X., Thomas, W. J., Krueger, S., Aksoy, M., . . . Brown, T. R. (2013). Combined prospective and retrospective correction to reduce motion-induced image misalignment and geometric distortions in EPI. *Magn Reson Med, 69*(3), 803-811.

Papp, D., Callaghan, M. F., Meyer, H., Buckley, C., Weiskopf, N. (2015). Correction of inter-scan motion artifacts in quantitative R1 mapping by accounting for receive coil sensitivity effects. *Magn Reson Med*.

Pauly, J., Nishimura, D., Macovski, A. (2011). A k-space analysis of small-tip-angle excitation. 1989. *Journal of magnetic resonance (San Diego, Calif : 1997), 213*(2), 544-557.

Pipe, J. G. (1999). Motion correction with PROPELLER MRI: application to head motion and free-breathing cardiac imaging. *Magn Reson Med, 42*(5), 963-969.

Pipe, J. G., Menon, P. (1999). Sampling density compensation in MRI: rationale and an iterative numerical solution. *Magn Reson Med, 41*(1), 179-186.

Polzin, J. A., Kruger, D. G., Gurr, D. H., Brittain, J. H., Riederer, S. J. (2004). Correction for gradient nonlinearity in continuously moving table MR imaging. *Magn Reson Med, 52*(1), 181-187.

Pruessmann, K. P., Weiger, M., Scheidegger, M. B., Boesiger, P. (1999). SENSE: sensitivity encoding for fast MRI. *Magn Reson Med, 42*(5), 952-962.

Qin, L., van Gelderen, P., Derbyshire, J. A., Jin, F., Lee, J., de Zwart, J. A., . . . Duyn, J. H. (2009). Prospective head-movement correction for high-resolution MRI using an in-bore optical tracking system. *Magn Reson Med, 62*(4), 924-934.

Rasche, V., Proksa, R., Sinkus, R., Bornert, P., Eggers, H. (1999a). Resampling of data between arbitrary grids using convolution interpolation. *IEEE Trans Med Imaging, 18*(5), 385-392.

Rasche, V., Proksa, R., Sinkus, R., Bornert, P., Eggers, H. (1999b). Resampling of data between arbitrary grids using convolution interpolation. *IEEE Trans Med Imaging, 18*(5), 385-392.

Robinson, S., Jovicich, J. (2011). B0 mapping with multi-channel RF coils at high field. *Magn Reson Med, 66*(4), 976-988.

Robinson, S., Schodl, H., Trattnig, S. (2014). A method for unwrapping highly wrapped multi-echo phase images at very high field: UMPIRE. *Magn Reson Med, 72*(1), 80-92.

Rosenfeld, D. (1998). An optimal and efficient new gridding algorithm using singular value decomposition. *Magn Reson Med, 40*(1), 14-23.

Sarty, G. E., Bennett, R., Cox, R. W. (2001). Direct reconstruction of non-Cartesian k-space data using a nonuniform fast Fourier transform. *Magn Reson Med, 45*(5), 908-915.

Schad, L. R., Ehricke, H. H., Wowra, B., Layer, G., Engenhart, R., Kauczor, H. U., . . . Lorenz, W. J. (1992). Correction of spatial distortion in magnetic resonance angiography for radiosurgical treatment planning of cerebral arteriovenous malformations. *Magn Reson Imaging, 10*(4), 609-621.

Schad, L. R., Lott, S., Schmitt, F., Sturm, V., Lorenz, W. J. (1987). Correction of Spatial Distortion in MR Imaging: A Prerequisite for Accurate Stereotaxy. *J Comput Assist Tomogr, 11*(3), 499-505.

Sha, L., Guo, H., Song, A. W. (2003). An improved gridding method for spiral MRI using nonuniform fast Fourier transform. *Journal of magnetic resonance (San Diego, Calif : 1997), 162*(2), 250-258.

Shechter, G., Ozturk, C., Resar, J. R., McVeigh, E. R. (2004). Respiratory motion of the heart from free breathing coronary angiograms. *IEEE Trans Med Imaging, 23*(8), 1046-1056.

Slavens, Z. W. (2008). *Generalized Interpolation applied to MR Image Magnification and Gradient Nonlinearity Correction (Doctoral dissertation).* http://speechlab.eece.mu.edu/johnson/papers/slavens_thesis.pdf.

Song, J., Liu, Y., Gewalt, S. L., Cofer, G., Johnson, G. A., Liu, Q. H. (2009). Least-Square NUFFT Methods Applied to 2-D and 3-D Radially Encoded MR Image Reconstruction. *IEEE Transactions on Biomedical Engineering, 56*(4), 1134-1142.

Speck, O., Hennig, J., Zaitsev, M. (2006). Prospective real-time slice-by-slice motion correction for fMRI in freely moving subjects. *MAGMA, 19*(2), 55-61.

Speck, O., Stadler, J., Zaitsev, M. (2008). High resolution single-shot EPI at 7T. *MAGMA, 21*(1-2), 73-86.

Stucht, D., Danishad, K. A., Schulze, P., Godenschweger, F., Zaitsev, M., Speck, O. (2015). Highest Resolution In Vivo Human Brain MRI Using Prospective Motion Correction. *PLoS One, 10*(7), e0133921.

Sulikowska, A. (2014). Will field shifts due to head rotation compromise motion correction. *In: Proceedings of Joint Annual Meeting ISMRM-ESMRMB, Milan*, p 0885.

Sumanaweera, T. S., Adler, J. R., Jr., Napel, S., Glover, G. H. (1994). Characterization of spatial distortion in magnetic resonance imaging and its implications for stereotactic surgery. *Neurosurgery, 35*(4), 696-703; discussion 703-694.

Sutton, B., Noll, D., Fessler, J. (2003). Fast, iterative image reconstruction for MRI in the presence of field inhomogeneities. *IEEE Trans Med Imaging, 22*(2), 178-188.

Tao, S., Trzasko, J. D., Shu, Y., Huston, J., 3rd, Bernstein, M. A. (2015). Integrated image reconstruction and gradient nonlinearity correction. *Magn Reson Med, 74*(4), 1019-1031.

Tao, S., Trzasko, J. D., Shu, Y., Huston, J., 3rd, Johnson, K. M., Weavers, P. T., . . . Bernstein, M. A. (2015). NonCartesian MR image reconstruction with integrated gradient nonlinearity correction. *Med Phys, 42*(12), 7190.

Thesen, S., Heid, O., Mueller, E., Schad, L. R. (2000). Prospective acquisition correction for head motion with image-based tracking for real-time fMRI. *Magn Reson Med, 44*(3), 457-465.

Thevenaz, P., Blu, T., Unser, M. (2000). Interpolation revisited. *IEEE Trans Med Imaging, 19*(7), 739-758.

Tian, Q., Gong, E., Leuze, C., Pauly, J., McNab, J. (2015). Effects of Motion on Coupling of Coil Elements and Parallel Imaging Reconstruction at 3T and 7T. *In: Proceedings of 23rd scientific meeting, International Society of Magnetic Resonance in Medicine, Toronto*, p 6702.

Twieg, D. B. (1983). The k-trajectory formulation of the NMR imaging process with applications in analysis and synthesis of imaging methods. *Med Phys, 10*(5), 610-621.

Ulaby, F. T. (1997). *Fundamentals of applied electromagnetics*: Prentice-Hall, Inc.

Unser, M. A. (2002). *Splines: a perfect fit for medical imaging.* Paper presented at the Medical Imaging 2002.

van der Kouwe, A. J., Benner, T., Dale, A. M. (2006). Real-time rigid body motion correction and shimming using cloverleaf navigators. *Magn Reson Med, 56*(5), 1019-1032.

Vogel, C. (1996). Non-convergence of the L-curve regularization parameter selection method. *Inverse Problems, 12*, 535-547.

Walsh, D. O., Gmitro, A. F., Marcellin, M. W. (2000). Adaptive reconstruction of phased array MR imagery. *Magn Reson Med, 43*(5), 682-690.

Walton, L., Hampshire, A., Forster, D. M., Kemeny, A. A. (1997). Stereotactic localization with magnetic resonance imaging: a phantom study to compare the accuracy obtained using two-dimensional and three-dimensional data acquisitions. *Neurosurgery, 41*(1), 131-137; discussion 137-139.

Wang, D., Strugnell, W., Cowin, G., Doddrell, D. M., Slaughter, R. (2004a). Geometric distortion in clinical MRI systems. *Magn Reson Imaging, 22*(9), 1211-1221.

Wang, D., Strugnell, W., Cowin, G., Doddrell, D. M., Slaughter, R. (2004b). Geometric distortion in clinical MRI systems Part I: evaluation using a 3D phantom. *Magn Reson Imaging, 22*(9), 1211-1221.

Ward, H. A., Riederer, S. J., Grimm, R. C., Ehman, R. L., Felmlee, J. P., Jack, C. R., Jr. (2000). Prospective multiaxial motion correction for fMRI. *Magn Reson Med, 43*(3), 459-469.

Weinhandl, J. T., Armstrong, B. S., Kusik, T. P., Barrows, R. T., O'Connor, K. M. (2010). Validation of a single camera three-dimensional motion tracking system. *J Biomech, 43*(7), 1437-1440.

Weisskoff, R. M., Kiihne, S. (1992). MRI susceptometry: image-based measurement of absolute susceptibility of MR contrast agents and human blood. *Magn Reson Med, 24*(2), 375-383.

Welch, E. B., Manduca, A., Grimm, R. C., Ward, H. A., Jack, C. R., Jr. (2002). Spherical navigator echoes for full 3D rigid body motion measurement in MRI. *Magn Reson Med, 47*(1), 32-41.

Wey, H., Huang, J., Hsu, Y., Lim, K., Kuan, W., Chen, C., Liu, H. (2006). Image Quality Testing Using An Oil-Filled ACR MRI Phantom at 3 T. *Med Phys, 33*(6), 2009-2009.

White, N., Roddey, C., Shankaranarayanan, A., Han, E., Rettmann, D., Santos, J., . . . Dale, A. (2010). PROMO: Real-time prospective motion correction in MRI using image-based tracking. *Magn Reson Med, 63*(1), 91-105.

Xuguang, J. (2011). Iterative reconstruction method for three-dimensional non-Cartesian parallel MRI (Doctoral dissertation). *Retrieved from http://ir.uiowa.edu/cgi/viewcontent.cgi?article=2376&context=etd*.

Yancey, S. E., Rotenberg, D. J., Tam, F., Chiew, M., Ranieri, S., Biswas, L., . . . Graham, S. J. (2011). Spin-history artifact during functional MRI: potential for adaptive correction. *Med Phys, 38*(8), 4634-4646.

Zaitsev, M., Dold, C., Sakas, G., Hennig, J., Speck, O. (2006). Magnetic resonance imaging of freely moving objects: prospective real-time motion correction using an external optical motion tracking system. *Neuroimage, 31*(3), 1038-1050.

Zhang, T., Pauly, J. M., Vasanawala, S. S., Lustig, M. (2013). Coil compression for accelerated imaging with Cartesian sampling. *Magn Reson Med, 69*(2), 571-582.

Zhao, T., Hu, X. (2008). Iterative GRAPPA (iGRAPPA) for improved parallel imaging reconstruction. *Magn Reson Med, 59*(4), 903-907.

Zhuo, J., Gullapalli, R. P. (2006). AAPM/RSNA physics tutorial for residents: MR artifacts, safety, and quality control. *Radiographics, 26*(1), 275-297.

PUBLICATIONS

Journal Articles

- Yarach U, Luengviriya C, Danishad A, Stucht D, Godenschweger F, Schulze P, Speck O (2015). Correction of gradient nonlinearity artifacts in prospective motion correction for 7T MRI. Magn Reson Med, 73(4), 1562-1569.
- Yarach U, Luengviriya C, Stucht D, Godenschweger F, Schulze P, Speck O (2016). Correction of B0-induced geometric distortion variations in prospective motion correction for 7T MRI. Magn Reson Mater Phy, 1-14. (Epub ahead of print)
- Godenschweger F, Kaegebein U, Stucht D, Yarach U, Sciarra A, Yakupov R, Luesebrink F, Schulze P, Speck O (2016). Motion correction in MRI of the brain. Phys Med Biol. 61(5) R32-56. (Epub ahead of print)

International Conferences

- Yarach U, Stucht D, Mattern H, Godenschweger F, Speck O (2016). Gradient Nonlinearity and B0-induced Distortion Corrections of Prospective Motion Correction Data at 7T MRI. ISMRM 24th Annual Meeting, Singapore. (Electronic poster).
- Yarach U, Mattern H, Sciarra A, Speck O (2016). Combination of Individual Coil QSM at High Field Strength (7T). ISMRM 24th Annual Meeting, Singapore. (Poster presentation).
- Yarach U, Stucht D, Godenschweger F, Speck O (2015). The Necessity of Coil Sensitivity & Gradient Non-Linearity Distortion Corrections in Prospective Motion Correction. ISMRM 23rd Annual Meeting, Toronto. (Poster presentation).
- Yarach U, Stucht D, Godenschweger F, Speck O (2015). The Correction of Motion-Induced Coil Sensitivity Miscalibration in Parallel Imaging with Prospective Motion Correction. ISMRM 23rd Annual Meeting, Toronto. (Poster resentation).

- Yarach U, Danishad KA, Luengviriya C, In M.H., Stucht D, Speck O (2013). RF-Sensitivity and Gradient Non-Linearity Distortion Corrections in Prospective Mo-Co at 7T MRI. ESMRMB, Toulouse. (Electronic poster).

ERKLÄRUNG

Hiermit erkläre ich, dass ich die von mir eingereichte Dissertation zum dem Thema

“Correction of Residual artifacts in Prospectively Motion-corrected MR-data”

selbständig verfasst, nicht schon als Dissertation verwendet habe und die benutzten Hilfsmittel und Quellen vollständig angegeben wurden.

Weiterhin erkläre ich, dass ich weder diese noch eine andere Arbeit zur Erlangung des akademischen Grades doctor rerum naturalium (Dr. rer. nat.) an anderen Einrichtungen eingereicht habe.

Magdeburg, Dezember. 2016 Uten Yarach